Dissertation

submitted to the
Instituto de Astrofísica, Facultad de Física
Pontificia Universidad Católica de Chile, Chile
for the degree of
Doctor in Astrophysics

submitted to the
Combined Faculties for the Natural Sciences and for Mathematics
of the Ruperto-Carola University of Heidelberg, Germany
for the degree of
Doctor of Natural Sciences

Put forward by

Felipe Garrido Goicovic
Born in Santiago, Chile

Oral examination: 08 August 2017

Infalling clouds onto supermassive black hole binaries

Felipe Garrido Goicovic
Heidelberg Institute for Theoretical Studies

Referees: Prof. Dr. Volker Springel
Prof. Dr. Jorge Cuadra

"Science is not only a disciple of reason but, also, one of romance and passion."

Stephen Hawking

Abstract

Infalling clouds onto supermassive black hole binaries

by Felipe Garrido Goicovic

There is compelling evidence that most –if not all– galaxies harbour a supermassive black hole at their nucleus, hence binaries of these massive objects are an inevitable product of the hierarchical evolution of structures in the universe, and represent an important but thus-far elusive piece of the galaxy formation puzzle.

Gas accretion is thought to be important for the dynamical evolution of supermassive black hole binaries (SMBHBs), as well as in producing luminous emission that can be used to infer their properties, although the mechanisms that drive material to the galactic nuclei are poorly constrained. One plausible source of the gaseous fuel is cold clumps of gas formed due to turbulence and gravitational instabilities in the interstellar medium that later fall towards and interact with the binary. In this context, I present a suite of smoothed-particle-hydrodynamical models to study the evolution of turbulent gas clouds as they infall towards equal-mass, circular SMBHBs.

I use a set of high-resolution simulations of separate clouds infalling onto binaries to study the formation of gaseous structures and their dynamics, as well as the feeding rate onto the SMBHB, depending on different orbital configurations. I show that some of the variabilities can have implications in the observability of these systems.

Additionally, exploiting similar single cloud models, I study the dynamical evolution of the binary orbit during the interaction with different clouds and show that it is dominated by the exchange of angular momentum through gas capture and accretion. Building on these results, I construct a simple model for the long-term evolution of a SMBHB interacting with several incoming clouds, which are randomly drawn from reasonable populations with different levels of anisotropy. In this scenario, the binary evolves down to the gravitational emission regime within a few hundred million years.

I finally extend the simulations to a binary interacting with a sequence of incoherent clouds to investigate the secular effects of the left-over gas on the SMBHB orbital evolution, previously unresolved with the single cloud models. After a sequence of ten events, I observe that these secular effects further increase the efficiency of the incoherent clouds with respect to a scenario that only considers the prompt accretion phase.

All these results suggest that sub-parsec SMBHBs embedded in gas-rich and turbulent environments efficiently evolve towards coalescence during the interaction with individual gas pockets, providing a possible solution to the "final parsec problem".

Resumen

Nubes cayendo a binarias de agujeros negros súper-masivos

por Felipe Garrido Goicovic

Existe numerosa evidencia que la mayoría –sino todas– las galaxias albergan un agujero negro súper-masivo en su núcleo, por lo que binarias de estos objetos son un producto inevitable de la formación jerárquica de estructuras en el universo, y representan una importante, pero hasta ahora elusiva, pieza en el rompecabezas de la evolución de galaxias.

La acreción de gas ha sido postulada como una etapa importante durante la evolución dinámica de binarias de agujeros negros súper-masivos, adicionalmente produciendo emisiones luminosas que pueden ser usadas para inferir sus propiedades, aunque los mecanismos que llevan material hacia el núcleo galáctico aún no son bien entendidos. Una fuente posible de material gaseoso son aglomeraciones frías que se forman debido a turbulencias e inestabilidades gravitatorias en el medio interestelar que luego caen hacia la binaria e interactúan con ella. En este contexto, presento un conjunto de modelos numéricos para estudiar la evolución hidrodinámica de nubes gaseosas turbulentas a medida que caen a binarias de igual masa y circulares.

Usando simulaciones de alta resolución de una nube individual cayendo a distintas binarias estudio la formación de estructuras gaseosas y su dinámica, así como la tasa de alimentación de los agujeros negros, dependiendo de las diferentes configuraciones orbitales de la nube. Muestro que algunas de las variabilidades presentes pueden tener implicancias en la observabilidad de estos sistemas.

Adicionalmente, con modelos similares de nubes individuales, estudio la evolución dinámica de la órbita de la binaria durante la interacción con diferentes nubes. Demuestro que esta evolución está dominada por el intercambio de momento angular a través de captura y acreción durante las primeras etapas de la interacción. Usando estos resultados, construyo un modelo simple de una binaria interactuando con varias nubes, las cuales son generadas al azar desde poblaciones con distintos niveles de anisotropía. En este escenario, la binaria evoluciona eficientemente hasta el régimen de ondas gravitacionales dentro de algunos cientos de millones de años.

Finalmente extiendo estas simulaciones a una binaria que interactúa con una secuencia de nubes incoherentes para investigar los efectos seculares del gas restante en la órbita del la binaria, previamente no resueltos con los modelos de nubes individuales. Luego de una secuencia de diez nubes, observo que los efectos seculares incrementan la eficiencia de las nubes incoherentes para disminuir la órbita de la binaria con respecto a un escenario que solo considera la evolución durante la etapa de acreción fuerte.

Todos estos resultados sugieren los agujeros súper-masivos binarios sub-parsec dentro de un ambiente rico en gas y turbulento eficientemente contraen su órbita durante la interacción con porciones discretas de gas, proporcionando una solución al "problema del último pársec".

Zusammenfassung

Interaktion einfallender Gaswolken mit Paaren superschwerer schwarzer Löcher

von Felipe Garrido Goicovic

Es gibt überzeugende Hinweise dafür, dass die meisten –wenn nicht alle– Galaxien superschwere schwarze Löcher in ihren Zentren beherbergen. Binärsysteme dieser massiven Objekte sind folglich ein unvermeidbares Produkt der hierarchischen Strukturentstehung im Universum und stellen einen wichtigen und bis heute wenig verstandenen Teil der Galaxieentstehung dar.

Gas-Akkretion wird als wichtiger Einflussfaktor sowohl auf die Dynamik als auch auf die Emission elektromagnetischer Strahlung von Paaren superschwerer schwarzer Löcher angesehen, wenngleich über die Interaktionsmechanismen zwischen Gas und den schwarzen Löchern wenig bekannt ist. Eine mögliche Quelle für einfallendes Material sind kalte Gasklumpen, welche durch Turbulenz im interstellaren Medium und gravitative Instabilitäten gebildet wurden und sich später dem Binärsystem nähern und mit ihm interagieren. In diesem Zusammenhang stelle ich eine Reihe teilchenbasierter Hydrodynamik-Simulationen vor, mit welchen ich die Entwicklung turbulenter Gaswolken erforsche, die auf ein Paar superschwerer schwarzer Löcher gleicher Masse auf kreisförmigen Umlaufbahnen treffen.

Ich verwende hochaufgelöste Simulationen einzelner einfallender Wolken, um die Entstehung und Dynamik von Gasstrukturen und das Wachstum der superschweren schwarzen Löcher durch Gasakkretion sowie dessen Abhängigkeit von verschiedenen Bahnkonfigurationen des einfallenden Gases zu untersuchen. Ich zeige, dass einige dieser Variationen die Beobachtbarkeit dieser Systeme beeinflussen.

Zusätzlich, unter Benutzung der Ergebnisse der Simulationen einzelner Wolken, untersuche ich die Dynamik des Binärsystems durch die Interaktion mit mehreren Wolken und zeige, dass dieser Prozess dominiert ist durch das Einfangen von Gas und der damit einhergehenden Änderung des Drehimpulses in der frühen Phase des Zusammentreffens von Gas und Binärsystem. Auf diesen Resultaten aufbauend entwickle ich ein einfaches Modell, welches die Entwicklung von Paaren von superschweren schwarzen Löchern und deren Interaktion mit einigen einfallenden Gaswolken, welche zufällig aus einer Verteilung realistischer Bahnen mit verschiedener Anisotropie ausgewählt werden, beschreibt. In diesem Modell verengt sich die Bahn des Binärsystems bis hin zum Regime der von Gravitationswellen dominierten Emission innerhalb weniger hundert Millionen Jahren.

Zuletzt verallgemeinere ich die Simulationen auf Binärsysteme, welche mit einer Reihe inkohärenter Wolken interagieren, um den Effekt des übrig gebliebenen Gases auf die Entwicklung der Bahnen der Binärsysteme zu untersuchen, einem Effekt der nicht von den Modellen einzelner Wolken erfasst wurde. Nach zehn Ereignissen verstärken säkulare Effekte die Effizienz des Wolkeneinfalls verglichen mit einer einzelnen Akkretionsphase.

All diese Ergebnisse deuten darauf hin, dass Paare superschwerer schwarzer Löcher, welche weniger als parsec Skalen von einander entfernt sind und sich in einer Gas-reichen und turbulenten Umgebung befinden, sich durch die Interaktion mit Gaswolken sehr effizient nähern und letztendlich verschmelzen. Dieses Szenario stellt eine mögliche Lösung des „letzten Parsec Problems“dar.

x

Acknowledgements

There is no way I can mention all the people who have been part of my life, and made a positive impact in it. If you are reading these words and your name is not listed, please do not feel left out, but know that I appreciate even the smallest moment that helped build the person sitting here today writing this thesis.

The first and foremost acknowledgement is for my advisor, Jorge Cuadra. I do not believe I have enough words to express how grateful I am to had worked with him as a colleague and a friend. I could not have asked for a better supervisor, his guidance and advise were crucial for me during all these years. I will also be forever indebted for all the opportunities he found for me that finally led to the exciting path I am today.

Also I cannot forget to thank Volker Springel for giving me the opportunity to work with him, one of the most prestigious astrophysicists working today. His immense knowledge is only matched by his humble personality. It has been a huge privilege to have learned from him and his group.

I will also be forever grateful to my wife and partner, Johanna, whose sole presence in my life is a continuous reminder of how lucky I am, and who never let me put my arms down whenever I panicked due to my stressful nature. She is the pillar that holds my life together, without her love and support I would not have made it this far. I am extremely thankful to her for being the one that put up with all my mood swings during the writing of this thesis, and for being the most beautiful proof-reader ever.

I can not forget to thank my mother, brother and sister for their unconditional love, especially knowing that I am not the easiest person to deal with. I am indebted to them for sticking with me when I needed it the most. To my dear mom Giselle, who showed me so many wonderful things about this world and planted the seed of curiosity that drives me every moment of my life. I would not be the person I am today without her teachings. Along the same lines, my life would had not been the same without the presence and continuous instruction of my grandfather, Raúl Goicovic, for whom this thesis is dedicated. He essentially inspired me to pursue a life of knowledge and discovery that ultimately resulted in my scientific career.

I am also extremely grateful to my wife's family, my in-laws, who not only welcomed me as one of their own, but were an enormous support throughout this whole process. A special thanks to María Carolina for those delicious afternoon "onces" that I was looking forward every week, and also for always sending me caring words (and stickers).

A warm thanks to my friends and fellow grad students, Camila Navarrete, Rodrigo Leiva, Diego Calderón, Camilo Fontecilla, Francisco Aros and Gergely Hajdu, for making my day a little brighter with their presence. And a very special acknowledgment to my friend Cristián Maureira, who joined me in the adventure of modelling infalling clouds, and who taught me so much computing and programming "stuff" that will be useful for the rest of my life.

Also to my friends in Heidelberg, Mauricio Ortiz, Natalia Kudryavtseva (well, Natalia Ortiz now), María José Cordero and Jorge Díaz, thanks for making this foreign city feel like home.

To all those amazing researchers I encounter during my studies, Alberto Sesana, Federico Stasyszyn, Pau Amaro-Seoane, Xian Chen, Taka Tanaka and Massimo Dotti, I am grateful for all those brilliant discussions and their help during the long road that has been my research.

To my first "mentor" Nelson Padilla, who was very important during the early stages of my development as a scientist, I am thankful for his infinite patience and dedication when I was a young and naive undergrad.

To the members of the PLAGA group at PUC, Virginie Faramaz, Nicolás Cuello, Sebastián Stammler and Matías Gárate, my thanks for all those wonderful and entertaining group meetings with stimulating discussions, and of course, for those amazing croissants we shared. I also want to thank our companion group at Universidad de Chile, led by Andrés Escala, that helped me along the way, in particular to Luciano del Valle.

I am extremely grateful to the Theoretical Astrophysics group (TAP), and the HITS in general, for their warm hospitality during my stay there. They provided the perfect environment one could expect to finish a thesis. A special thanks to Reiner Weinberger for translating my abstract to German.

I am also indebted to the following institutions that hosted me during the development of this project: the Albert Einstein Institute (AEI), the Leibniz Institute for Astrophysics Potsdam (AIP), the Max Planck Institute for Astronomy (MPA), the School of Physics and Astronomy of the University of Birmingham, and the Max Planck Institute for Extraterrestrial physics (MPE).

During my doctoral studies I was supported by the CONICYT PCHA/Doctorado Nacional scholarship and the PUC-HD Graduate Exchange Fellowship by the DAAD. This project was partly supported from CONICYT-Chile through FONDECYT (1141175), Basal (PFB0609), Anillo (ACT1101), Redes (120021), and Exchange (PCCI130064) grants; from the DAAD (57055277); from the European Commission's Framework Programme 7, through the Marie Curie International Research Staff Exchange Scheme LACEGAL (PIRSES-GA-2010-269264); from the Max Planck Society through a partner group grant.

All the simulations presented in this thesis were partially performed between the *datura* cluster at the AEI, the *geryon* computers at the Center for Astro-Engineering UC, and the *sandy-bridge* computers at HITS.

Contents

List of Figures

List of Tables

List of Abbreviations

BH	Black Hole
SMBH	Supermassive Black Hole
SMBHB	Supermassive Black Hole Binary
GW	Gravitational Wave
LIGO	Laser Interferometer Gravitational-wave Observatory
LISA	Laser Interferometer Space Antenna
PTA	Pulsar Timing Array
QSO	Quasi Stellar Object (quasar)
AGN	Active Galactic Nucleus
SPH	Smoothed Particle Hydrodynamics

Dedicated to Raúl Goicovic, whose greatness inspired so many...

Chapter 1

Introduction

A black hole (BH) is simply a region of spacetime that cannot communicate with the external Universe. This occurs when an object has a gravitational field so strong that its escape velocity is larger than the speed of light, hence nothing can escape from it, including light. The boundary of this region is called the event horizon; once something has crossed the event horizon any information from it cannot reach an outside observer, as this boundary can be crossed only in one direction – towards the black hole. Since extremely high densities are necessary to produce such an object, BHs represent the final stage of gravitational collapse.

The idea of a BH was first conceived by John Michell in 1783, which he called "dark stars" (Michell, 1784). Having accepted Newton's corpuscular theory of light, which posited that light consists of minuscule particles, he reasoned that such particles, when emanated by a star, should be slowed down by its gravitational pull. Michell proposed that stars with very large masses might exist, and if so, their gravities would be huge. Consequently, the escape velocities of such stars would be correspondingly huge, reaching values over the speed of light. In those cases, he reasoned, even light could not escape the star. A few years later, mathematician Pierre-Simon Laplace suggested a similar concept of light being trapped by objects with very high gravity (Laplace, 1799).

The emergence of Einstein's theory of general relativity at the beginning of the 20th century (Einstein, 1915) provided the theoretical framework from which gravitationally collapsed objects (including BHs) can be understood. First, Schwarzschild (1916) derived a solution for the gravitational field surrounding a spherical mass. His solution contained a complete description of the external field of spherically symmetric, electrically neutral, non-rotating BHs, which today are commonly referred as "Schwarzschild black holes". This solution had a singularity in the radial coordinate, which is now called the Schwarzschild radius, where some terms of the Einstein equations became infinite. Thanks to the contributions of Eddington (1924) and Lemaître (1933) this singularity was understood as a non-physical coordinate singularity. Finkelstein (1958) introduced the concept of the event horizon, showing that the Schwarzschild surface acts as a perfect unidirectional membrane: causal influences can cross it in only one direction. Kerr (1963) then discovered a family of charge-free solutions to Einstein's field equations representing rotating black holes. Afterwards, Newman et al. (1965) found axisymmetric solutions for a black hole that is both rotating and electrically charged. It is currently understood that the solutions described by Kerr and Newman (often called the Kerr-Newman geometry) provide a complete description of the gravitational and electromagnetic fields of stationary black holes.

John Wheeler, in 1967, used the words "black hole" in a public lecture. Unofficially, the phrase had been used earlier by others, but this spread the use of the term throughout the scientific community, as well as the general public.

Black holes were long considered just a mathematical curiosity. It was not until the 1960s that the discovery of compact X-ray sources in 1962 (Giacconi et al., 1962), quasars in 1963 (Schmidt, 1963) and pulsars in 1968 (Hewish et al., 1968), motivated plenty of new theoretical work showing that BHs were a generic prediction of general relativity, and sparked interest in gravitationally collapsed compact objects as a possible astrophysical reality. Observations of the binary X-ray source Cygnus X-1 finally provided the first plausible evidence that black holes might actually exist in our Universe (Bolton, 1972; Webster and Murdin, 1972).

Despite the fact that BHs are "invisible" because they do not directly emit electromagnetic radiation[1], their presence can be inferred through their gravitational influence over the surrounding medium. Binary systems that include a BH are often sources of huge amounts of energy. This includes one of the most important known mechanisms of energy production around BHs: *accretion*. Matter falling through the steep gravitational potential of a BH, and then being captured by it, implies that roughly 10% of the accreted rest-mass energy should be converted into radiation. Consequently, accretion is a powerful source of energy, considerably more efficient than many other known mechanisms (e.g., nuclear fusion <1%). When gas falls onto a BH, it usually settles into a disc due to conservation of angular momentum, which then starts radiating as it is heated by friction, producing some of the brightest objects in the Universe.

Another noteworthy mechanism for detection of BHs, and more relevant to this work, is the emission of gravitational waves (GWs). In 1916, the year after the final formulation of the field equations of general relativity, Albert Einstein predicted the existence of gravitational waves (Einstein, 1916). He found that the linearised weak-field equations had wave solutions: transverse waves of spatial strain that travel at the speed of light, generated by time variations of the mass quadrupole moment of the source.

GW astronomy is an emerging branch of observational astronomy which aims to use gravitational radiation to collect data from sources with detectable GWs, mainly from binary systems, and most notably, binary black holes. GWs carry energy away from their sources and, in the case of orbiting bodies, this is associated with an inspiral or decrease in orbit. On February 11, 2016, the Laser Interferometer Gravitational-Wave Observatory (LIGO) collaboration announced the first detection of gravitational waves (Abbott et al., 2016), made simultaneously on September 14, 2015 by the two LIGO detectors. The source, denoted as GW150914, was consistent with the inspiral and merger of a pair of black holes with around $30M_{\odot}$ each. This discovery, undoubtedly one of the most significant scientific achievements of this century, not only has opened up a new window to observe our Universe not accessible with electromagnetic radiation, but also represents the first observation of a binary black hole merger.

In our Universe, astrophysical black holes had been observed in two very distinctive mass regimes: the "stellar mass black holes" with masses in the range ~ 1 – $30\ M_{\odot}$ (Özel et al., 2010) which are the remnants expected to form when very massive stars collapse at the end of their life cycle; and "supermassive black holes" (hereafter SMBHs) with masses of $\sim 10^6$ – $10^{10}\ M_{\odot}$ (Kelly and Shen, 2013) which have been observed to reside in the nuclear regions of galaxies. This thesis focuses exclusively on the latter.

[1]Hawking radiation, which has been hypothesised to arise from quantum effects at the event horizon (Hawking, 1974), is too small to be observed directly, hence it is irrelevant in astrophysical contexts.

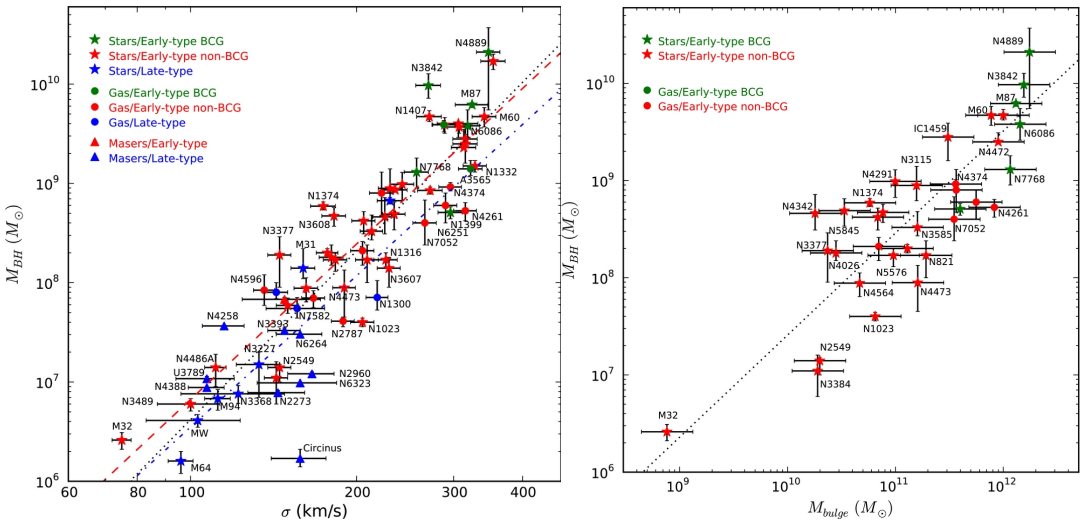

FIGURE 1.1: Relations between the mass of the SMBH and the bulge of the host galaxy. The left panel shows the bulge's velocity dispersion, while the right panel corresponds to the bulge's mass. These well-established observational correlations have been explained by the coevolution scenario, and represent the strongest clue that most galaxies must contain a SMBH in their nucleus. Both Figures are from McConnell and Ma (2013).

The important role of SMBHs in galaxy evolution has been established over the past decades. Hypothesised in the sixties to be the central engine of the then-discovered quasi-stellar objects (quasars or QSOs; Lynden-Bell, 1969), a growing body of evidence confirmed the existence of SMBHs in virtually every massive galaxy in the local Universe during the nineties (Kormendy and Richstone, 1995). Currently, we observe SMBHs powering the bright QSOs and the less luminous active galactic nuclei (AGN; Merloni and Heinz, 2013), but they are also observed in their quiescent state as massive dark objects in nearby galaxy spheroids (Kormendy and Ho, 2013). The most compelling case for one of these objects is in our own "backyard": the centre of the Milky-Way. Observations of the proper motions of stars in the Galactic centre around the radio source Sagittarius A* have been used to show the presence of a very massive, yet invisible object, strongly implying the presence of an (almost) inactive SMBH with a mass of $\approx 4 \times 10^6\ M_\odot$ (Ghez et al., 2008; Gillessen et al., 2009).

The discovery of tight correlations between the SMBH masses and key properties of their host galaxies (Magorrian et al., 1998; Ferrarese and Merritt, 2000; Gebhardt et al., 2000) points towards a coevolution scenario, based on an interplay of gas accretion onto the SMBH from the host, releasing a large amount of energy feeding back onto the host galaxy (Kormendy and Ho, 2013, and references therein). Figure 1.1 shows examples of two of the most well-known correlations between the mass of the black hole and the properties of the host galaxy's bulge. The left panel shows the bulge's velocity dispersion, known as the $M_{\rm BH}$-σ relation, while the right panel displays the bulge's mass, referred to as the $M_{\rm BH}$-$M_{\rm bulge}$ relation.

In view of these correlations and the proposed coevolution scenario, each step of the SMBH evolution would have an imprint in the population of galaxies. One of these steps is when two SMBHs orbit each other, forming a binary system, which is the focus of this thesis. In the following section I overview the current understanding

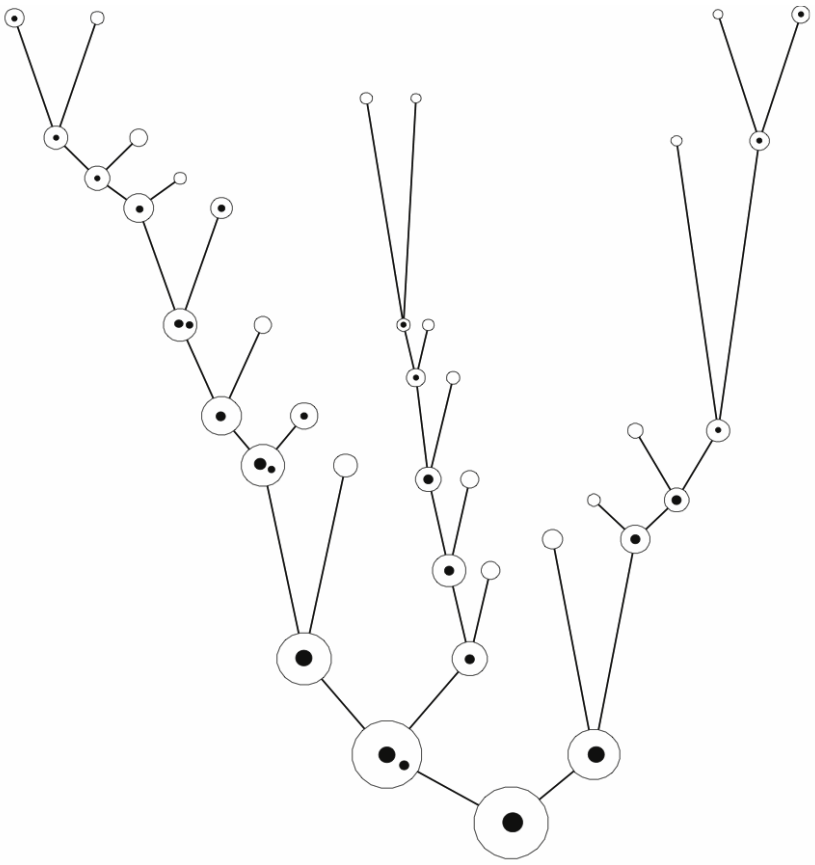

FIGURE 1.2: Schematic representation of the merger-tree history of a Milky-Way sized galaxy and its central black hole in a ΛCDM Universe. Time increases from top (”small branches”) to bottom ("trunk", present time). A galaxy is formed by the sequential merger of smaller systems (white circles), increasing in mass in a hierarchical fashion. Black holes (black dots) evolve in a similar way - merging when their hosts do. Credit: M. Volonteri (`http://www2.iap.fr/users/volonter/BHdynamics.html`)

of the black hole pairing in galaxy mergers, as well as some of the binary candidates presented in the literature to date. I refer the interested reader to the review of Colpi (2014) for a more detailed analysis.

1.1 Supermassive black holes binaries

According to our current paradigm of structure evolution in the ΛCDM cosmology, galaxies assemble hierarchically through mergers following their parent dark matter haloes, building up from smaller structures (White and Rees, 1978). An illustrative example can be seen in Fig. 1.2, where a Milky Way-type galaxy at the present time has evolved from smaller galaxies via successive mergers. In this scenario, a natural outcome of the galaxy evolution process is the formation of supermassive black hole binaries (hereafter SMBHBs). Following a merger of two galaxies, each harbouring a black hole, we expect the SMBHs to sink toward the centre of the merger remnant and eventually form a binary, as illustrated with black dots in Fig. 1.2. Therefore, understanding their formation and dynamical evolution is extremely important for reconstructing the puzzle of the hierarchical growth of structures in the Universe.

This is a central problem if we want to consider SMBHBs as powerful sources of gravitational waves, as proposed in "The Gravitational Universe" (Consortium et al., 2013).

As explained before, GWs are mainly expected from binary systems due to their quadrupolar nature. Furthermore, the strongest sources of gravitational radiation are the most massive objects moving close to the speed of light. Consequently, pairs of SMBHs orbiting each other very closely are the most energetic sources in the Universe in terms of gravitational radiation. Depending on the mass regime of the coalescing binary, the GW signal will be detected by separate techniques, due to their different frequency of operation. For moderately massive black hole masses (10^5 – $10^7 M_\odot$), these mergers will be detected with a high signal-to-noise ratio with the space-borne gravitational wave detector LISA (Laser Interferometer Space Antenna; Consortium et al., 2013). This space mission, proposed by the European Space Agency, has an arrangement of three spacecrafts forming an equilateral triangle with sides 2.5×10^6 km long, flying along an Earth-like heliocentric orbit. LISA will observe gravitational waves by measuring differential changes in the length of its arms, as sensed by laser interferometry. It will allow to explore the formation and evolution of SMBHs as early as $z \sim 10$. For example, the GWs emitted at coalescence offer a unique environment to measure very precisely the black hole masses and spins, which will allow to constrain different scenarios of seed formation and evolution (Amaro-Seoane et al., 2013).

On the other hand, for very massive binaries ($\gtrsim 10^8 M_\odot$), the frequency range will be detectable with Pulsar Timing Arrays (PTAs). This technique uses correlated signatures in the pulse's arrival times from a set of millisecond pulsars to detect and analyse possible GWs. PTA will trace binary mergers among very massive galaxies present in the already evolved universe, at redshift $z \lesssim 1$ (Hobbs et al., 2010).

Although these experiments are very promising, at present day they are not producing scientific results. First, LISA is not expected to be launched before 2030. Secondly, the timing of milli-second pulsars used by PTAs has not reached the required precision to lower the sensitivity to the point of detection. Recent PTA efforts resulted only in several upper limits by individually resolvable and assumed circular SMBHBs. For instance, the study of Babak et al. (2016) excluded the presence of binaries with separations of $a < 0.01$ pc and masses $M > 10^9 M_\odot$ out to a distance of about 25 Mpc, and with masses $M > 10^{10} M_\odot$ out to a distance of about 1 Gpc.

In any case, future successful detections with both of these experiments will need to be complemented with observations in the electromagnetic spectrum in order to fully localise and characterise the sources. For LISA, which can be thought of as two independent detectors, the triangulation of the signal is very limited; an additional detector, placed far from these other two, is required to use the standard time-of-flight method. Nevertheless, for mergers around the peak of star formation ($z \approx 2$), LISA will be able to locate mergers within 100 square degrees on the night sky at least 24 hours before the actual merger, allowing telescopes to search for counterparts (Amaro-Seoane et al., 2013).

Furthermore, with PTAs it is not possible to get particularly accurate sky locations, as the angular resolution of a given timing array experiment depends upon the number of pulsars in the array, the timing precision and the distribution of the pulsars on the sky. For example, with 100 pulsars uniformly distributed on the sky, if a source is detected with a signal to noise ratio of 10, the source position could be determined to within ∼40 square degrees (Sesana and Vecchio, 2010).

1.1.1 Binaries in the realm of observations

Despite the fairly solid theoretical predictions, observational evidence of SMBHB existence is sparse. This could imply a very short coalescence timescale of the two black holes following the galaxy merger. Observing these objects, however, is unfortunately very challenging, as their separations cannot be resolved by current capabilities in most galactic nuclei. Conversely, there is an increasing number of detections of SMBH *pairs*. Around 20 systems with separations between $\sim$ 10 pc and $\sim$ 10 kpc are known to date. The separations imply that the SMBHs are inspiriling due to dynamical friction (see next subsection). These objects are identified because they appear as a single galaxy with two AGNs. Some examples are: the prototypical case of NGC 6240 (Komossa et al., 2003), the radio galaxy 3C75 (Hudson et al., 2006), the spiral galaxy NGC 3341 (Barth et al., 2008), the ultraluminous infrared galaxy Mrk463 (Bianchi et al., 2008), the interacting galaxy COSMOS J100043.15+020637.2 (Comerford et al., 2009), and the quasar pair J1254+0846 (Green et al., 2010), among others. All these objects have been discovered because of the presence of two resolved X- ray sources wandering in the merged galaxy.

Even though SMBHBs cannot be spatially resolved in optical and X-ray observations, high frequency radio interferometry enables the resolution of parsec scales in low redshift galaxies. In fact, the most compelling SMBHB candidate to date is the peculiar double radio core of 0402+379 (Rodriguez et al., 2006). The two flat-spectrum radio sources, corresponding to the two components of the candidate SMBHB, have a projected separation of $\sim$ 7 pc. This technique, unfortunately, is not efficient for searching rare objects such as SMBHBs, because of its very limited field of view and the requirement that both SMBHs are radio-luminous.

On the other hand, several binary candidates have been proposed based on distinctive spectroscopic features. Because of the high orbital velocities (typically $\gtrsim$ 1000 km/s), sub-parsec SMBHBs have been tentatively identified by offsets of the broad line emission lines with respect to the reference provided by the narrow lines (Tsalmantza et al., 2011; Eracleous et al., 2012; Decarli et al., 2013; Ju et al., 2013; Runnoe et al., 2017). This occurs because the broad lines are generated by gas close to the SMBHs, whereas the narrow counterparts are generated at hundreds of parsecs from the central region. If the SMBHs have a significant velocity compared to the galaxy rest frame, and the broad emission region is bound to the individual SMBHs, then broad lines will have an extra redshift/blueshift compared to the reference frame of the galaxy. Note that the broad lines might be generated within a putative circumbinary disc for a very compact SMBHB (Lu et al., 2016), questioning this interpretation. Additionally, there are alternative interpretations for these spectral properties, such as recoiling individual SMBHs, or chance superposition of two AGNs (Dotti, Sesana, and Decarli, 2012; Bogdanović, 2015; Liu et al., 2015).

Another approach to look for SMBHBs is to study periodic variations in the luminosity of AGNs, as it might be driven by orbital motions. One of the most iconic candidates selected on this basis is the BL Lac object OJ287 (Sillanpaa et al., 1988), which showed quasi-periodic optical outbursts at intervals of 12 years, with the physical interpretation of the burst being the secondary black hole passing through the accretion disc of the primary (see e.g. Valtonen et al., 2011). Recently, year-like periodicities have been examined for AGNs using the Catalina, Pan-STARRS and Palomar Transient Factory archives. Exploring the light curves of hundreds of thousands of objects, only five apparently well established periodic cases have been found (Graham et al., 2015a; Liu et al., 2015; Charisi et al., 2016; Li

et al., 2016; Zheng et al., 2016) and ~ 100 are considered as promising candidates. The most compelling case is the quasar PG 1302–102 (Graham et al., 2015a). The optical light curve of this object shows a strong 5.2 year periodic signal, detected over a period of ≈ 20 years. Although the interpretation of this phenomenon is still uncertain, the most plausible mechanisms involve a binary system of two supermassive black holes with a sub-parsec separation (D'Orazio et al., 2015; D'Orazio, Haiman, and Schiminovich, 2015; Graham et al., 2015b). Future surveys such as the Large Synoptic Survey Telescope (LSST; Ivezic et al., 2008), PLATO 2.0 and the Zwicky Transient Facility (Smith et al., 2014) promise to expand time domain studies even further. Unfortunately, for most of the candidates the observed variability can be explained also with alternative scenarios that do not require a SMBHB, such as a warped accretion disc, or intrinsic jet variability, among others (see e.g. Villforth et al., 2010; Graham et al., 2015b; Sandrinelli et al., 2016).

All of the detection methods mentioned up to this point require at least one of the components of the SMBHB to be active. In order to trace the population of inactive binaries, Liu, Li, and Chen (2009) proposed to use the temporary activity coming from the accretion of a tidally disrupted star. As the presence of a second black hole temporarily interrupts the stellar debris stream on the primary, it causes characteristic dips in the tidal disruption light-curve. This signature has been identified in the light-curve of SDSS J120136.02+300305.5, which is consistent with the presence of a $\sim 10^7 M_\odot$ binary with an orbital separation of $\sim 6 \times 10^{-4}$ pc (Liu, Li, and Komossa, 2014). This analysis was also recently applied to the superluminous supernova candidate ASASSN-15lh by Coughlin and Armitage (2017). They show that its features, including an anomalous re-brightening, are consistent with the tidal disruption of a star by a supermassive black hole in a binary system. Additionally, Brem et al. (2014) showed that TDEs by one binary member have a characteristic signature in the emission of the circumbinary disc after the flare. They propose a novel method of identifying these systems using reverberation mapping.

In order to increase the number of known candidates, and/or to confirm their interpretation, it is therefore of fundamental importance to identify new signatures of SMBHBs. The simultaneous observation of various signatures could represent the only way to firmly validate the binary scenario in the known candidates. These signatures can also complement future GW observations with LISA or PTAs to improve the localisation and characterisation of the source, which are challenges for these forthcoming experiments. As SMBHBs seem to be linked in fundamental ways to the dynamics of the stellar and gas components of galaxies, understanding each step of their evolution is very important to potentially identify new observational signatures (see Colpi and Dotti, 2011, and references therein).

1.1.2 The binary's path to coalescence

The first theoretical approach to the evolution of a pair of SMBHs after their host galaxies merge was presented by Begelman, Blandford, and Rees (1980). They propose the existence of three main phases along their path to coalescence: an early phase of pairing under dynamical friction against the background matter, which ends when the system is close enough to form a Keplerian binary; a phase of hardening during which the binary separation decreases due to energy loss by close encounters with single stars; and finally a phase of gravitational wave inspiral, ending with the coalescence of the two black holes. A diagram illustrating the timescales involved in these different phases is shown in Fig. 1.3.

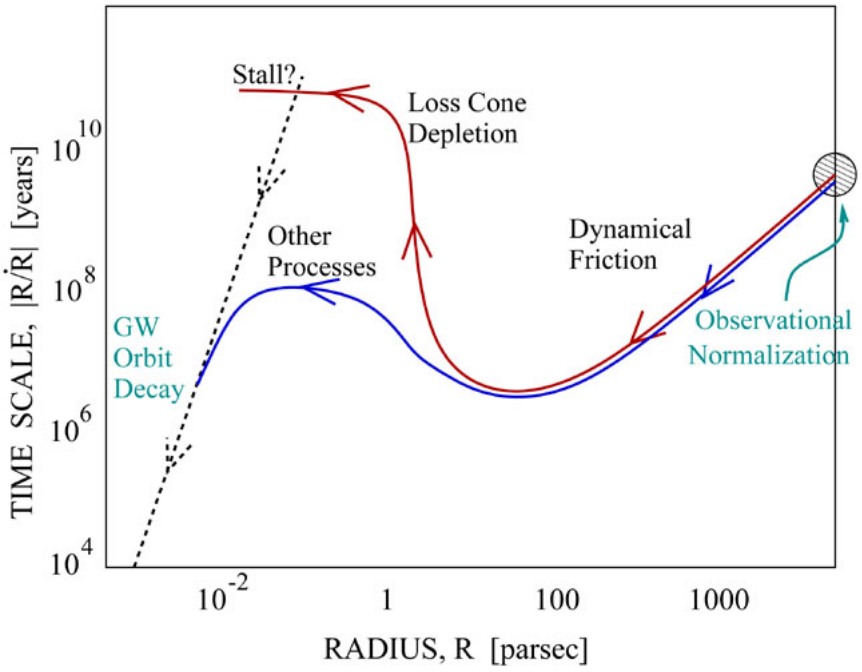

FIGURE 1.3: Diagram of the timescales involved in the path to coalescence of a SMBHB. After the galaxy merger, both black holes sink due to dynamical friction, until they form a Keplerian binary. Further hardening proceeds due to the ejection of single stars (or other processes), up to the point where GW emission takes over and the binary promptly merges. Figure adapted from Begelman, Blandford, and Rees (1980) by Backer, Jaffe, and Lommen (2004).

For GWs to carry away enough energy to finally coalesce the SMBHB within a Hubble time, both objects have to reach a separation of

$$a_{\rm GW} \sim 2 \times 10^{-3} f(e)^{1/4} \frac{q^{1/4}}{(1+q)^{1/2}} \left(\frac{M}{10^6 M_\odot} \right)^{3/4} \text{ pc}, \tag{1.1}$$

where M is the total binary mass, q is the mass ratio and

$$f(e) = \left(1 + \frac{73}{24} e^2 + \frac{37}{96} e^4 \right) (1 - e^2)^{-7/2} \tag{1.2}$$

is a strong function of the binary eccentricity e (Peters and Mathews, 1963). This equation clearly implies scales below milli-parsecs, which is extremely small compared to the expected initial separation after the galaxy merger. In consequence, the journey of the SMBH pairs is one that traverses several orders of magnitude to reach coalescence, and different mechanisms will be at play depending on their relative separation and the galaxies' properties.

For instance, after a dry merger, both SMBHs sink towards the galactic nucleus on short timescales due to dynamical friction against the surrounding background of dark matter and stars (Chandrasekhar, 1943; Milosavljević and Merritt, 2001). Assuming a distribution of N stars in a single isothermal sphere, with velocity dispersion σ, the dynamical friction timescale for each SMBH with mass $M_{\rm BH}$ can

be written as

$$t_{\rm df} \sim 2 \times 10^8 \frac{1}{\ln N} \left(\frac{M_{\rm BH}}{10^6 M_\odot} \right)^{-1} \left(\frac{r}{100\,{\rm pc}} \right)^2 \left(\frac{\sigma}{100\,{\rm km\,s^{-1}}} \right) \ {\rm yr}. \tag{1.3}$$

Note that this equation implies that the dynamical friction timescale decreases with the distance from the galaxy's nucleus, hence its action increases efficiency as the pair sinks towards the centre of the remnant. Additionally, this process depends on the pair's mass ratio: equal-mass mergers will result in a rapid formation of a SMBHB, while very unequal mergers would leave the less massive SMBH wandering in the outskirts of the remnant. This fact has been confirmed by numerical studies such as the one of Callegari et al. (2009), where they found a critical mass ratio of $q \gtrsim 1/10$ for the SMBHB formation in gas-rich galaxies, and $q \gtrsim 1/4$ for the gas-poor counter-parts.

The pairing process, however, becomes inefficient when the mass enclosed in the orbit of the two SMBHs is of the order of their total mass (M), which can be expressed as

$$a_{\rm BHB} \sim \frac{GM}{2\sigma^2} \sim 0.2 \left(\frac{M}{10^6 M_\odot} \right) \left(\frac{\sigma}{100\,{\rm km\,s^{-1}}} \right) \ {\rm pc}. \tag{1.4}$$

At this point, when the pair forms a gravitationally bound binary, the relative velocity of the two black holes becomes larger than the velocity dispersion of the background medium, and the efficiency of dynamical friction drops sharply. If the mass of the two black holes follows the $M_{\rm BH}$-σ relation (see Fig. 1.1) this expression can be written just in terms of the binary mass

$$a_{\rm BHB} \sim 0.5 \left(\frac{M}{10^6 M_\odot} \right)^{1/2} \ {\rm pc}. \tag{1.5}$$

Beyond this point, the further evolution and the final fate of the SMBHs strongly depends on the content and distribution of both gas and stars in the galactic nucleus. In figure 1.3 this can be seen as the branching out of the red and blue lines. Different processes can change dramatically the hardening timescale, even resulting in values higher than the Hubble time. Even though there is some indirect evidence that these binaries coalesce into a single object, such as the low scatter in the $M - \sigma$ relation (Kormendy and Ho, 2013), the processes involved are not completely understood. In the following subsections I describe the current understanding of the dynamical evolution of SMBHBs in different environments.

Dynamical evolution in gas-poor environments

In a gas-poor environment, the binary will continue hardening by ejecting single stars via three-body encounters. A star intersecting the SMBHB orbit experiences a chaotic three-body interaction, being eventually ejected to infinity through the slingshot mechanism. Extensive scattering experiments (e.g. Mikkola and Valtonen, 1992; Quinlan, 1996; Sesana, Haardt, and Madau, 2006) have shown that each encounter can carry away an average specific energy of

$$\Delta E \approx \frac{3}{2} \frac{q}{(1+q)^2} \frac{GM}{a}. \tag{1.6}$$

This corresponds to an increase in the binding energy of the binary, and consequently a decrease in the semimajor axis of the order

$$\frac{\Delta a}{a} \sim \frac{\Delta E}{E} \sim \frac{m}{M}, \tag{1.7}$$

where m is the mass of an individual star (Merritt and Milosavljević, 2005).

One of the first descriptions of this process was outlined by Quinlan (1996), where he considers the evolution of a SMBHB in a fixed stellar background. Assuming an interaction rate given by $\Gamma = n\Sigma v$, where n is the number density of stars, Σ the binary's cross section and v the typical velocity, he showed that the evolution of the semimajor axis is given by

$$\frac{\mathrm{d}a}{\mathrm{d}t} = -H\frac{G\rho}{\sigma}a^2, \tag{1.8}$$

where H is a dimensionless hardening rate, which reaches an approximately constant value $H \approx 15$ when the binary is already hard (equation 1.4), independent of the mass, mass ratio and eccentricity of the system. This result implies that the bound binary hardens at a constant rate in a *constant* density background, and it translates to a hardening timescale of

$$t_{\mathrm{hard}} \sim 70 \left(\frac{\sigma}{100\,\mathrm{km\,s^{-1}}}\right)\left(\frac{\rho}{10^4 M_\odot\,\mathrm{pc^{-3}}}\right)^{-1}\left(\frac{a}{10^{-3}\,\mathrm{pc}}\right)^{-1}\ \mathrm{Myr}. \tag{1.9}$$

This timescale is less than a Hubble time for a wide interval of stellar densities and velocity dispersions, and thus predicts an efficient coalescence of the SMBHB.

However, this idealised picture severely underestimates the true hardening rate because it ignores the depletion of the so-called "binary loss cone". In an extended stellar system, only a fraction of stars would have orbits intersecting the SMBHB orbit. The loss cone is the region in phase-space populated by stars with sufficiently low angular momentum J to interact with the binary, which can be estimated as

$$J^2 \lesssim 2GMa. \tag{1.10}$$

In a non-fixed stellar background, as stars are ejected, the binary loss cone is depleted. As the stellar mass contained in the loss cone of a typical galaxy is less than the mass required to significantly change the binary orbital energy, the orbit shrinks at a much lower rate once the loss cone is emptied (Milosavljević and Merritt, 2003). Whether the binary can continue to evolve by ejecting stars then depends on the efficiency at which stars are fed into the loss cone. In a spherical system, the loss cone refilling proceeds via two-body relaxation, which is usually longer than the Hubble time, hence the depletion of the orbital population inside the loss cone may lead to a stalling in the decay rate, an issue called the "final parsec problem" (see, e.g. Milosavljević and Merritt, 2001; Yu, 2002).

However, in the past decade, several semi-analytical and numerical works have shown that in the non-relaxed, triaxial rotating remnant of a galaxy merger, the supply of stars to the SMBHB should be large enough to lead to a final coalescence on a Gyr timescale (Berczik et al., 2006; Sesana, 2010; Preto et al., 2011; Khan, Just, and Merritt, 2011; Khan et al., 2013; Holley-Bockelmann and Khan, 2015; Vasiliev, Antonini, and Merritt, 2015; Sesana and Khan, 2015). In a triaxial potential, the stellar orbits do not conserve any of its angular momentum components, generating a family of "centrophilic" orbits, which can get arbitrarily close to the binary and

continue the hardening process (Poon and Merritt, 2004; Merritt and Vasiliev, 2011). One of the most recent studies by Gualandris et al. (2017), using a novel numerical technique, finds that the loss cone is efficiently replenished even in very mildly triaxial models (with axis ratios 1:0.9:0.8). With their results they conclude that there is no final parsec problem.

Another factor that can change the picture is the binary's eccentricity evolution. As seen in equation (1.1), this parameter plays an important role in the emission of GWs and the possible final fate of the binary. Additionally, even though the loss of energy through gravitational radiation will rapidly lead to circularisation of the binary orbit, any residual eccentricity at the moment of merger will imprint a characteristic waveform, identifiable with the future experiments described above.

The eccentricity evolution is usually described as

$$\frac{\mathrm{d}e}{\mathrm{d}\ln(1/a)} = K, \tag{1.11}$$

where K is a dimensionless parameter that depends on the binary mass ratio and eccentricity, in contrast with the hardening rate H (Quinlan, 1996). Typically K is positive, implying an eccentricity growth during the shrinking process. Sesana (2010), using three-body scattering experiments, constructed evolutionary tracks for binaries embedded in a surrounding distribution of stars. The general trend observed is that nearly circular and equal mass SMBHBs experience just a mild eccentricity growth, whereas systems initially eccentric or with mass ratios significantly lower than 1 can evolve up to $e > 0.9$. This behaviour was also found in full N-body simulations (Milosavljević and Merritt, 2001; Merritt, Mikkola, and Szell, 2007; Hemsendorf, Sigurdsson, and Spurzem, 2002; Aarseth, 2003; Amaro-Seoane, Miller, and Freitag, 2009; Amaro-Seoane et al., 2010), although the relatively low resolution they can afford makes the results susceptible to noise.

In view of these results, the overall picture favours an efficient coalescence of SMBHBs in dense stellar environments. The triaxial and rotating nature of the stellar merger remnants promotes efficient loss cone refilling, while large eccentricities (especially in unequal mass systems) shorten the gap between the binary pairing and the efficient GW emission stage. In the near future, massive N-body simulations with several million particles will offer a unique opportunity to confirm this scenario.

Dynamical evolution in gas-rich environments

The picture can be quite different for SMBH pairs within gas-rich environments. In this case, interaction with gas can be very efficient in absorbing and transporting outwards the angular momentum of the pair, leading to a more rapid evolution and eventual coalescence.

Different numerical studies have shown an orbital decay, driven mainly by dynamical friction, on timescales of only $\sim 10^6$ yr within the massive, rotationally supported, gaseous nuclear disc that forms after a gas-rich galaxy merger (Escala et al., 2004; Escala et al., 2005; Dotti et al., 2007; Mayer et al., 2007; Dotti et al., 2009). Figure 1.4 shows a multi-scale hydrodynamical simulation of an equal-mass galaxy merger, developed by Mayer et al. (2007). In this gas-rich merger the two black holes sink to the centre of the remnant on short timescales due to the gravitational torques exerted by the massive circumnuclear disc formed during the interaction.

When these circumnuclear discs are unstable to their own-self gravity, massive clumps develop through gravitational collapse. As they masses segregate, these

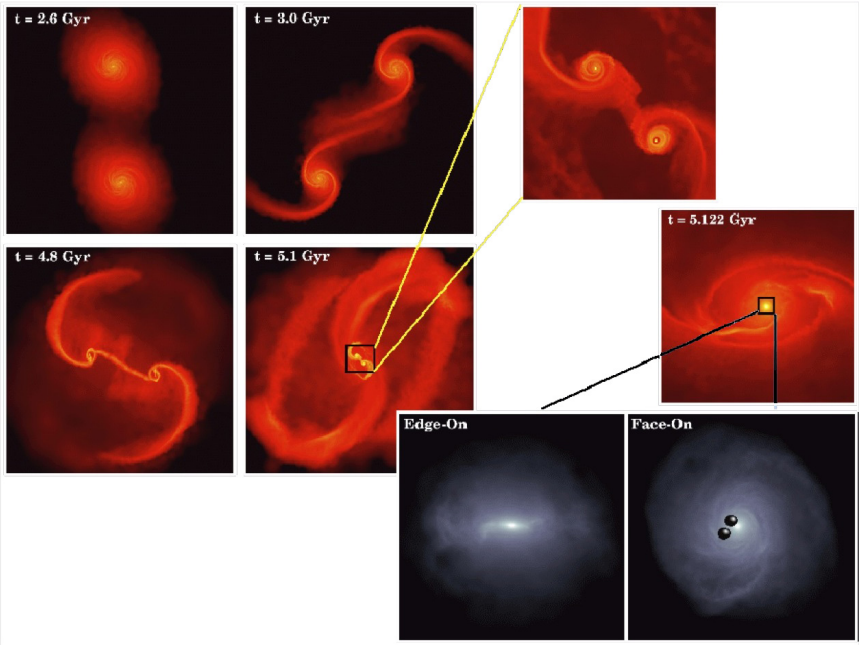

FIGURE 1.4: Density maps of the different stages of an equal-mass gas-rich galaxy merger. By the end of the multi-scale simulation, the binary is embedded in a very massive circumnuclear disc in the centre of the galaxy remnant. Figure from Mayer et al. (2007).

clumps act as massive perturbers and stochastically evolve the binary orbit through impulsive exchanges of energy and angular momentum. The stochastic behaviour of the orbit resulting from the incoherence of these torques typically enlarges the decay timescale reaching up to 50 Myr (Fiacconi et al., 2013; Roškar et al., 2015; del Valle et al., 2015; Lupi et al., 2015). This suggests that accurately describing the cold clumpy phase of the interstellar medium in nuclear discs is important to predict the black hole dynamics (and probably will continue to be important once the bound binary has formed, see next subsection). In any case, the results drawn from these numerical studies indicate that the pairing phase of two SMBHs in gas-rich mergers can occur, efficiently driven by the global disc torques of the massive circumnuclear disc.

Once the SMBHs form a compact enough, bound binary, its gravitational torque is expected to open up a cavity (also referred to as gap) in the gas distribution (e.g., Artymowicz and Lubow, 1994; del Valle and Escala, 2012; del Valle and Escala, 2014). In this scenario, the binary will naturally end up surrounded by a corotating disc. Viscous torques in the disc oppose the gas clearing, ensuring a strong coupling with the binary. Under these conditions, the binary enters a regime of orbital decay similar to the Type II migration in planetary systems, where the inner edge of the disc follows the hardening of the binary orbit (Gould and Rix, 2000; Artymowicz and Lubow, 1994). If the size of the gap is denoted by $\delta(t)$, then $\delta_{\rm pro} \sim 2a(t)$ for a corotating gaseous disc. It is important to mention that this relation only holds up when the viscous timescale of the disc is shorter than the migration timescale of the binary orbit, which is not necessarily true during the entirety of the merging process – at some point during the GW emission regime the binary evolution could be fast enough that it "decouples" from the surrounding disc, meaning that the latter cannot any longer follow the shrinkage of the orbit.

The decay timescale of a binary surrounded by this disc can be estimated as

$$t_{\rm decay} \sim \frac{M_{\rm edge} + M_2}{M_{\rm edge}} t_\nu, \tag{1.12}$$

where $M_{\rm edge}$ is an estimate of the mass in the disc's inner edge that is directly interacting with the secondary SMBH (M_2), and t_ν is the viscous timescale in that region. This expression directly relates the binary's orbital evolution to the fate of the circumbinary disc, as the amount of available mass will determine whether the decay accelerates or decelerates. When $M_{\rm edge}$ is larger than M_2, the secondary SMBH behaves like a fluid element and migrates on a viscous timescale, whereas when the opposite occurs, the decay is significantly delayed.

These types of systems, however, appear to be more complex than previously outlined. 2D and 3D numerical simulations have shown that, even though the gravitational forces keep most of the gas cleared from the binary orbit, some material leaks through the cavity wall in the form of narrow streams that reach the black holes. Such inflowing gas can exert a net negative torque inside the cavity region, shrinking the binary more effectively than with just the resonant torques (e.g. MacFadyen and Milosavljević, 2008; Roedig et al., 2012; D'Orazio, Haiman, and MacFadyen, 2013; Tang, MacFadyen, and Haiman, 2017).

To tackle this problem, many theoretical and numerical studies have focused on the evolution of a sub-parsec binary surrounded by a coplanar, corotating circumbinary disc (e.g., Ivanov, Papaloizou, and Polnarev, 1999; Armitage and Natarajan, 2005; Cuadra et al., 2009; Haiman, Kocsis, and Menou, 2009; Lodato et al., 2009; Nixon et al., 2011; Roedig et al., 2011; Roedig et al., 2012; Kocsis, Haiman, and Loeb, 2012; Amaro-Seoane, Brem, and Cuadra, 2013; Roedig and Sesana, 2014; Dunhill, Cuadra, and Dougados, 2015), typically finding a very slow orbital evolution. For instance, Cuadra et al. (2009) estimated that, surrounded by a massive disc on the verge of fragmentation, binaries with mass $M < 10^7 M_\odot$ have migration times of $\sim 10^8$ yr, while heavier binaries would instead stall, and/or decay via three-body encounters of stars (the latter option was explored by Amaro-Seoane, Brem, and Cuadra, 2013). They demonstrated that such massive structures can shrink the binary orbit because the disc's own gravity acts as an effective viscosity by transporting angular momentum. The analytical estimates done by Cuadra et al. (2009) were confirmed using a numerical simulation, as shown in Fig. 1.5.

Similarly, the eccentricity evolution has also been considered. The observed tendency of this parameter is to increase during interaction with the prograde disc (Armitage and Natarajan, 2005; MacFadyen and Milosavljević, 2008; Roedig et al., 2011). Further analysis has revealed that such excitation cannot grow indefinitely, as saturation occurs due to the interaction of the secondary black hole with gas near the inner rim of the disc body, and to the accumulation of gas around the black holes in the mini-discs (Roedig et al., 2011). The process reaches saturation around $e \sim 0.6 - 0.8$.

Note that the discussion above assumes a corotating disc with respect to the SMBHB. In realistic scenarios, however, this picture could change. If the surrounding gaseous envelope fails in bringing the two SMBHs to the final coalescence, the circumnuclear disc resulting from the galaxy merger is likely to be consumed by star formation and/or feedback (see e.g. Lupi et al., 2015). In one of these cases, inflows of gas could happen with a random angular momentum orientation, resulting in a retrograde circumbinary disc (Nixon, King, and Pringle,

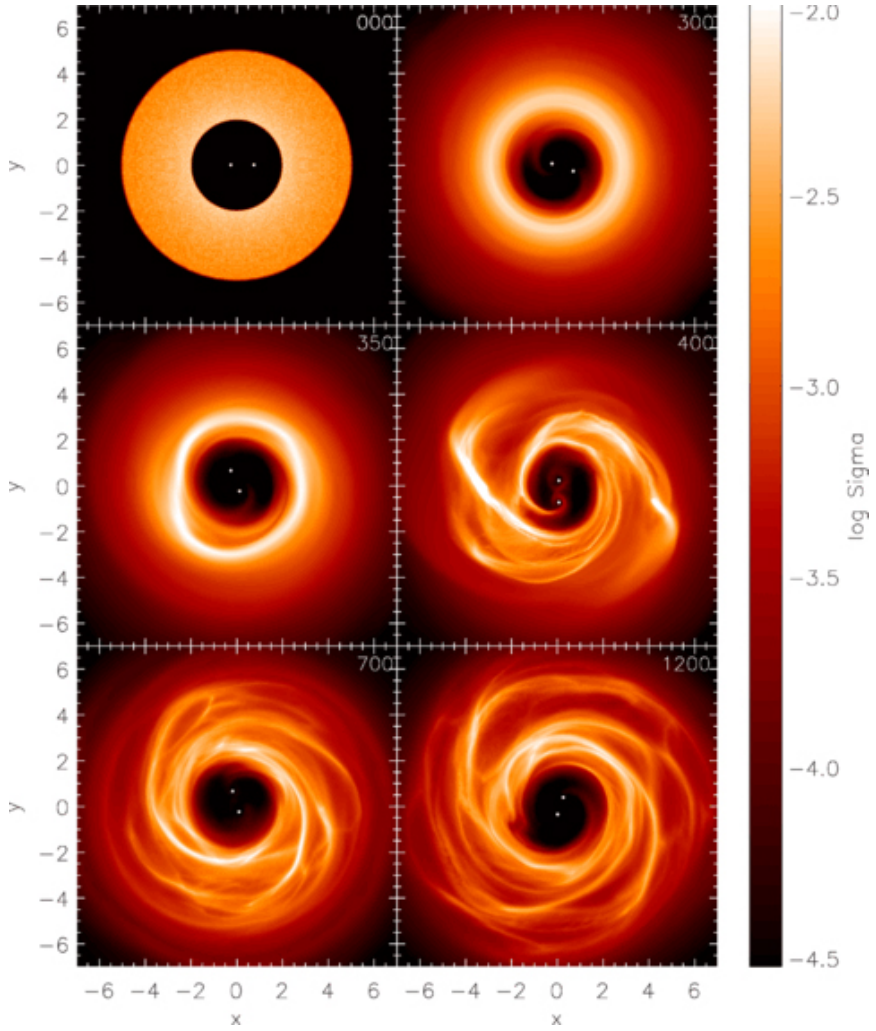

FIGURE 1.5: Column density maps of the evolution of a SMBHB in a prograde circumbinary disc. The binary has a mass ratio of $q = 1/3$, while the disc mass is $M_{\rm disc} = 0.2M$. The persistent spiral arms, developed because of the disc's self-gravity, are able to torque the binary, transporting angular momentum outwards. Figure from Cuadra et al. (2009).

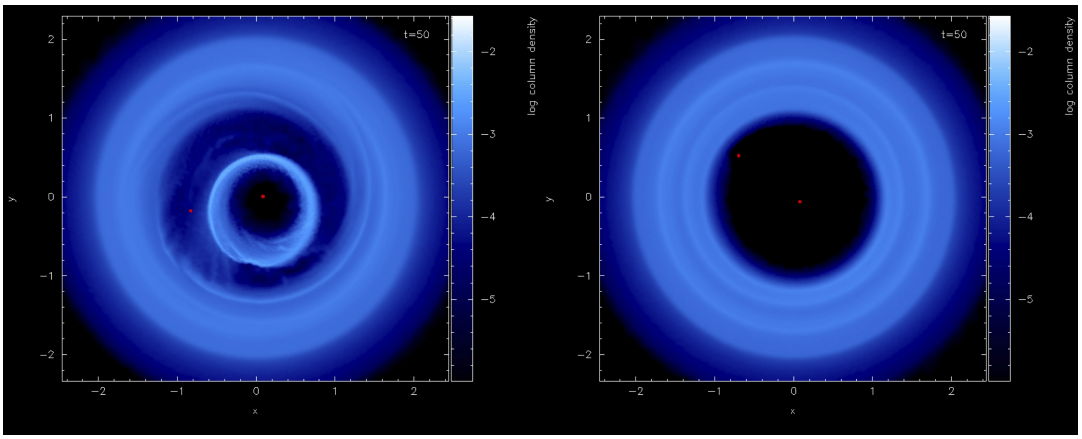

FIGURE 1.6: Column density maps of a SMBHB in retrograde circumbinary discs. In both panels the binary has a mass ratio of $q = 1/10$, the difference being the size of the secondary's accretion radius, which determines the amount of gaseous material captured by each SMBH. The total disc mass is $M_{\rm disc} = 10^{-2}M$, hence its self-gravity is negligible. Figure from Nixon et al. (2011).

2011).

Motivated by this fact, Roedig and Sesana, 2014, as well as Nixon and collaborators (see, e.g. Nixon et al., 2011; Nixon, King, and Price, 2013; Nixon and Lubow, 2015), have extensively investigated the binary interplay with misaligned or counter-rotating discs. In Figure 1.6 there is an example of the numerical experiments developed by Nixon et al. (2011), where a binary evolves embedded in a coplanar, counter-rotating circumbinary disc. Interaction with a retrograde disc can be considerably more effective in shrinking the binary due to the absence of orbital resonances that brings the gas much closer ($\delta_{\rm retro} \sim a(t)$). With this configuration, the binary directly absorbs negative angular momentum through gas capture and accretion, especially by the secondary black hole, being nearer to the cavity's edge. In many cases the binary orbit becomes eccentric, shortening the pericentre distance as the eccentricity grows. In all cases the binary coalesces once it has absorbed the angular momentum of a gas mass comparable to that of the secondary black hole. Nixon et al. (2011) discusses that the coalescence timescale is therefore $\sim M_2/\dot{M}$, where $\dot{M}$ is the inflow rate through the circumbinary disc, which is considerably faster than the migration timescales inferred for similar prograde discs.

Nevertheless, relaxed steady discs are often assumed as initial condition. In all the aforementioned studies, the evolution of the SMBHB is "decoupled" from the host galaxy, in the sense that there is no attempt to model the formation of the circumbinary disc structure, nor to link it to the fuelling mechanisms that transport gas from galactic scales down to the binary. Additionally, all these scenarios are subject to the disc consumption problem, namely, if the disc dissolves through some process (e.g. star formation, AGN/supernovae feedback), the hardening of the binary orbit stops. Consequently, the final fate of SMBHBs is intimately related to the unsolved problem of the black hole feeding in galactic nuclei.

1.2 Clumpy accretion onto supermassive black holes

The fuelling of gaseous material onto galactic nuclei is currently a critical, yet uncertain piece in the galaxy formation puzzle. Such inflows ultimately generate phenomena as diverse as starbursts and ultraluminous infrared galaxies (ULIRGs), nuclear stellar clusters and accretion onto SMBHs. However, the wide range of physical scales involved makes the fuelling a very complex process – the gas needs to lose its angular momentum efficiently to be transported from galactic scales down to the nuclear region.

There are several known mechanisms that can produce inflows on galactic scales. For instance, galaxy mergers produce strong non-axisymmetric perturbations that can drive material inwards, especially during major mergers. Such disturbances may also be produced in some globally unstable, self-gravitating isolated galactic discs. Observationally, major mergers are associated with enhancements in star formation in ULIRGs and submillimetre galaxies (e.g. Sanders et al., 1988; Sanders and Mirabel, 1996; Dasyra et al., 2006a; Dasyra et al., 2006b; Woods, Geller, and Barton, 2006; Veilleux et al., 2009). Numerical simulations of mergers have shown that when such events occur in gas-rich galaxies, resonant tidal torques lead to rapid inflow of gas into the central kiloparsec (kpc; Hernquist, 1989; Barnes and Hernquist, 1991; Hernquist and Barnes, 1991; Barnes and Hernquist, 1996).

However, the physics of how gas is transported from kpc scales to much smaller scales remains uncertain (Goodman, 2003). Typically, the large-scale torques produced by the galactic structure become less efficient at sub-kpc scales. In the case of stellar bars or spiral waves, there can even be a hard barrier to further inflow in the form of an inner Lindblad resonance, if the system has a complex, axisymmetric bulge. In mergers, the coalescence of the two systems generates perturbations on all scales, and so it allows gas to move through the resonances, but the perturbations relax rapidly on small scales, often before gas can inflow (Hopkins and Quataert, 2010; Hopkins and Quataert, 2011).

A plausible mechanism that could break this angular momentum barrier is provided by chaotic feeding or ballistic accretion of cold streams when the gas is cold enough to form dense clouds or filaments. This gas can travel easily through the interstellar medium, reaching the galactic nuclei almost unaffected by hydrodynamical drag. Cold accretion onto black holes has long been predicted by both theory and simulations. The possible relevance of discrete and randomly oriented accretion event was first highlighted by King and Pringle (2006) (see also King and Pringle, 2007; Nayakshin and King, 2007; Nayakshin, Power, and King, 2012), which they referred to as "chaotic accretion" scenario. They argue that a series of gas pockets falling from uncorrelated directions could explain the rapid growth of SMBHs across cosmic time, and reproduce some of the observed properties (e.g. the $M_{\rm BH} - \sigma$ relation).

Cosmological simulations have shown that cold streams may be important for supplying relatively low angular momentum gas to galaxies (e.g. Dubois et al., 2012; Bellovary et al., 2013; Prieto et al., 2017), while higher resolution simulations that resolve the regions nearer to SMBH suggest that similar processes may operate on smaller scales (Levine, Gnedin, and Hamilton, 2010; Curtis and Sijacki, 2016). Furthermore, the numerical study of Hobbs et al. (2011) shows that turbulence in a quasi-spherical distribution of gas leads to the formation of convergent flows that create high-density filaments. The latter can travel almost ballistically through the rest of the bulge, with some portions arriving in the inner parsecs of the galaxy. Even though most of the gas ends up in a galaxy-scale disc with a large angular

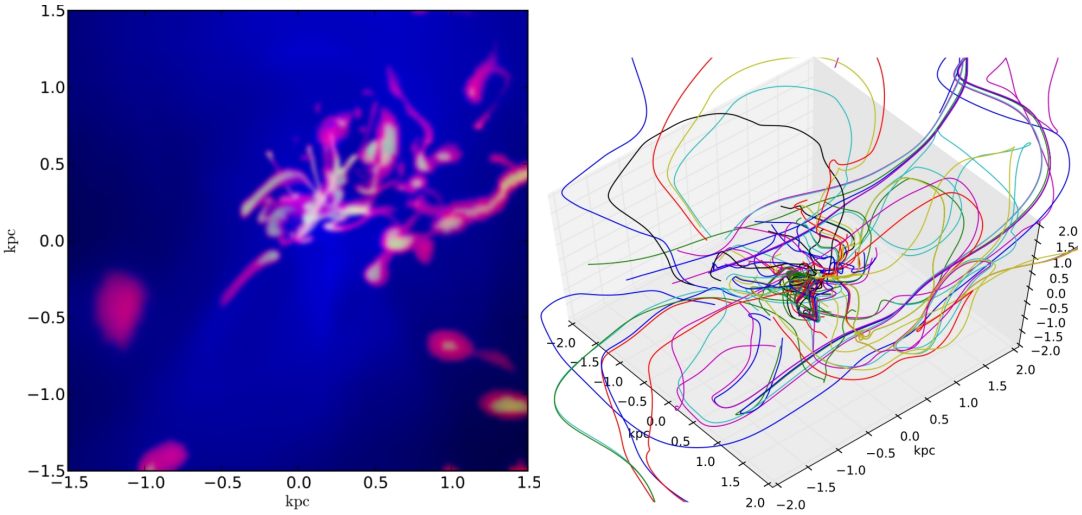

FIGURE 1.7: Cold chaotic accretion onto a SMBH from the condensation of a hot halo with turbulence, cooling, AGN heating and rotation. *Left:* Composite image tracing the hot plasma (blue), warm gas (red) and cold gas (green). Warm and cold clouds coalesce, forming a network of filaments and giant associations. *Right:* A sample of stream lines integrated from the outer kpc region. This shows the chaotic dynamics of the cold phase gas. Both Figures are from Gaspari, Temi, and Brighenti (2017).

momentum, the SMBH receives most of its fuel from the gas filaments and clumps arriving at its vicinity directly. The large spread in angular momentum achieved with turbulence randomises the direction of the accretion events.

One of the most extensive efforts to study the evolution of multiphase gaseous haloes and its impact on SMBH accretion is the work of Gaspari and collaborators (Gaspari, Ruszkowski, and Sharma, 2012; Gaspari, Ruszkowski, and Oh, 2013; Gaspari, Brighenti, and Temi, 2015; Gaspari and Sądowski, 2017; Gaspari, Temi, and Brighenti, 2017). They have shown that realistic turbulence, cooling, and heating affecting the hot halo, can dramatically change the accretion flow onto black holes, departing from the idealised picture of the Bondi prescription (Bondi, 1952). Under certain physical conditions, cold clouds and filaments condense out of the hot phase due to thermal instabilities. Chaotic collisions promote the funnelling of the cold phase towards the SMBH, leading to episodic spikes in the accretion rate. An example of the results of one of their numerical experiments is shown in Fig. 1.7, where cold and chaotic clumps form in a hot halo with turbulence, cooling, AGN heating and rotation.

A perhaps more concrete example of this kind of discrete accretion events is the putative cloud that resulted in the unusual distribution of stars orbiting our Galaxy's SMBH. Several numerical studies have shown that portions of a near-radial gas cloud infall can be captured by a SMBH to form one or more eccentric discs that eventually fragment to form stars (Bonnell and Rice, 2008; Hobbs and Nayakshin, 2009; Alig et al., 2011; Mapelli et al., 2012; Lucas et al., 2013, see Fig. 1.8 for an example), roughly reproducing the observed stellar distribution (Paumard et al., 2006; Lu et al., 2009). An interesting feature of these observed stellar discs is that they appear to be misaligned with respect to the Galactic plane, which implies that the infalling gas had an angular momentum direction unrelated to that of the large scale structure of the Galaxy.

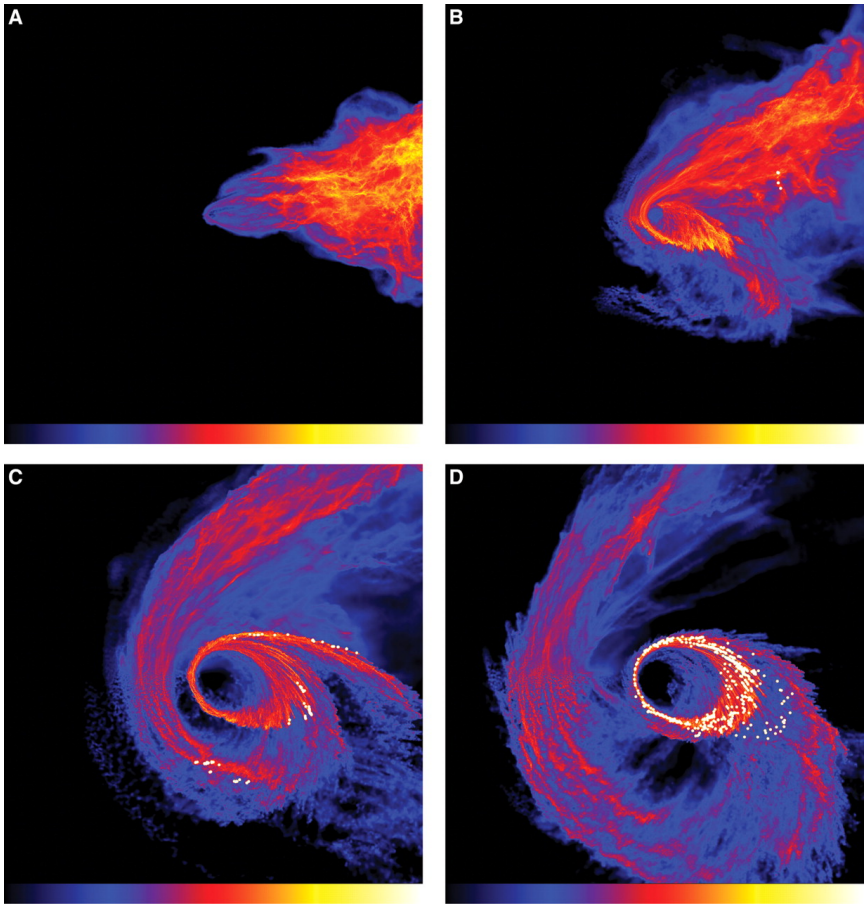

FIGURE 1.8: The evolution of a molecular cloud falling towards a supermassive black hole. The color code represents column density in logarithmic scale. Some of the gaseous material that is captured by the SMBH fragments to form stars, which are represented with white circles. The final product of this process (panel D) is an eccentric disc of stars, resembling the distribution observed around Sgr A*. Figure from Bonnell and Rice (2008).

From an observational perspective, the development of multi-wavelength observations has started to unveil the multiphase structure of massive galaxies, hosting considerable amounts of ionised, neutral and molecular gas, in addition to the hot plasma halo. In the optical, there are elliptical galaxies sitting at the core of groups and clusters that present filaments and clouds of warm gas ($\approx 10^4$ K) up to 10 kpc from the centre, which are tightly correlated with soft X-ray and far-ultraviolet emission (see Tremblay et al., 2015, and references therein). Aside from filamentary structures, this gas is also found in a coherent rotating structure, which is typically correlated with more quiescent systems (Hamer et al., 2016).

Massive galaxies also harbour neutral and molecular gas down to $\sim$10 K (e.g. Combes, Young, and Bureau, 2007). The Atacama Large Millimetre Array (ALMA) has opened up the gate to high-resolution detections of molecular gas in early-type galaxies. For instance, there have been observations of giant molecular associations in the NGC5044 group within $r \lesssim 4$ kpc, inferred to have chaotic dynamics (David et al., 2014). In massive galaxy clusters, ALMA has detected molecular hydrogen in the core of the Abell 1835 galaxy cluster (McNamara et al., 2014), which may be supported in a rotating, turbulent disc oriented nearly face-on. In the Abell 1664 cluster, the molecular gas shows asymmetric velocity structure, with two gas clumps flowing into the nucleus (Russell et al., 2014).

More importantly, in a recent study, Tremblay et al. (2016) reported observations that reveal a cold, clumpy accretion flow towards a supermassive black hole fuel reservoir in the nucleus of the Abell 2597 galaxy cluster, a nearby giant elliptical galaxy surrounded by a dense halo of hot plasma. They infer that these cold molecular clouds are within the innermost hundred parsecs, moving inwards at about 300 kilometres per second, likely fuelling the black hole with gaseous material. The authors claim that this is the first time a distribution of molecular clouds has been unambiguously linked with SMBH growth.

Despite these several clues suggesting that stochastic condensation of cold gas and its accretion onto the central SMBH is essential for active galactic nuclei, it has been barely explored as a possible source of gas for sub-parsec SMBHBs. A notable exception is the study of Dunhill et al. (2014) which showed that slightly misaligned infalling clouds with a large impact parameter result in prograde or retrograde circumbinary discs (see Fig. 1.9). However, their main focus was to explore a range of cloud masses and cooling rates instead of different orbital configurations for the incoming gas.

Since these clouds are expected to reach the galactic nucleus after a series of chaotic collisions, their inclination is likely to be completely uncorrelated to that of the galaxy and a putative residing binary. For that reason, it is of paramount importance to probe a variety of orbital configurations in order to really gauge the relevance of these type of discrete accretion events in the binary evolution, as well as in the formation of gaseous structures.

In this thesis I explore the hypothesis of infalling clouds as the source of gas for sub-parsec supermassive black hole binaries using numerical simulations. In particular, I concentrate on clouds with very low specific angular momentum (near-radial orbits) for a wide range of orbital configurations, namely different inclinations and pericentre distances. This thesis is arranged as follows. In Chapter 2, I summarise some of the key aspects of the numerical technique used to model the evolution of these systems. Chapter 3 explores the formation and early dynamics of discs using high-resolution simulations of a single cloud impacting on to SMBHBs, exploring different possible pericentre distances and relative inclinations. In Chapter 4, I use a similar suite of single cloud simulations to study

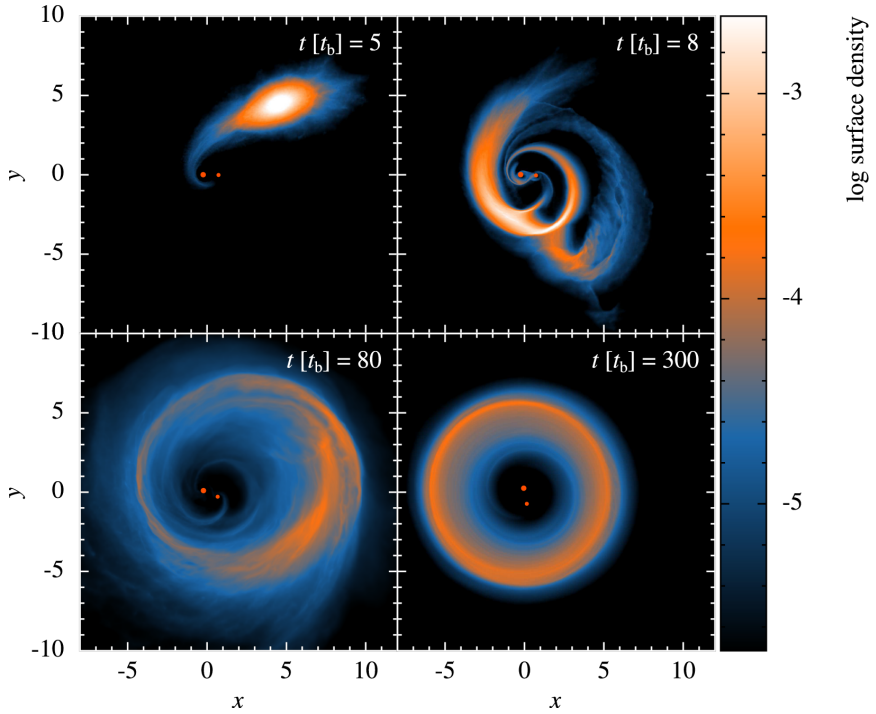

FIGURE 1.9: Surface density maps for a simulation of an infalling cloud onto a SMBHB with a mass ratio of $q = 1/3$. Both the cloud and the binary are co-rotating with a small initial misalignment of 15 degrees, thus the final product of the interaction is a prograde circumbinary disc. Figure from Dunhill et al. (2014).

the orbital response of a binary as a function of the different orbital configurations. Chapter 5 extends the single cloud models to a scenario with several incoherent gas pockets interacting with SMBHBs, which allows to measure some of the secular effects expected from the left-over gas. Finally, in Chapter 6, I discuss some of the possible future avenues for this research, as well as summarise the main results from each of the previous chapters.

Chapter 2

The Smoothed Particle Hydrodynamics technique

Throughout this thesis I present a variety of numerical models of turbulent clouds infalling onto supermassive black hole binaries to explore the implications of these type of events being common in some galactic nuclei, especially after galaxy mergers where SMBHBs are expected to form. In this chapter I present the basic aspects of the numerical technique used to simulate the binary-cloud interaction, along with the specific modifications made to the code to capture the desired physics. For more comprehensive reviews on the topic I refer the interested reader to the reviews of Springel (2010b) and Price (2012), as well as the paper presenting the public version of the code GADGET-2 (Springel, 2005).

2.1 Fundamentals

Smoothed particle hydrodynamics (SPH) was originally proposed by Lucy (1977) and Gingold and Monaghan (1977), and since then it has been widely used in several fields due to its versatility, especially in astrophysics, where it has been applied to the modelling of a variety of systems from planets to cosmological simulations. One of the most attractive properties is that the resolution naturally follows the fluid, with more detail in the dense regions, while wasting no computational time in portions where there is little to no material. Another relevant feature is its conservative nature which makes it ideal for dynamical studies, such as this project.

Formally, SPH is a Lagrangian particle method to solve the equations of hydrodynamics. In simple words, the very basic principle behind SPH is the discretisation of the fluid into particles of fixed mass. Since each point represents a portion of gas, the fluid quantities are computed over the so-called "smoothing kernel", W. In consequence, the density at each position can be estimated with the following weighted sum over the neighbouring particles $N_{\rm neigh}$

$$\rho(\boldsymbol{r}) = \sum_{i=1}^{N_{\rm neigh}} m_i W(\boldsymbol{r} - \boldsymbol{r}_i, h), \tag{2.1}$$

where h is the scale parameter of the kernel commonly referred to as "smoothing length". Note that conservation of the total mass enforces a normalisation over W given by

$$\int_V W(\boldsymbol{r} - \boldsymbol{r}_i, h) d^3\mathbf{r} = 1. \tag{2.2}$$

The accuracy of the density estimate depends on the choice of W. In order to be considered a good smoothing kernel, it must satisfy the following basic criteria:

1. To be non-negative, decrease monotonically with relative distance and have smooth derivatives.
2. Symmetry with respect to $\boldsymbol{r} - \boldsymbol{r}_i$, namely $W(\boldsymbol{r} - \boldsymbol{r}_i, h) \equiv W(\boldsymbol{r}_i - \boldsymbol{r}, h)$
3. A flat central portion so that small-scale changes in position do not strongly affect the density estimate.

The natural step would be to pick a Gaussian kernel, given that it fulfils these criteria and that it is infinitely differentiable. However, the main disadvantage is that it never goes formally to zero, requiring interaction with all the particles, which is of course computationally expensive. In practice, the most widely used are the B-spline functions, which are Gaussian-like, but truncated at a finite radius. The standard kernel used by GADGET is the cubic spline

$$W(r,h) = \frac{8}{\pi h^3} \begin{cases} 1 - 6\left(\frac{r}{h}\right)^2 + 6\left(\frac{r}{h}\right)^3 & \text{if} \quad 0 \leq \frac{r}{h} \leq \frac{1}{2}, \\ 2\left(1 - \frac{r}{h}\right)^3 & \text{if} \quad \frac{1}{2} \leq \frac{r}{h} \leq 1, \\ 0 & \text{otherwise}, \end{cases} \tag{2.3}$$

where $r = |\boldsymbol{r} - \boldsymbol{r}_i|$.

The adaptive smoothing length of each particle is determined by imposing the condition that the kernel volume contains a constant mass, which can be expressed in the following relation

$$\frac{4\pi}{3} h_i^3 \rho_i = N_{\text{neigh}} m_i, \tag{2.4}$$

where the number of neighbouring particles (N_{neigh}) is kept constant during one simulation. Throughout this project I use $N_{\text{neigh}} = 50$.

Since SPH is basically an interpolation method, it is possible to estimate the value of any arbitrary field using the distribution of sampling particles. Consider a field F and N sampling particles with positions where the value of F is known. The field at any other position can be approximated as

$$F_s(\mathbf{r}) = \int F(\mathbf{r}')W(\mathbf{r} - \mathbf{r}', h)d\mathbf{r}' + \mathcal{O}\big(h^2\big) \tag{2.5}$$

$$\approx \sum_{i=1}^{N_{\text{neigh}}} \frac{m_i}{\rho_i} F(\mathbf{r}_i)W(\mathbf{r} - \mathbf{r}_i, h). \tag{2.6}$$

One further useful feature of SPH is that the spatial derivative for any field estimated in this manner can be found simply by taking the derivative of the kernel itself. This can be simply seen from

$$\boldsymbol{\nabla} F_s(\mathbf{r}) = \frac{\partial}{\partial \mathbf{r}} \int_0^\infty F(\mathbf{r}')W(\mathbf{r} - \mathbf{r}', h)d\mathbf{r}' + \mathcal{O}\big(h^2\big) \tag{2.7}$$

$$\approx \sum_{i=1}^{N_{\text{neigh}}} \frac{m_i}{\rho_i} F(\mathbf{r}_i)\boldsymbol{\nabla} W(\mathbf{r} - \mathbf{r}_i, h). \tag{2.8}$$

This makes SPH calculations very efficient because there is no need to take derivatives during the simulation. The same is true for the divergence and curl of vector fields following the same arguments.

Using this SPH formalism, namely, a set of discrete particles as tracers to describe the state of the fluid, it is possible to solve the equations that describe the hydrodynamics: the continuity, momentum and energy equations.

The continuity equation is simply given by the SPH density estimator shown in equation (2.1).

2.2 Equations of motion

Because the particles sample the fluid in a Lagrangian sense, we can consider the following discrete Lagrangian of the entire system

$$\mathcal{L}_{\mathrm{SPH}} = \sum_i m_i \left[\frac{1}{2} v_i^2 - u_i(\rho_i, s_i) \right], \tag{2.9}$$

where v is the norm of the velocity vector $\mathbf{v} \equiv \mathrm{d}\mathbf{r}/\mathrm{d}t$, and u is the thermal energy that can be specified as a function of the thermodynamic variables ρ and s (density and entropy, respectively).

The equations of motion of such a system can be derived from the principle of least action, which translates into the well-known Euler-Lagrange equations

$$\frac{\mathrm{d}}{\mathrm{d}t} \left(\frac{\partial \mathcal{L}}{\partial \mathbf{v}} \right) - \frac{\partial \mathcal{L}}{\partial \mathbf{r}} = 0. \tag{2.10}$$

From the equation (2.9) the partial derivatives are obtained as

$$\frac{\partial \mathcal{L}_{\mathrm{SPH}}}{\partial \mathbf{v}_i} = m_i \mathbf{v}_i, \tag{2.11}$$

$$\frac{\partial \mathcal{L}_{\mathrm{SPH}}}{\partial \mathbf{r}_i} = \sum_j m_j \frac{\partial u_j}{\partial \mathbf{r}_i} = \sum_j m_j \left. \frac{\partial u_j}{\partial \rho_j} \right|_{s_j} \frac{\partial \rho_j}{\partial \mathbf{r}_i}, \tag{2.12}$$

where the important assumption of no dissipation is made, implying a constant entropy. From the first law of thermodynamics ($\mathrm{d}U = T\mathrm{d}S - P\mathrm{d}V$), the change in thermal energy is

$$\left. \frac{\partial u_j}{\partial \rho_j} \right|_{s_j} = \frac{P_j}{\rho_j^2}, \tag{2.13}$$

where P is the pressure of the fluid. From equation (2.1) the density gradient is

$$\frac{\partial \rho_j}{\partial \mathbf{r}_i} = f_j \sum_k m_k \boldsymbol{\nabla}_i W_{jk}(h_j)(\delta_{ik} - \delta_{ij}), \tag{2.14}$$

where δ is the Kronecker delta function, and where the following definitions were made:

$$\boldsymbol{\nabla}_i \equiv \frac{\partial}{\partial \mathbf{r}_i}, \tag{2.15}$$

$$W_{jk}(h_j) \equiv W(\mathbf{r}_j - \mathbf{r}_k, h_j), \tag{2.16}$$

$$f_j \equiv \left[1 - \frac{h_j}{3\rho_j} \sum_k m_k \frac{\partial W_{jk}(h_j)}{\partial h_j}\right]^{-1}. \tag{2.17}$$

Finally, by combining equations (2.13), (2.14) and (2.10), the equations of motion for the SPH particles are obtained as follows:

$$\frac{\mathrm{d}\mathbf{v}_i}{\mathrm{d}t} = -\sum_j^{N_{\mathrm{neigh}}} m_j \left[f_i \frac{P_i}{\rho_i^2} \boldsymbol{\nabla}_i W_{ij}(h_i) + f_j \frac{P_j}{\rho_j^2} \boldsymbol{\nabla}_i W_{ij}(h_j)\right]. \tag{2.18}$$

Equation (2.18) corresponds to the momentum equation of each SPH particle. From this expression it is possible to demonstrate that linear and angular momentum are conserved exactly during the simulation. The conservation properties follow directly from the symmetries in the original Lagrangian and the SPH density estimate. Linear momentum conservation follows from invariance to translations, while angular momentum conservation is due to invariance to rotations of the particle coordinates.

2.3 The energy equation

The energy equation can also be added to the Lagrangian formalism shown above. Here there is a choice of evolving either the thermal energy u, the total specific energy $e = 0.5v^2 + u$, or an entropy variable.

In the formulation of SPH used in this thesis a particle's thermal energy is not directly evolved. Instead an entropic function $A(s)$ is used, from which the internal energy is computed. For an ideal gas, the equation of state is

$$P = A(s)\rho^\gamma, \tag{2.19}$$

where γ is the polytropic index of the gas. In this way we can strictly ensure that entropy is never inadvertently decreased through errors caused by SPH estimation methods.

Provided there are no shocks or external sources of heat, the entropy A_i of each particle remains constant throughout the simulation. However, the entropic function can be evolved explicitly by adding dissipation terms. This can be made following Springel and Hernquist (2002) as

$$\frac{\mathrm{d}A_i}{\mathrm{d}t} = \frac{\gamma - 1}{\rho_i^{\gamma-1}} \left(\frac{\mathrm{d}u}{\mathrm{d}t}\right)_{\mathrm{diss}}. \tag{2.20}$$

The thermal energy is then evaluated using

$$u_i = \frac{A_i}{\gamma - 1} \rho_i^{\gamma-1}. \tag{2.21}$$

During the simulations reported in this thesis the only source of dissipation is the artificial viscosity introduced to capture shocks, as explained in the following section. Nonetheless, using this formalism, other sources can be implemented, such as radiative cooling and heating.

2.4 Artificial viscosity

Thanks to the Lagrangian nature of SPH, the equations shown above describe a flow without any *intrinsic* dissipation, where energy is not dissipated nor diffused. However, in a real astrophysical fluid this is not necessarily the case. For instance, shocks and other kinds of discontinuities are not adequately captured by the standard formulation of SPH. Dissipationless SPH also experiences problems of particle penetration, where particles become disordered and pass through one another. The absence of dissipation implies that where dissipative terms are required, they must be explicitly added.

In the case of converging flows, "artificial" terms must be added to the SPH equations to mimic the real behaviour of an astrophysical fluid, known as artificial viscosity. In practice this term causes close and approaching SPH particles to repel each other with a force that increases with the approaching velocity. The result is that particles in colliding streams are decelerated and they do not pass through each other. This will effectively smooth out any discontinuity that cannot be allowed in these type of simulations. It is referred to as "artificial" because it is not intended to replicate a physical process.

There are a number of different forms of this, and the one implemented in the code used here is that of Morris and Monaghan (1997). In this scheme, the additional term

$$\left.\frac{\mathrm{d}\mathbf{v}_i}{\mathrm{d}t}\right|_{\mathrm{visc}} = -\sum_{j}^{N_{\mathrm{neigh}}} m_j \Pi_{ij} \nabla_i \overline{W}_{ij} \tag{2.22}$$

is added to the momentum equation (2.18). Similarly, the dissipation term in equation (2.20) has the form

$$\left.\frac{\mathrm{d}u}{\mathrm{d}t}\right|_{\mathrm{diss}} = \frac{1}{2}\sum_{j}^{N_{\mathrm{neigh}}} m_j \Pi_{ij} \mathbf{v}_{ij} \cdot \nabla_i \overline{W}_{ij}. \tag{2.23}$$

Here $\overline{W}_{ij}$ is the arithmetic mean of the two particle kernels involved, $W_{ij}(h_i)$ and $W_{ij}(h_j)$, while $\Pi_{ij} \geq 0$ is the viscosity "switch", non-zero only when particles are approaching each other in physical space, and is given by

$$\Pi_{ij} = -\frac{\alpha}{2}\frac{(c_i + c_j - 3w_{ij})}{\rho_{ij}} w_{ij}, \tag{2.24}$$

where

$$w_{ij} = \begin{cases} \mathbf{v}_{ij} \cdot \mathbf{r}_{ij}/|\mathbf{r}_{ij}| & \text{if} \quad \mathbf{v}_{ij} \cdot \mathbf{r}_{ij} < 0 \\ 0 & \text{otherwise,} \end{cases} \tag{2.25}$$

is the relative velocity projected onto the separation vector, and c_i is the particle's sound speed. The strength of the viscosity is determined by the parameter α[1],

[1]Note that this parameter is not related to the α-disc model proposed by Shakura and Sunyaev (1973)

with typical values in the range $\alpha \sim 0.5 - 1.0$ (Springel, 2005). Throughout all the simulations presented in this thesis, I have set this parameter to $\alpha = 1.0$. Early tests done with these models showed a very weak dependance of the results with this parameter.

Ideally, the aim of the switch is to detect the presence of a shock, which the algorithms here interpret as any convergent flow with the condition $\mathbf{v}_{ij} \cdot \mathbf{r}_{ij} < 0$. However, this will be also true in the case of a shear flow, where the divergence is negative but the flows are not in fact converging. This problem can be reduced by employing the method devised by Balsara (1995) and Steinmetz (1996), which consists of multiplying the viscous tensor Π_{ij} with $(f_i + f_j)/2$, where

$$f_i = \frac{|\boldsymbol{\nabla} \times \mathbf{v}|_i}{|\boldsymbol{\nabla} \cdot \mathbf{v}|_i + |\boldsymbol{\nabla} \times \mathbf{v}|_i}, \tag{2.26}$$

is a simple measure for the relative amount of shear around particle i. This serves to suppress the artificial viscosity in the case where the vorticity is dominant over the convergence, for example in the case of accretion discs.

2.5 The code: GADGET-3

All the simulations presented in this thesis were performed using the N-body/SPH code GADGET-3 (in particular, the version P-GADGET3), which is an updated version of the public code GADGET-2 introduced by Springel (2005). This is a massively parallel TreeSPH code that follows the evolution of a self-gravitating collisionless N-body system together with the gas dynamics using the SPH formalism as explained above. In GADGET-3 both the force computation and the time-stepping are fully adaptive, with a dynamic range which is, in principle, unlimited. Thanks to its versatility, this code has been used to model a wide variety of astrophysical systems, even though it was originally intended for cosmological simulations.

In the following subsections I introduce some of the basic features of this code, along with the specific modifications introduced during the development of this project. For discussions and more details of the code, I refer the reader to Springel (2005).

2.5.1 The tree algorithm

Gravity is an extremely important force for the type of systems modelled in this thesis. Unfortunately, its long range nature makes its computation very challenging, especially if one needs relatively high accuracy.

To avoid the extremely high computational cost of the N^2-scaling of computing directly the gravitational forces by summing each individual particle, GADGET-3 uses a Barnes-Hut oct-tree algorithm (Barnes and Hut, 1986) to approximate the gravitational contribution. In this method, the simulation volume is divided up into cells via an oct-tree, so that only particles from nearby cells need to be treated individually, and distant particles are grouped together into ever larger cells and their contribution to the potential is approximated at the cell centre of mass plus a number of multipole expansions. GADGET, in particular, adopts only the monopole moments due to numerical considerations.

The cell-opening criterion is the following: a node is considered for usage if

$$\frac{GM}{r^2}\left(\frac{l}{r}\right)^2 \leq \alpha_\theta |\mathbf{a}|, \tag{2.27}$$

where M, l and r are the node's mass, extension and distance to the particle, respectively. Additionally, $|\mathbf{a}|$ is the particle's net acceleration in the previous time-step, and α_θ is a tolerance parameter. Internally, in GADGET-3 this parameter is called `ErrTolForceAcc`. The tolerance basically determines the accuracy of the simulation; larger values increase the speed, but decreasing the accuracy of the result. If `ErrTolForceAcc` is set to zero, then all particles are treated individually and the algorithm is equivalent to a direct-summation algorithm. Unless stated otherwise, for these simulations I choose `ErrTolForceAcc`=0.005.

2.5.2 Time integration

In order to preserve the Hamiltonian structure of the system, the time integration of the particle's equation of motions is done using a symplectic integrator. Symplectic integrators are designed for the numerical solution of Hamilton's equations, which read

$$\dot{\mathbf{p}} = -\frac{\partial H}{\partial \mathbf{q}} \tag{2.28}$$

$$\dot{\mathbf{q}} = \frac{\partial H}{\partial \mathbf{p}}. \tag{2.29}$$

where $\mathbf{q}$ denotes the position coordinates, $\mathbf{p}$ the momentum coordinates and H is the Hamiltonian. Symplectic integrators are, by definition, canonical transformations. With this formalism, the evolution of the system can be viewed as a continuous canonical transformation generated by the Hamiltonian. Most of the usual numerical methods, like the primitive Euler scheme and the classical Runge-Kutta scheme, are not symplectic integrators. Consequently, GADGET-3 implements the leapfrog scheme. In particular, for individual variable time-steps (see below) it uses the "kick-drift-kick" (KDK) integrator. This scheme is symplectic because it corresponds to a succession of phase-space transformations. The other advantage of the leapfrog is its time-reversibility. The integrator is based on the operator "drift", given by

$$D_t(\Delta t): \begin{cases} \mathbf{p}_i & \rightarrow \ \mathbf{p}_i \\ \\ \mathbf{x}_i & \rightarrow \ \mathbf{x}_i + \dfrac{\mathbf{p}_i}{m_i}\displaystyle\int_t^{t+\Delta t} \frac{\mathrm{d}t}{a^2} \end{cases}, \tag{2.30}$$

and "kick" given by

$$K_t(\Delta t): \begin{cases} \mathbf{p}_i & \rightarrow \ \mathbf{p}_i + \mathbf{f}_i \displaystyle\int_t^{t+\Delta t} \frac{\mathrm{d}t}{a} \\ \\ \mathbf{x}_i & \rightarrow \ \mathbf{x}_i \end{cases}, \tag{2.31}$$

where $\mathbf{f}_i$ is the force on particle i. Using these operators, the time evolution operator can be approximate as

$$\tilde{U} = K\left(\frac{\Delta t}{2}\right) D(\Delta t) K\left(\frac{\Delta t}{2}\right). \tag{2.32}$$

In practice, what this integrator does is to update the positions and velocities of the particles at interleaved time points in such a way that they "leapfrog" over each other. The separation of the force calculation onto the beginning and end of a step means that if time resolution is increased by a factor of two, then only one extra force calculation is required.

Individual and adaptive time-steps

For the majority of astrophysical systems there is a very large dynamical range in the domain of a hydrodynamical simulation. For example, in the models presented here, the density contrast between the gas close to the black holes and the regions far from the binary is typically 5 orders of magnitude, if not more. Naturally, the time-steps required to integrate the particles in the high-density regions are smaller compared to the low-density counter-parts. Consequently, evolving all particles with the smallest time-step implies a substantial waste of computational time. For this reason, GADGET-3 has an integration scheme with individual time-stepping. The main idea is to compute the forces only for a fraction of the total particles in a given iteration; particles with smaller time-steps are evolved more frequently than the ones with larger time-steps.

The time-step criterion for colissionless particles is

$$\Delta t_i^{(\mathrm{grav})} = \min\left[\Delta t_{\max}, \left(\frac{2\eta\epsilon_i}{|\mathbf{a}_i|}\right)\right], \tag{2.33}$$

where η is an accuracy parameter set as $\eta = 0.05$ over all simulations, ϵ is the gravitational softening and $\mathbf{a}$ the acceleration of the particle. The value of ϵ depends on the particle type: for gas particles it is forced to be equal to the smoothing length in order to avoid spurious fragmentation, while for the black holes (see below) it is fixed to $\epsilon_{\mathrm{BH}} = 10^{-2}$, in code units. It is worth mentioning that for the simulations presented in Chapter 3 the black hole time-steps are computed using equation (2.33), while for the models where I study the binary orbital evolution (Chapters 4 and 5) this value is fixed to maintain the time symmetry of the orbit integration.

For SPH particles, there is an additional criterion – a Courant-like hydrodynamical time-step related to the signal velocity between particles ($v_{\mathrm{sig}} = c_i + c_j - 3w_{ij}$)

$$\Delta t_i^{(\mathrm{hyd})} = C_{\mathrm{courant}} \frac{h_i}{\max_j (c_i + c_j - 3w_{ij})}, \tag{2.34}$$

The maximum value is determined among the neighbouring particles j of particle i. The final time-step for a gas particle would be the minimum between equations (2.33) and (2.34).

For the simulations shown in Chapter 3, I set $C_{\mathrm{courant}} = 0.1$, while for Chapters 4 and 5 this value has been decreased to $C_{\mathrm{courant}} = 0.03$ in order to achieve a higher numerical accuracy, necessary to resolve the small changes expected in the binary orbit.

2.5.3 Code modifications

In addition to the basic physics described above, two non-standard modifications to the code have been made in order to model the interaction between the binaries and the turbulent infalling clouds. In the following subsections I will describe them.

Modelling accreting black holes

To model the presence of a binary of SMBHs I use so-called 'sink' particles. This type of particle was first introduced to SPH simulations by Bate, Bonnell, and Price (1995). Sink particles are often used to represent 'heavy' objects in hydrodynamical simulations (e.g., stars, planets, black holes). Their main feature is that they are allowed to accrete SPH particles that satisfy some conditions. Other than that, sink particles interact with other particles (including sinks) only through gravity. It is worth mentioning that, even though I am modelling SMBHs, the gravity throughout these simulations is purely Newtonian. This approximation is justified because relativistic corrections are negligible at the relevant scales for sub-parsec binaries.

The accretion recipe included in the standard version of GADGET-3 uses the Bondi model to estimate the amount of mass that should be added to each SMBH and then determines, probabilistically, the corresponding accreted particles (Springel, Di Matteo, and Hernquist, 2005). This prescription for the black hole growth is usually applied in cosmological simulations (e.g. Planelles et al., 2014) because the scales where the SMBHs are accreting are well below the resolution limit. In contrast, in all the numerical models presented in the thesis the Bondi–Hoyle–Littleton radius is resolved, thus I shall use a more deterministic recipe for accretion.

In these simulations each black hole is represented by a "deterministic" sink particle. That means, it accretes all SPH particles satisfying some given conditions within a certain radius (Cuadra et al., 2006). In these models the SMBHs have a fixed accretion radius of $r_{\rm sink} = 0.1a_0$, where a_0 is the initial separation of the binary (see §3.1.2). Each particle crossing $r_{\rm sink}$ is accreted if its kinetic energy is less than a fraction α of its potential energy[2] (Dotti et al., 2009):

$$E_{\rm kin} < \alpha |E_{\rm pot}|. \tag{2.35}$$

Since the accretion radius is very large compared to the Schwarzschild radius[3] ($R_{\rm sch}$), this condition is necessary to avoid non-bound particles being added to the SMBHs. I adopt $\alpha = 1$ throughout all the simulations presented, meaning that all bound particles within the accretion radius are added to the corresponding SMBH. I have tested $\alpha = 0.5$ and also $r_{\rm sink} = 0.05a_0$, but the results were virtually unchanged, thus I kept the original values to save computational time.

When a gas particle is accreted, its mass and linear momentum are directly added to the sink particle, and it is no longer considered in the calculation. The properties of the accreted particles, such as time, ID, mass, position and velocity, are stored once they are added to the SMBH (Dotti et al., 2010). This allows to explore the fate of the unresolved material inside the sink radius, such as unresolved mini-discs (Chapter 3, § 3.4), or to know the angular momentum of the gas particle at the moment of accretion (Chapter 4, § 4.3).

[2] Both energies are computed in the reference frame of each SMBH.

[3] For a $10^6 M_\odot$ binary separated 0.1 pc, the sink radius would be $\sim 10^5 R_{\rm sch}$.

Gas thermodynamics

As I do not implement radiative cooling explicitly for these models, I use a barotropic equation of state, i.e. pressure as a function of density $P = P(\rho)$. The functional form of the pressure is chosen to mimic the thermodynamics – in particular the temperature dependance with density – of star-forming gas. At low densities the cloud is initially optically thin to the thermal emission from dust grains, and the compressional heating rate by the collapse is much smaller than the cooling rate by the thermal radiation. The situation reverses at high densities, when the compressional heating overwhelms the radiative cooling rate and the gas is heated as it collapses (Masunaga, Miyama, and Inutsuka, 1998; Masunaga and Inutsuka, 2000).

Following Bonnell (1994), the effective equation of state has the same form as equation (2.19), but with a polytropic index γ that depends on the density as follows:

$$\begin{aligned} \gamma &= 1.0 \qquad \text{for} \qquad \rho \leq \rho_c, \\ \gamma &= 1.4 \qquad \text{for} \qquad \rho > \rho_c, \end{aligned} \tag{2.36}$$

with the threshold density chosen to be $\rho_c = 1.096$, in code units. When scaling the simulations to physical units (see § 3.6.1), this critical density assumes values in the range $10^{-10} - 10^{-14}$ g cm^{-3}, which are typically found during the first collapse of star-forming regions (see e.g. Masunaga, Miyama, and Inutsuka, 1998). Note that the introduction of this two-regime equation of state breaks the scale-free nature of the simulations. In Section 3.6.1 I discuss the interpretation of scaling this number to different physical units. The index $\gamma = 7/5$ corresponds to an adiabatic regime for diatomic gas and it is the value found by Masunaga and Inutsuka (2000) that represents the thermal evolution of a collapsing molecular cloud in the density regime of interest.

A consequence of using this equation of state is that it stops the collapse of the densest gas, avoiding excessively small time-steps that can stall the simulations. This type of equation of state is frequently used in hydrodynamical simulations of the evolution of turbulent clouds (e.g. Bate, Bonnell, and Price, 1995). In the case of these models, this simple treatment of the thermodynamics allows to capture the global behaviour of the gas during the interaction with the binary without an explicit implementation of cooling and/or radiative transfer. As the overall gas dynamics during the early phases of the interaction is dominated by the gravitational potential of the binary, the results presented here will depend only weakly on the adopted thermodynamics. The long-term evolution of the gas will be likely dependent on the thermodynamics, e.g. the cooling rate will determine whether the gas fragments or not.

Recall that the isothermal regime enforces a constant entropic function A. From equation (2.20), this implies that any heat generated by shocks (through artificial viscosity) will be immediately radiated away.

Chapter 3

Single cloud infall: formation of discs and accretion

As largely discussed in Chapter 1, gas accretion in the form of cloud clumps are a plausible source of gas for sub-parsec SMBHBs. Exploring the hypothesis that infalling clouds are common in post-merger galactic nuclei, I numerically model the evolution of a turbulent cloud in near-radial infall onto equal-mass and circular binaries, using the modified version of the SPH code GADGET-3 previously introduced.

In this chapter, I present a total of 12 simulations that explore different possible pericentre distances and relative inclinations for the incoming cloud to study the formation of gaseous structures depending on those parameters. I am also interested in the dynamics of the formed discs, as well as the variability of the feeding rate onto the SMBHs in the different configurations. The main focus is to present different phenomenologies that can potentially have distinctive electromagnetic signatures, which are very relevant for the future identification and characterisation of SMBHBs.

3.1 Initial conditions

3.1.1 Turbulent cloud

The cloud is set to have initially constant density, and a turbulent velocity field imposed upon it using a method similar to Bonnell and Rice (2008). The turbulent velocity field provides support to the cloud against its self-gravity and it generates local structures, some of which can collapse to form stars.

The velocities are drawn from a Gaussian random distribution with power spectrum

$$P_v(k) \equiv \langle |\mathbf{v}_k|^2 \rangle \propto k^{-n}, \tag{3.1}$$

where k is the wave number of the velocity perturbation. Throughout this thesis, I use a power index of $n = 4$ for the perturbation spectrum, which yields a velocity dispersion averaged over a volume of size R of

$$\sigma_v \propto R^{1/2}, \tag{3.2}$$

to match the observed velocity dispersion of molecular clouds (Larson, 1981).

To set the internal velocity field the cloud is treated as incompressible ($\boldsymbol{\nabla} \cdot \mathbf{v} = 0$), which implies that the velocity field can be represented with a "vector potential" $\boldsymbol{A}$. This vector follows a Gaussian distribution related to that of the desired velocity, namely,

$$\boldsymbol{A}_k(k_x, k_y, k_z) = k^{\frac{-n-2}{2}} \left(C_{k_x} e^{i\phi_{k_x}}, C_{k_y} e^{i\phi_{k_y}}, C_{k_z} e^{i\phi_{k_z}} \right) \tag{3.3}$$

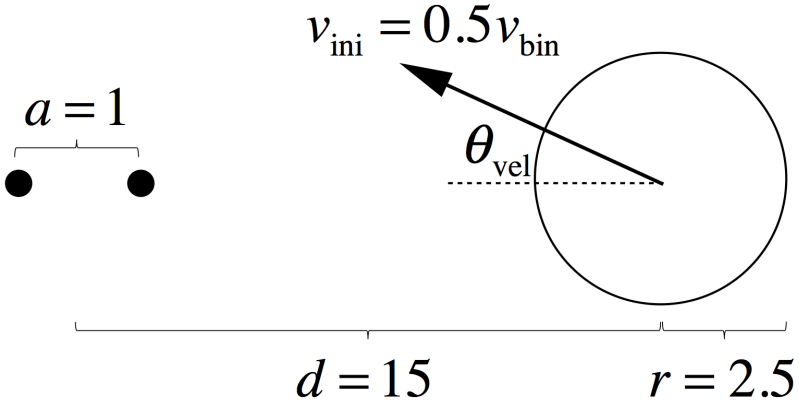

FIGURE 3.1: Initial setup of the simulations. The circle on the right represents the cloud, while the small black, solid circles are the SMBHs. In this set of 12 simulations I sample different inclinations of the cloud initial velocity (i.e. different $\theta_{\rm vel}$) and orientations of the binary orbit.

where the amplitude C_k is given by a Rayleigh distribution, while the phase angle ϕ will be uniformly distributed between 0 and 2π.

I sample the components of $\mathbf{A}$ in the Fourier space ($\mathbf{A}_k$) using an equispaced lattice with 256^3 coordinates (k_x, k_y, k_z) in the range

$$-k_{\rm max} \leq k_i \leq k_{\rm max}, \tag{3.4}$$

where

$$k = \sqrt{k_x^2 + k_y^2 + k_z^2} \tag{3.5}$$

and

$$k_{\rm max} = \frac{2\pi}{d_{\rm min}}. \tag{3.6}$$

The minimum inter-particle distance in these simulations is $d_{\rm min} = 3 \times 10^{-2}$ in code units (see below).

To assign a velocity vector to each particle, I inverse Fourier transform $\mathbf{A}$ and then interpolate the obtained values between grid points. Finally, the velocity field is normalised such that the kinetic energy is equal to the absolute value of the potential energy, resulting in a cloud that is marginally unbound.

3.1.2 Binary-cloud setup

The physical setup of the simulations is shown in Figure 3.1. I place the cloud at a distance of 15 from the centre of mass of the binary, with an initial velocity $\mathbf{v}_{\rm ini}$ such that it has an eccentric, bound orbit. The modulus of the initial velocity vector is constant in all simulations ($v_{\rm ini} = 0.5\, v_{\rm bin}$, where $v_{\rm bin} = 0.5\sqrt{GM/a}$ is the tangential velocity of each SMBH), but I change its direction, reflected in the angle $\theta_{\rm vel}$. I model clouds with three different impact parameters; I choose $\theta_{\rm vel} = 0.197$, 0.298 and 0.403 radians, so that the pericentre distances are 0.7, 1.5 and $3\, R_{\rm bin}$, respectively, where $R_{\rm bin}$ is the binary radius (i.e. half of the binary separation, $a/2 = 0.5$).

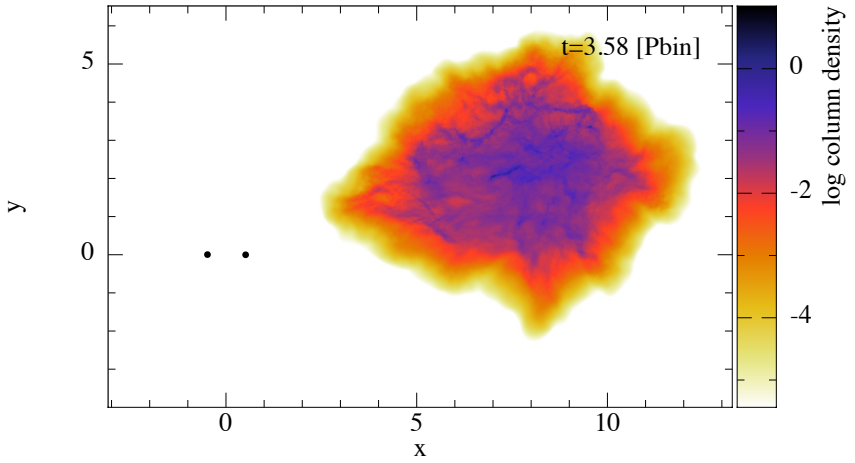

FIGURE 3.2: Column density map of an early snapshot after the initial conditions of one of the simulations. At this stage the cloud looks roughly the same for all orbital configurations, as its evolution is dominated by the initial turbulent velocity field. The SMBHs are represented with two black circles on the left.

Finally, since turbulence and relaxation might cause significant randomisation of the angular momenta of the gas clouds on parsec scales, I model clouds approaching with different relative orientations with respect to the binary orbit:

- "Aligned": the cloud starts in the plane of the SMBHB, with $\mathbf{v}_{\rm ini}$ lying on the same plane such that the cloud and the binary are co-rotating.
- "Counter-aligned": same as aligned, but counter-rotating.
- "Perpendicular edge-on": the cloud is initially in the same plane as the SMBHB, but the tangential component of $\mathbf{v}_{\rm ini}$ $(v_{\rm ini} \sin\theta_{\rm vel})$ is perpendicular to that plane.
- "Perpendicular face-on": the cloud starts in the plane perpendicular to that of the SMBHB, but the tangential component of $\mathbf{v}_{\rm ini}$ is parallel to that plane.

3.2 Formation of discs

In Fig. 3.2 I show an early snapshot of one of my simulations as a column density map. Due to the large initial distance between the cloud and the SMBHB, the evolution of the gas is initially dominated by the turbulent velocity field, which produces filaments in the cloud. In this snapshot it can already be noticed how the gas is stretched by the gravitational pull of the binary. At this stage, the gas evolves almost independently of the particular orbital configuration of the system, because the effects that the SMBHB quadrupole potential can have on the hydrodynamics of the cloud are negligible, and the differences between impact parameters are small.

The study of the secular evolution of the systems, after the gas dynamics reaches a quasi-steady state, requires a considerable computing time that is not affordable with the standard configuration. I hence stop the simulations either once the transient effects of the cloud infall have stopped, or when the simulation stalls due to clump formation. I do however explore long-term effects with lower-resolution simulations in Section 3.5.

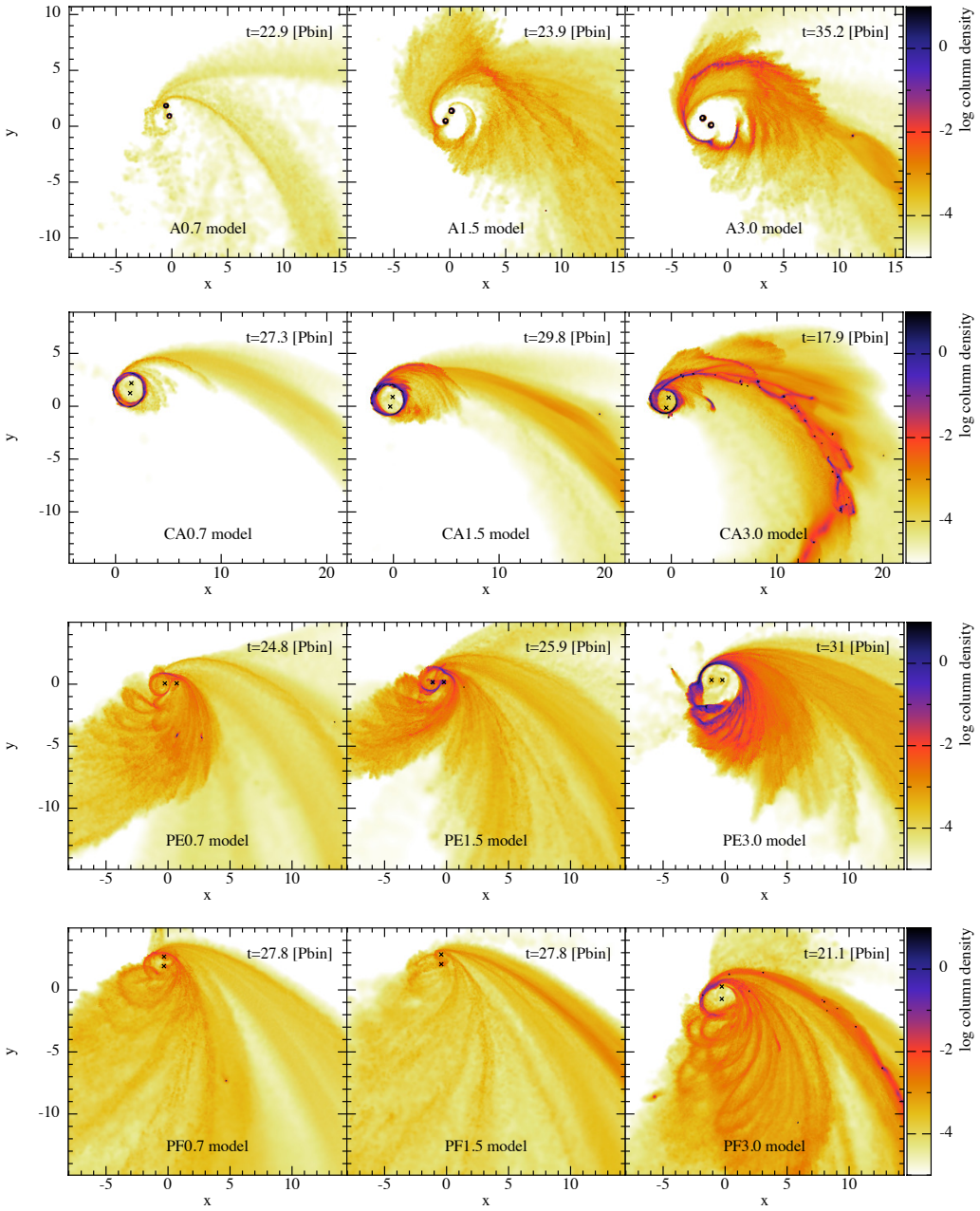

FIGURE 3.3: Column density maps of each simulation's final state. The different rows are the 4 inclinations modelled, while increasing the impact parameter from left to right, as indicated by the model name. The position of the SMBHs is indicated by the black crosses. *Top row – aligned (A) simulations:* The binary moves on the x-y plane, counter-clockwise. *Upper middle row – counter-aligned (CA) simulations:* The binary moves on the x-y plane, clockwise. *Lower middle row – perpendicular edge-on (PE) simulations:* The binary moves on the x-z plane. *Bottom row – perpendicular face-on (PF) simulations:* The binary moves on the y-z plane.

I show the final state of my aligned simulations (models A) in the top row of Fig. 3.3. The first interaction of the gas with the binary is characterised by an efficient slingshot which pushes the remaining gas away from the system, shaping a tail. For the smallest impact parameter (top row, left panel of Fig. 3.3), the strong interaction only allows the formation of the so-called "mini-discs" around each SMBH, while increasing the impact parameter allows more material to avoid the slingshot and settle in bound orbits around the binary, forming a circumbinary disc. The common feature of every impact parameter is the formation of mini-discs, appearing in the figure as black rings around either SMBH because of their high column density. The discs tend to be slightly misaligned with respect to the binary orbit. The analysis of the dynamics of these mini-discs is shown in Section 3.4. *Only with this orientation is the formation of extended, prominent and persistent mini-discs observed.* For the other SMBHB-cloud orientations, the material captured by individual SMBHs has little angular momentum, thus falling directly within $r_{\rm sink}$. Nevertheless, higher resolution tests sometimes show the formation of *small and intermittent* mini-discs, which indicates that mini-discs might form on smaller scales, but cannot be resolved with the standard resolution. I explore the possibility of unresolved mini-discs inside the sink radius in Section 3.4.

The final state of the counter-aligned simulations (models CA) is shown in the upper middle row of Fig. 3.3. The interaction is very different because the typical gas velocity has the opposite direction relative to the orbital motion of the binary, cancelling most of the gas initial angular momentum. This enhances the accretion onto the SMBHB, as discussed in Section 3.3. The gas that remains bound after the interaction forms a very eccentric tail. For the three cases the formation of a nearly circular, very narrow, counter-rotating circumbinary ring is observed, arising as the material from the tail reaches the binary radius. The inner edge of these rings has a radius $\approx a$ from the center-of-mass (CoM) of the binary, which is expected due to the absence of resonances in a counter-rotating case (e.g. Nixon et al., 2011). The main qualitative difference observed in these three counter-aligned cases is the amount of gas clumps formed, as larger impact parameters result in more clumps. Most of these clumps form due to the compression of gas during the pericentre passage that allows them to become self-gravitating, and eventually to form stars. I discuss the observational implications of star formation in Section 3.6.

I show the final state of my two perpendicular simulations in the lower rows of Figures 3.3 (model PE, perpendicular edge-on and models PF, perpendicular face-on). As the typical gas velocity is perpendicular to that of the black holes, the slingshot is not very efficient, meaning that most of the gas is not pushed away from the binary. As the impact parameter increases, more material is allowed to settle on stable orbits. This gas forms a circumbinary disc, although completely misaligned with respect to the binary, keeping its initial angular momentum direction. In these configurations there are also regions of over-density which might lead to stellar formation, although they are located outside the region shown in the figures.

In Table 3.1, I compile different relevant values measured for the discs formed in the simulations. As noticed above, only the aligned cases show the formation of extended mini-discs, detectable at the resolution of the sink radius. These discs are very prominent and stable, and hence easy to identify. All their quantities presented have been computed using the median values over the last binary orbit. It is striking that the disc masses are very similar for different impact parameters, which means that this quantity is -at least in this respect- independent of the amount of non-accreted gas. Note that all these mini-discs extend from the

accretion radius of the SMBH to around the radius of the Hill sphere[1], as expected.

The circumbinary discs are more difficult to analyse. It is not possible to determine at the time I stop the simulations which fraction of the gas is going to form a stable disc. Hence, I first simply visually establish whether there is gas orbiting the binary in closed orbits – this criterion is stated in Table 3.1. Additionally, to estimate the possible disc properties, I identify the gas particles that could become part of a circumbinary disc. These are going to be the particles that are bound to the binary, and have orbits calculated around the CoM with pericentre distances b larger than a threshold value defined to be $r_{\rm min} = 2a$ for the aligned cases and $r_{\rm min} = a$ for the rest. Gas particles with a pericentre distance smaller than this radius will either be re-ejected in a slingshot process that prevents the gas to complete an orbit around the binary (see e.g. top row, left panel of Fig. 3.3), or accreted, or will become part of one of the minidiscs, if present. For all gas particles fulfilling the $b > r_{\rm min}$ criterion, I measure as before the total mass and median eccentricity from the last snapshot in each simulation. The amount of gas available to form a circumbinary disc increases with the impact parameter, simply because gas with larger angular momentum avoids being accreted. The median eccentricity of the gas is high for most cases due to the initial orbit of the cloud: after the first passage most of the gas forms a very eccentric tail. The exception is case CA0.7, here, due to the small pericentre distance, most of the gas is accreted, leading to a very light tail with respect to the circumbinary ring. The other cases have a more massive tail, which makes the eccentricity distribution skewed towards high values.

In conclusion, the interaction of individual clouds with a binary results in circumbinary discs that are initially very eccentric ($e \gtrsim 0.8$, note that this estimate includes bound material within the highly eccentric tails, the long-term evolution of eccentricity will be discussed in Section 3.5). Moreover, for my choice of parameters, the disc masses are at most roughly half of the initial cloud mass, and in most cases much less than that, only a few percent. This does not only make them hard to detect directly, but also implies a small effect on the secular evolution of the binary. This conclusion is likely to change, however, by considering the cumulative effect of many cloud infall events, or the effect of individual massive clouds.

[1] $r_{\rm H} \approx 0.3a$ for a circular, equally-massive binary

TABLE 3.1: Properties of the discs formed in the simulations. In the model names the letter indicates the orbit orientation (A: aligned, CA: counter-aligned, PE: perpendicular edge-on, PF: perpendicular face-on) and the number the pericentre distance in units of binary radius. $t_{\rm fin}$ is the time at which I stop each simulation. M_i and $r_{i,\rm out}$ $(i = 1, 2)$ are the mini-disc masses and outer radii, respectively. Available M corresponds to the mass available to form a circumbinary disc, while $< e >$ is the median eccentricity of that gas.

Model	$t_{\rm fin}$ ($P_{\rm bin}$)	Resolved mini-discs?	M_1 ($M_{\rm bin}$)	M_2 ($M_{\rm bin}$)	$r_{1,\rm out}$ (a)	$r_{2,\rm out}$ (a)	Noticeable Circumbinary?	Available M ($M_{\rm bin}$)	$< e >$
A0.7	22.9	YES	2.6×10^{-4}	1.4×10^{-4}	0.34	0.44	NO	2.9×10^{-6}	0.89
A1.5	23.9	YES	3.8×10^{-4}	4.3×10^{-4}	0.32	0.31	YES	1.1×10^{-4}	0.88
A3.0	35.2	YES	2.8×10^{-4}	4×10^{-4}	0.28	0.29	YES	1.3×10^{-3}	0.89
CA0.7	27.3	NO	-	-	-	-	YES	5.9×10^{-4}	0.16
CA1.5	29.8	NO	-	-	-	-	YES	2.6×10^{-3}	0.81
CA3.0	17.9	NO	-	-	-	-	YES	5.5×10^{-3}	0.83
PE0.7	24.8	NO	-	-	-	-	NO	1.5×10^{-4}	0.89
PE1.5	25.9	NO	-	-	-	-	NO	1.9×10^{-3}	0.91
PE3.0	31.2	NO	-	-	-	-	YES	6.7×10^{-3}	0.75
PF0.7	27.8	NO	-	-	-	-	NO	8.6×10^{-5}	0.91
PF1.5	27.8	NO	-	-	-	-	NO	8.8×10^{-4}	0.97
PF3.0	21.1	NO	-	-	-	-	YES	5.6×10^{-3}	0.91

3.3 Accretion rate and total accreted mass

In Fig. 3.4 I show the accretion rate and cumulative accreted mass for every inclination and impact parameter. Note that throughout this section the results are presented in code units, thus the results can be re-scaled to a range of binary masses and periods (for physical rescaling of the results see Section 3.6).

It is important to emphasise that the accretion radius set for each SMBH is very large compared to the Schwarzschild radius, so the computed accretion rate does not correspond to the actual accretion onto the SMBHs. The gas within the accretion radius will have non-zero angular momentum, thus should settle on an accretion disc and evolve on a viscous timescale ($t_{\rm visc}$), which is typically longer than its dynamical timescale ($t_{\rm dyn}$) in the SMBH gravitational potencial. In consequence, the accretion rates correspond to the rate at which the gas is added to the BH-accretion disc systems, which are unresolved in my simulations. For an α-disc (Shakura and Sunyaev, 1973), these timescales are related as following:

$$t_{\rm visc} \sim \frac{1}{\alpha}\left(\frac{H}{R}\right)^{-2} t_{\rm dyn}, \tag{3.7}$$

where α is a dimensionless number quantifying the strength of the viscosity (with typical values of $\sim 0.01 - 0.1$) and H/R is the disc aspect ratio. On the other hand, the dynamical timescale (at the sink radius) can be related with the orbital period of the binary as follows:

$$\frac{t_{\rm dyn}}{P_{\rm bin}} \sim \frac{1}{2\pi}\left(\frac{r_{\rm sink}}{a}\right)^{3/2}\left(\frac{M}{M_1}\right)^{1/2} \approx 5\times10^{-3}, \tag{3.8}$$

where $r_{\rm sink} = 0.1a$ is the accretion radius, M is the binary mass and $M_1 = 0.5M$ is the mass of one SMBH.

As a rough estimate, I would expect the actual accretion rate onto each SMBH be related with the binary orbital period if the latter is longer than the viscous timescale. In other words, when

$$\alpha\left(\frac{H}{R}\right)^{2} \gtrsim 5\times10^{-3}, \tag{3.9}$$

which implies that there are combinations of parameters (e.g., $\alpha \sim 0.1$ and $H/R \sim 0.2$) for the unresolved accretion discs where the variability presented below would indeed affect directly the actual accretion onto the SMBHs (Sesana et al., 2012). For systems where the viscous time is longer than the binary orbital period, the streaming periodicity will not be directly reflected into a variable accretion onto each SMBH, and a pair of persistent (unresolved) mini-discs will form. However, even in these cases I could expect to find observational signatures of this variability (§ 3.6).

Another caveat of my model is that I do not include any type of feedback from the SMBHs; radiation pressure could reduce the amount of gas that is accreted. Nevertheless, the amount of gas that actually reaches the SMBHs will likely be a monotonic function of the value that crosses the sink radius.

In summary, the behaviour of the accretion rate shown in this section can still be useful to characterise the accretion onto the SMBHs and the mini-discs emission.

As expected, the accretion rate is very high at the beginning of the interaction with the cloud. Most of the cloud is engulfed by the binary during the first few orbits ($\sim 4-7$), as can be observed in the cumulative mass of each figure. This stage

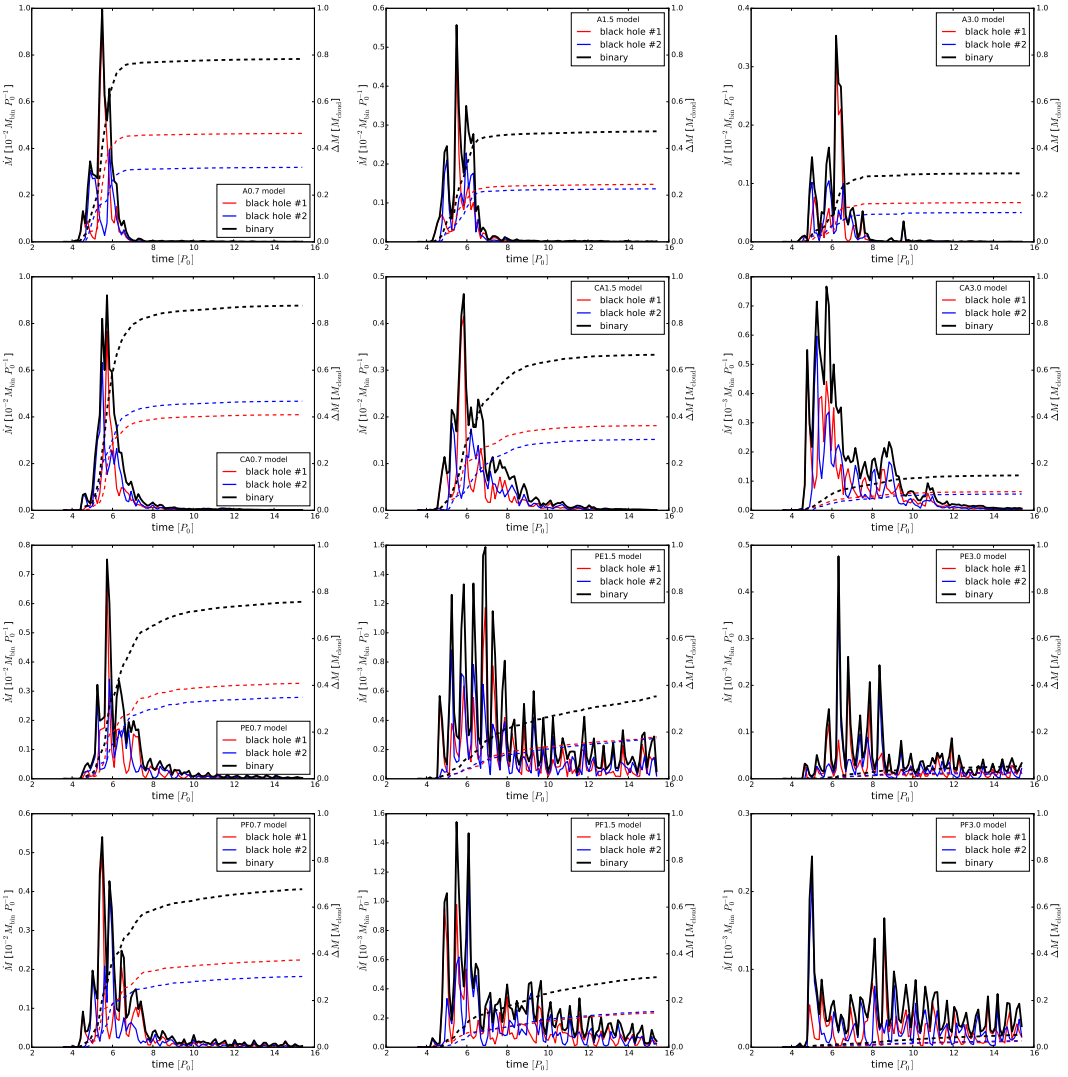

FIGURE 3.4: Evolution of the accretion rate (solid, left axes) and cumulative accreted mass (dashed, right axes) onto the binary (black) and each black hole (blue and red), for all simulations. From left to right: pericentre distances of 0.7, 1.5 and $3R_{\rm bin}$. From top to bottom: aligned, counter-aligned, perpendicular edge-on and perpendicular face-on orbits. Notice that the range of the left y-axes is not the same for all plots. On each curve there is a periodic behaviour that is directly related with the binary period, and in most cases the accretion onto both SMBHs are in counter-phase with each other.

corresponds to the first passage of the cloud. After that interaction the accretion drops sharply, by 2 or 3 orders of magnitude in some cases.

For most orbital configurations there is a clear periodicity of the accretion rates. Each black hole has an accretion periodicity which matches the binary orbital period, but in phase opposition with each other, so that the total binary accretion rate has a period of half an orbit. This feature is associated with the stream of gas that remains bound to the binary and feeds each black hole alternatively when they cross the stream. Variability related to the binary orbital period is the type of behaviour that is expected will help to identify and characterise these systems.

The accretion in the cases of perpendicular orbits (edge and face-on, two lower rows of Fig. 3.4) tends to be more extended than the parallel ones (two upper rows), in the sense that there are still significant peaks after the first passage of the cloud. This is because, as explained in the previous section, the slingshot is less efficient when the encounters have perpendicular relative velocities, allowing more material to remain around the binary in close orbits.

For all the orbital configurations modelled, two trends with increasing impact parameter are apparent: (i) the accretion rates and the total accreted mass decrease, and (ii) the relative amplitude of the accretion rate peaks during the cloud first passage decreases compared to the later stages.

The compilation of the total mass accreted by the binary at the end of each simulation is shown in Fig. 3.5. Here it can be seen how the accretion is dramatically reduced when increasing the impact parameter of the cloud. For instance, in the PE3.0 model the total accretion is around 5% of the cloud mass, in contrast with the $\approx 70\%$ on the smaller pericentre distance (PE0.7). This is very interesting as it shows the transition between a "prompt accretion" regime, and one characterised by the formation of circumbinary discs for the aligned and perpendicular edge-on orbits (see Section 3.5).

3.4 Misaligned mini-discs

As mentioned in Section 3.2, the only configurations that show the formation of extended and stable mini-discs, limited by the Hill radius, are the aligned models, which is the first case I study below. However, I also measure the direction of the gas around the SMBHs for the other inclinations to see if possible unresolved mini-discs have some preferential orientation.

3.4.1 Mini-discs for the aligned configurations

In all my models with aligned orbits there is the formation of prominent and persistent mini-discs around each SMBH (top row of Fig. 3.3). In order to measure the level of alignment with the orbit of the binary I compute the mini-disc direction using the total angular momentum vector of the gas particles within the Hill sphere. I represent this direction with the spherical coordinates (θ, ϕ) in the reference frame of the corresponding SMBH. The time evolution of the mini-disc directions is shown in the Hammer projections of Fig. 3.6.

From these projections it is possible to observe that the mini-discs are well defined and evolve smoothly with time, and also that they are roughly aligned with the binary orbit (and the original cloud orbit), although there is always some level of misalignment. Studying closely the time evolution of the minidisc orientations, I notice the following behaviour: not only the mini-discs precess around the aligned

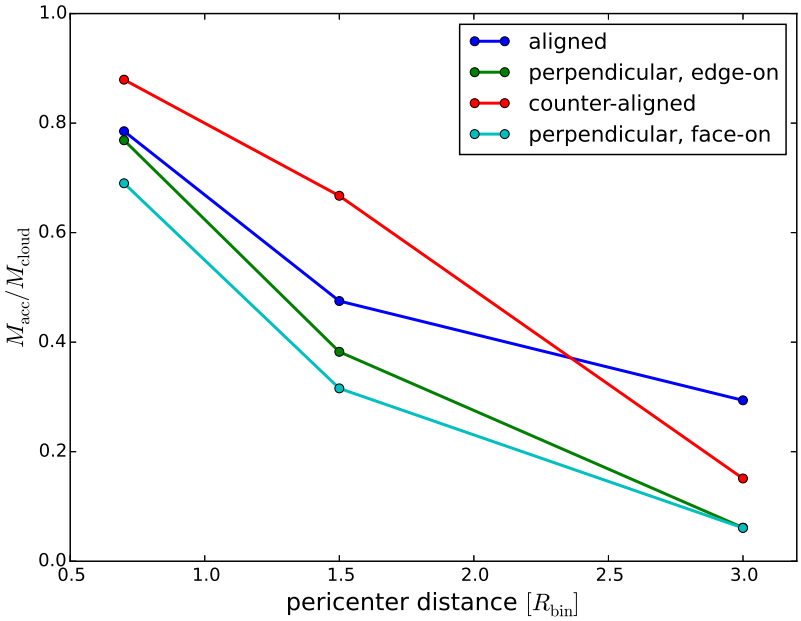

FIGURE 3.5: Fraction of the total cloud mass accreted by the binary as a function of the pericentre distance, for the four different orbital orientations. Notice that the total mass is strongly dependent on the impact parameter of the binary, dropping by one order of magnitud in some cases.

position, but on top of that another low-amplitude, periodic motion is observed that hereafter I refer to as "wobbling". In order to study these motions in more detail, I describe the direction of the mini-discs with other two angles: inclination and position. The first one is the angular difference with respect to the aligned position, while the second is the angle between the projection of the mini-disc on the orbital plane and an arbitrary vector on the same plane.

Since a similar behaviour is observed in all three runs with aligned orbits (see Fig. 3.6), I now concentrate on the analysis of the A3.0 model, which ran the longest and has the best defined direction evolution. Notice that this run also shows a slow but clear alignment of the mini-discs with the binary orientation. However, I do not discuss this in detail as it depends on the numerics (see below). I show the time evolution of the inclination and position angles in Fig. 3.7. The precession is steady (constant slope in absolute value), with a period of around 20 binary orbits. On the other hand, the mini-disc's inclination tends to decrease with time and to wobble with a period almost exactly half of the binary period. As shown below, this behaviour is expected for misaligned discs.

3.4.2 Dynamics of misaligned discs

Based on the study by Bate et al. (2000) I can obtain an analytical understanding of the dynamics of the misaligned mini-discs around each SMBH. I consider a circular binary with components M_1 and M_2, with separation of a. A non-rotating frame with z axis parallel to the rotation axis of the binary, centred on one of the SMBHs is used. The force at a position vector $\boldsymbol{r}$ (with $r \ll a$) caused by the other black hole is given by:

$$\boldsymbol{F}_2 = -\frac{GM_2m_r}{a^3}\boldsymbol{r} + \frac{3GM_2m_r}{a^5}(\boldsymbol{r}\cdot\boldsymbol{a})\boldsymbol{a}, \tag{3.10}$$

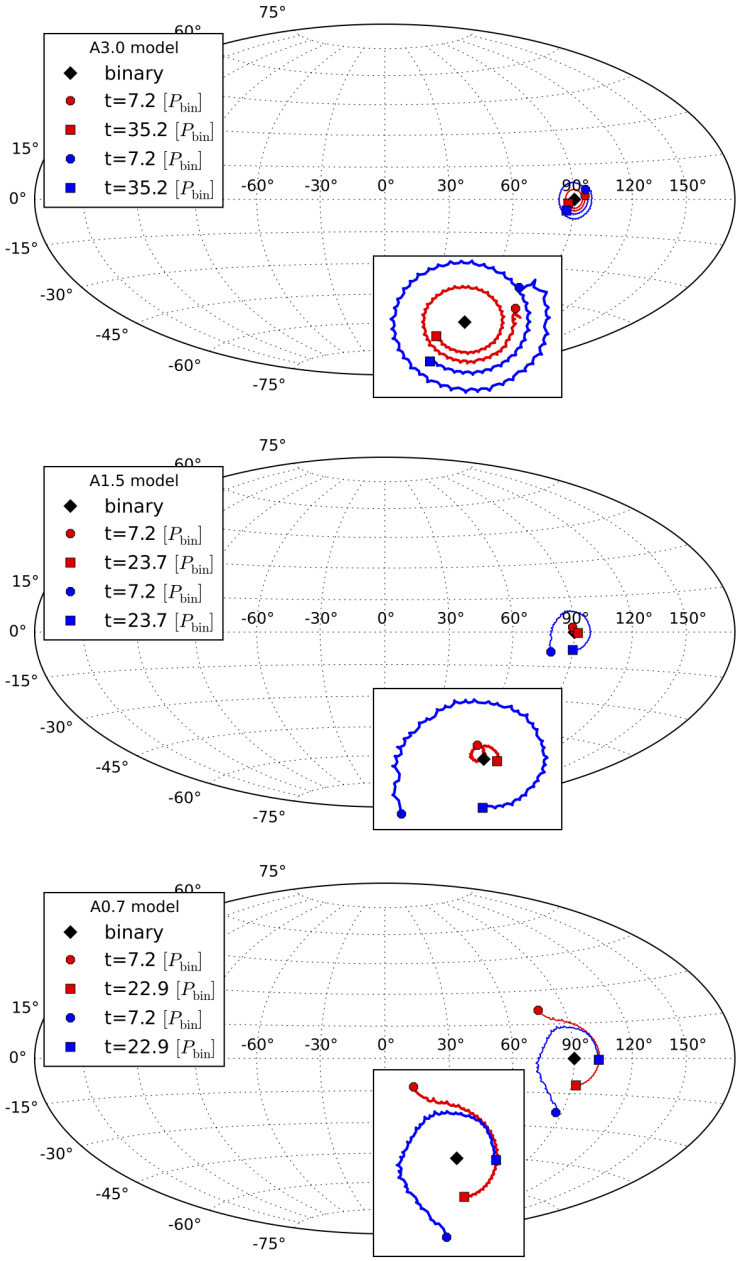

FIGURE 3.6: Time evolution of the directions of both mini-discs shown in Hammer projections for the aligned orbits and the three different impact parameters. Upper left: $0.7R_{\rm bin}$, upper right: $1.5R_{\rm bin}$ and bottom: $3R_{\rm bin}$. The circles and squares correspond to the times when each mini-disc appears and the end of the simulation, respectively; while the black diamonds correspond to the binary orbit orientation. The inset panels show zoom-ins of the projections, in which it is noticeable that the evolution of the mini-discs shows two combined effects: a steady precession around the aligned position and a super-imposed wobbling.

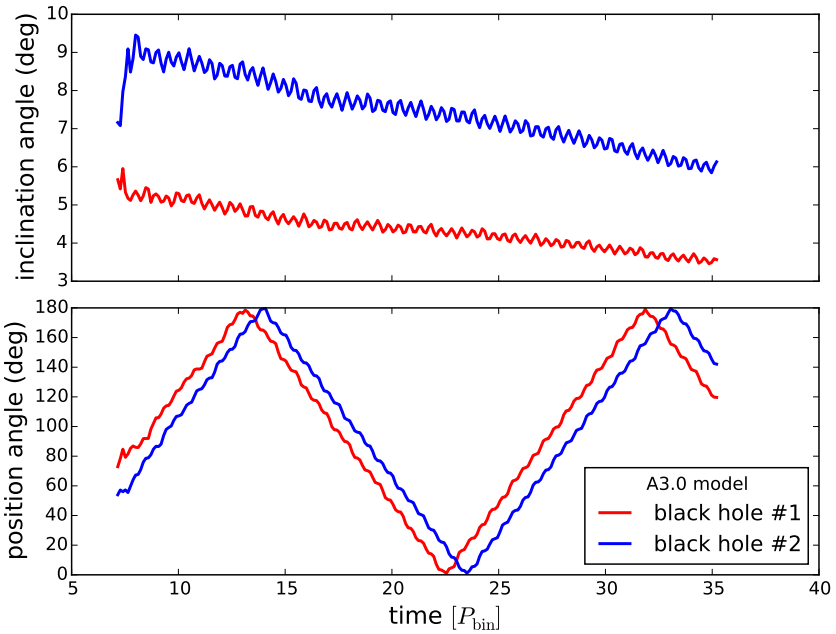

FIGURE 3.7: Upper panel: inclination angle evolution of the mini-discs with respect to the aligned position. Both the slow decline due to dissipation and the wobbling discussed in the main text are clearly visible. Lower panel: position angle evolution, i.e. angle between the projection of the mini-disc direction on the orbital plane and an arbitrary vector on the same plane. This evolution shows how the discs slowly and steadily precesses around the aligned position. The period of this movement is around 20 binary periods.

where $\boldsymbol{a}$ is the position vector of the secondary SMBH and m_r is a test mass.

The right hand side of equation (3.10) can be split into 2 contributions: the isotropic term ($m = 0$) and the quadrupole ($m = 2$), and each of them can be associated with a different effect.

1. The $m = 0$: By considering a ring of gas with mass m_r and radius a_r, the torque produced by this term is:

$$\boldsymbol{T}_0 = -\frac{3}{4}\left(\frac{GM_2 m_\mathrm{r} a_\mathrm{r}^2}{a^3}\right)\sin\delta\cos\delta\hat{\imath}. \tag{3.11}$$

   The angular frequency of a ring of disc material is given by

$$\boldsymbol{\Omega}_\mathrm{d} = -\Omega_\mathrm{d}\sin\delta\hat{\jmath} + \Omega_\mathrm{d}\cos\delta\hat{k}, \tag{3.12}$$

   where Ω_d is a function of the radius of the considered ring, δ is the inclination angle of the ring with respect to the binary plane. Then, as $\boldsymbol{\Omega}_\mathrm{d}\cdot\boldsymbol{T}_0 = 0$, the net effect of this torque is to produce a precession around the z axis. The mean precession rate is

$$\frac{\omega_\mathrm{p}}{\Omega_\mathrm{d}} = \frac{3}{4}q\cos\delta\left(\frac{a_\mathrm{r}}{a}\right)^3, \tag{3.13}$$

   where q is the mass ratio of the binary.

2. The $m = 2$: In this case the torque on the ring is

$$\begin{aligned}\boldsymbol{T}_2 = -\frac{3}{4}\left(\frac{GM_2 m_\mathrm{r} a_\mathrm{r}^2}{a^3}\right)\sin\delta\,[&\cos\delta\cos(2\Omega_\mathrm{b}t)\hat{\imath}\\ &+\cos\delta\sin(2\Omega_\mathrm{b}t)\hat{\jmath} + \sin\delta\sin(2\Omega_\mathrm{b}t)\hat{k}],\end{aligned} \tag{3.14}$$

   where Ω_b is the binary angular frequency. This oscillating torque is also perpendicular to the rotation of the ring ($\boldsymbol{T}_2\cdot\boldsymbol{\Omega}_\mathrm{d} = 0$), and the effect is to produce an oscillation around the steady precession, with a frequency equal to twice the binary frequency, consistent with what I measure for the inclination in Fig. 3.7. The amplitude of the wobble is roughly $\sim\omega_\mathrm{p}/(2\Omega_\mathrm{b})$.

The behaviour of the entire disc will be given by the integral of each ring. Then, the net precession rate is

$$\frac{\omega_\mathrm{p}}{\Omega_\mathrm{d}} = K\cos\delta q\left(\frac{R}{a}\right)^3, \tag{3.15}$$

where

$$K = \frac{3}{4}R^{-3/2}\frac{\int_0^R \Sigma r\,\mathrm{d}r}{\int_0^R \Sigma r^{-3/2}\,\mathrm{d}r}, \tag{3.16}$$

and Σ is the mass surface density of the disc. Some typical values of K are: $K = 15/32 \approx 0.487$ for a constant surface density profile (Larwood et al., 1996); and $K = 3/10$ for $\Sigma\propto r^{-3/2}$ (Hartmann et al., 1998).

Thus typically

$$\frac{\omega_\mathrm{p}}{\Omega_\mathrm{b}} \approx 0.05\left(\frac{K}{0.4}\right)q\sqrt{\frac{2}{1+q}}\left(\frac{R}{0.3a}\right)^{3/2}\cos\delta. \tag{3.17}$$

Evaluating equation (3.17) with the approximate values of my mini-discs I find

$$\frac{P_{\rm p}}{P_{\rm b}} \approx 20, \tag{3.18}$$

and also the amplitude of the wobble in the outer part of the disc, which is the dominant contribution, is

$$A_{\rm wob} \sim \frac{\omega_{\rm p}}{2\Omega_{\rm b}} \approx 0.02 \text{ rad} \approx 1 \text{ deg}. \tag{3.19}$$

Both quantities are actually very close to what is observed in Fig. 3.7.

All these calculations are made assuming that the discs are able to communicate the precession efficiently without breaking, which is clearly the case in my simulations as they move as a whole. However, the ability of the disc to precess rigidly depends strongly on its aspect ratio and viscosity (Papaloizou and Terquem, 1995; Larwood et al., 1996; Lubow and Ogilvie, 2000; Fragner and Nelson, 2010; Doğan et al., 2015), which are not well resolved quantities in my models due to the small number of particles ($\sim$ 1000) that shape the mini-discs and the numerics itself. In addition, the presence of the accretion radius around the sink particles excises the inner portion of the mini-discs, which does not allow to model the precession and wobbling particularly onto those scales.

The numerical models performed by Fragner and Nelson (2010), study the evolution of individual discs that arise in misaligned binary systems, showing precession and wobbling (i.e. periodic perturbation in the inclination angle), similarly as I found in my mini-discs. Their grid-based hydrodynamic code allows them to control better the viscosity's influence in the disc evolution. They show that, for several combinations of aspect ratios and viscosities, the discs will efficiently communicate the differential precession and move as a rigid body. In particular, they find that thin discs ($h \lesssim 0.03$) with high viscosities will achieve a state of rigid precession after developing a twist. More important, when the discs are not disrupted due to the differential precession, the periodic perturbations in the inclination are able to travel all the way to the central parts (cf. their Fig.6), which are not resolved in these models.

In conclusion, even if the global dynamics of the mini-discs cannot be studied robustly due to the relatively low resolution of my models, I expect that the misalignment arising from the infall of extended portions of gas will produce the precession and wobbling observed.

3.4.3 Mini-discs for other inclinations

As explained in Section 3.2, during the whole duration of the simulations with different inclinations (counter-aligned and perpendiculars) I do not observe the formation of persistent mini-discs, probably because I do not have the spatial resolution due to the artificially large accretion radii and the low angular momentum of the captured gas relative to the individual SMBHs. Nevertheless, I can still measure whether the material around each SMBH has some preferential direction. I do so by computing the angular momentum of all accreted gas between outputs, which is an indicator of the direction that the unresolved mini-discs might have, if they exist. I consider the time after the first passage of the cloud (~ 8 orbits) for every snapshot until the simulation ends. I show an example of the projections obtained with the larger impact parameter in Fig. 3.8, where each point represents the direction of the gas in a particular output.

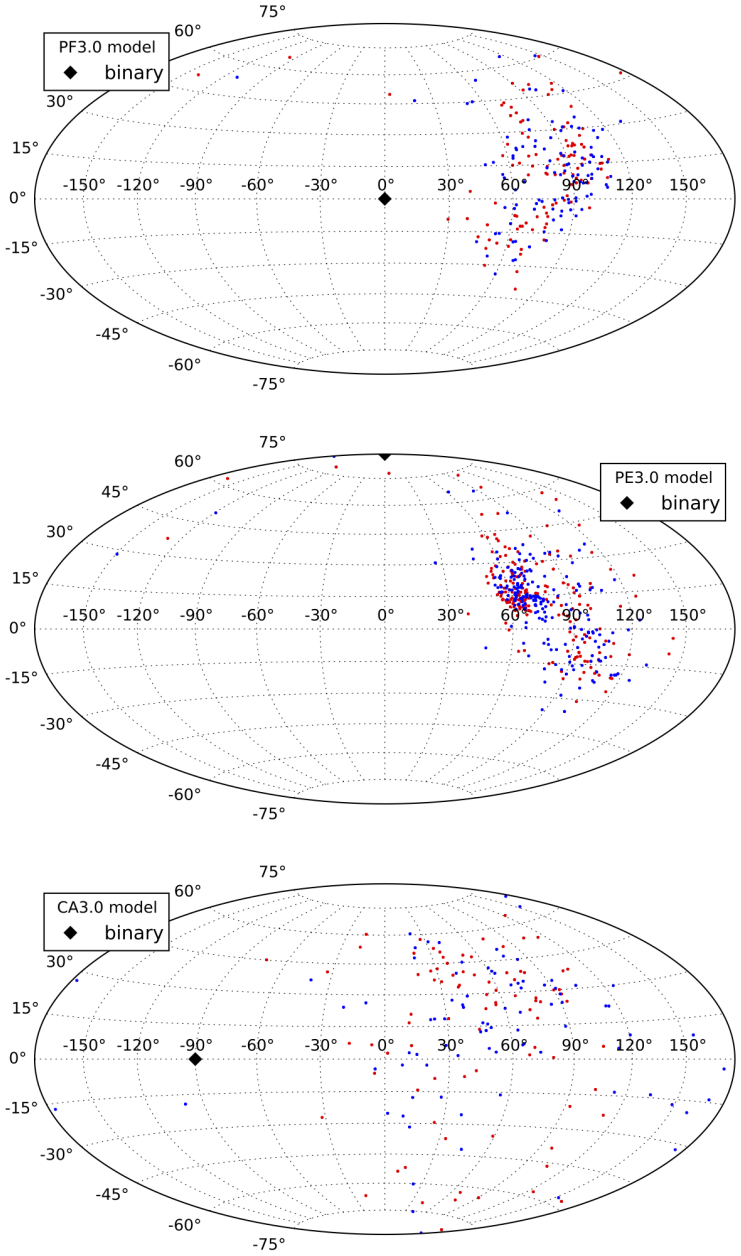

FIGURE 3.8: Evolution of the direction of all the accreted gas by each SMBH (red and blue dots) in a Hammer projection. The different plots correspond to different inclinations: counter-aligned (upper left), perpendicular edge-on (upper right) and perpendicular face-on (bottom). As indicated in the legend, all correspond to the larger impact parameter. The black diamonds indicate the binary direction. Notice how in all cases the gas tends to follow the initial orientation of the cloud, located always at $(90°, 0°)$, and not the orientation of the binary. The effect is weakest for the counter-aligned orbit case.

For the counter-aligned orbits (upper left panel of Fig. 3.8) the different orientations of the gas are not concentrated around any particular point. However, they are preferentially on the right side of the projection, which indicates that the gas tends to be counter-aligned with respect to the binary rotation. On the other hand, for both perpendicular orbits (upper right and bottom panel of Fig. 3.8) the gas tends to cluster more clearly around $(90°, 0°)$, which is the initial direction of the cloud orbit. This is because the dynamical interaction with the binary is not able to efficiently change the angular momentum direction of the surrounding gas on such short time-scales. In conclusion, the mini-discs that might arise from these perpendicular accretion events will be completely misaligned with respect to the binary orbit, but they are likely to be roughly aligned with each other.

Due to the large misalignment between the possible mini-discs and the binary, I expect other periodic effects to appear, like the Kozai–Lidov oscillations (Kozai, 1962; Lidov, 1962), where a test particle around one component of the binary periodically exchanges its inclination for eccentricity. Using hydrodynamical simulations, Martin et al. (2014) showed that this effect is also present in fluid discs. The time-scale for these oscillations is expected to be several times the binary orbital period – Martin et al. estimate $t_{\rm KL} \approx 17(0.35a/R_{\rm out})^{3/2}P_b$ for an equally-massive, circular binary and a mini-disc with surface density given by $\Sigma \propto r^{-1.5}$, which implies periods over 20 binary periods for mini-discs inside the Hill radius. However, the changes on the disc inclination and eccentricity are large, which could have implications on processes such as the shaping of jets, the feeding onto the SMBHs and star formation.

In summary, as hinted by this set of simulations, the misalignment appears to be a natural outcome from infalling cloud events, even when their orbits are aligned with the binary. Through the particular dynamics due to the interaction with the non-Keplerian gravitational potential of the binary, this could have important implications on the observability of these systems (see Section 3.6).

3.5 Circumbinary discs

As shown in Section 3.2, a circumbinary disk promptly forms[2] whenever the impact parameter of the infalling cloud is large enough (or when its orbit is retrograde to that of the binary). However, my simulations are too short to assess the physical properties of these discs as they evolve toward a (possibly) steady state. In order to investigate the longer term evolution of these discs, I take two representative cases (namely, cases A3.0 and PE3.0 in table 3.1). I re-simulate them for ≈ 30 further SMBHB orbits, using the final snapshots as initial conditions, but keeping only a sub-set of the particles, to save computational time. I selected only particles bound to the binary with a period smaller than 30 times the binary period, as the contribution of the excised particles is dynamically negligible.

The PE3.0 model is particularly interesting, because the circumbinary disc retains memory of the original orientation of the cloud and it is, therefore, perpendicular to the binary orbit. Column density maps at the beginning and the end of the re-simulation, from two edge-on views of the binary, are shown in Fig. 3.9. In the lower panel, where the disc is seen roughly edge-on, it tends to slowly align to the binary orbit. In order to measure this evolution, I use the total angular momentum of the gas within a fixed radius as a proxy for the direction of the disc. The evolution of the inclination angle is shown in Fig. 3.10 for different definitions of the disc extent,

[2] within the simulated 20 orbits or so

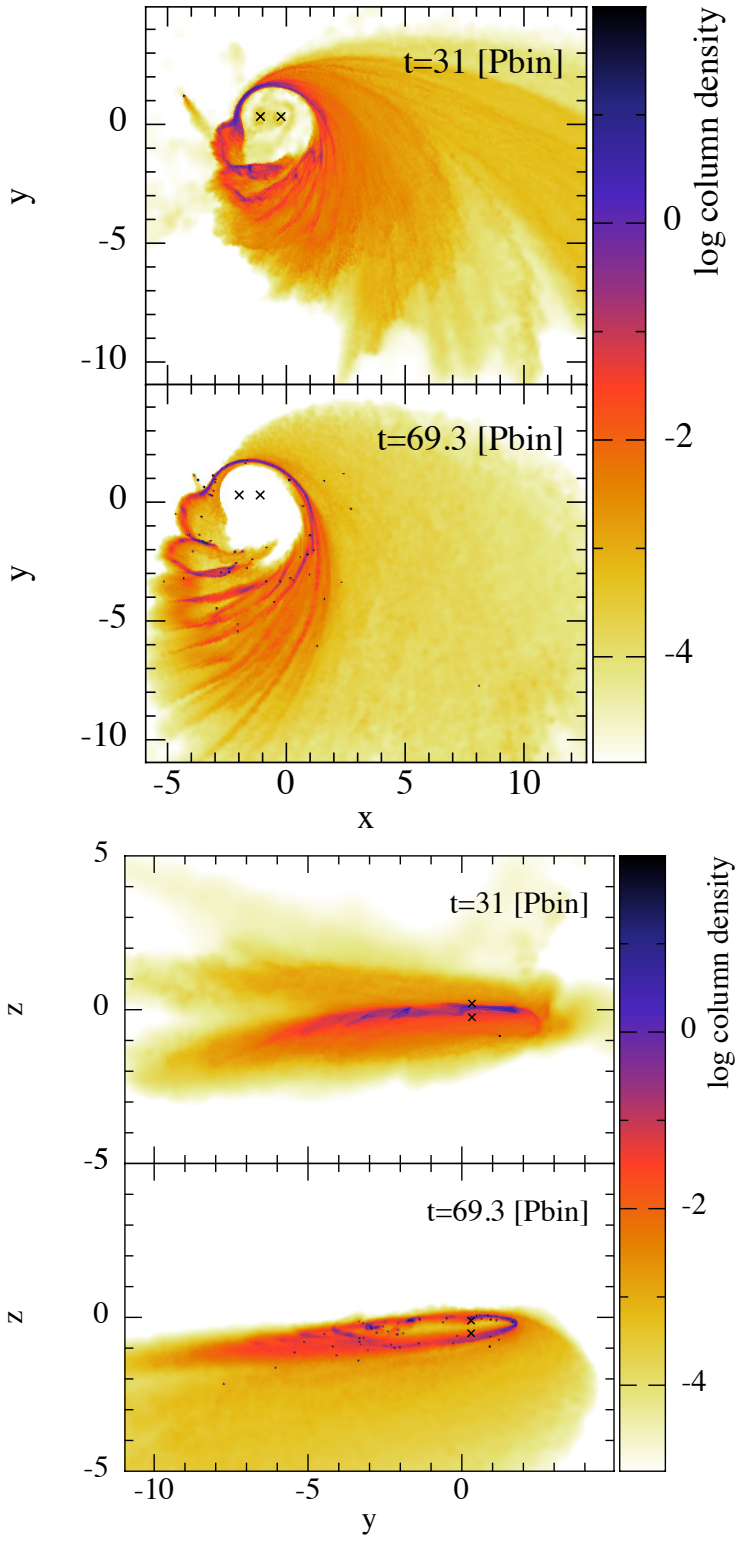

FIGURE 3.9: Column density maps of the PE3.0 re-simulation. The different times correspond to the beginning and the end of the re-simulation. The upper and lower panels show face-on and edge-on views of the disc, respectively.

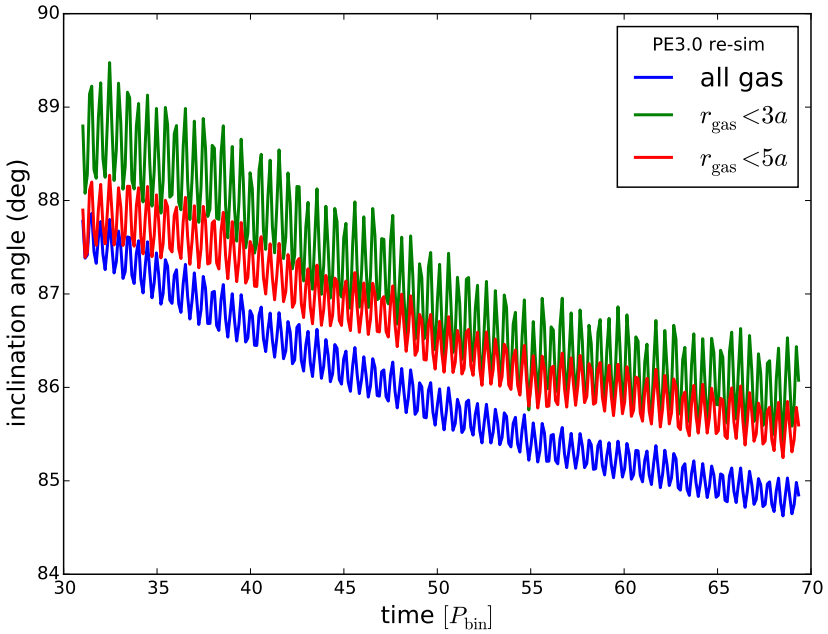

FIGURE 3.10: Time evolution of the gas inclination of the re-simulation of the PE3.0 model. Because the circumbinary disc is not a well-defined structure, I sum the angular momentum of all the gas, and also only that within two different radii, as indicated on the legend.

showing that this result is robust. I estimate that the alignment timescale is around 1000 orbits, should the evolution remain roughly constant. However, as explained for the mini-disc evolution, this timescale will depend critically on the viscosity treatment. I also notice that the inclination evolution shows the same oscillations that the mini-discs showed in the aligned case. These oscillations have also half of the binary period, as expected since the dynamics is driven by similar processes as in the former case. This periodic perturbation has been overlooked in most studies of misaligned discs because it does not have a secular effect on its evolution. However, my model suggests that it might have some interesting implications. For example, the density waves produced by the oscillatory perturbations enhance fragmentation of the gas, seen in the form of clumps in Fig. 3.10. Some of these clumps may form stars, a fraction of which will end up producing observable tidal disruption events (TDEs; see Section 3.6). Another possible signature of this oscillation might be imprinted in the shifting of spectral lines, specially coming from the inner regions where their amplitude is larger. The longer simulation also allows to investigate trends in the circumbinary disc eccentricity. By inspecting the face-on views (upper panels of Fig. 3.9) it seems that the material is more concentrated on eccentric orbits towards the end of the simulation. In order to measure this, I plot the eccentricity distribution at three selected times in the upper panel of Fig. 3.11. The distribution becomes narrower as the simulation advances, but actually keeps essentially the same median eccentricity of ≈ 0.6.

For the re-simulated A3.0 model, column density maps for the beginning and the end are shown in Fig. 3.12. As expected, the gas and the binary are essentially coplanar, with an initial inclination of only $\approx 4^\circ$, which decreases by $\approx 0.5^\circ$ during the re-simulation. The eccentricity evolution, shown in the lower panel of Fig. 3.11, is more interesting. Here a different behaviour with respect to the model PE3.0 is

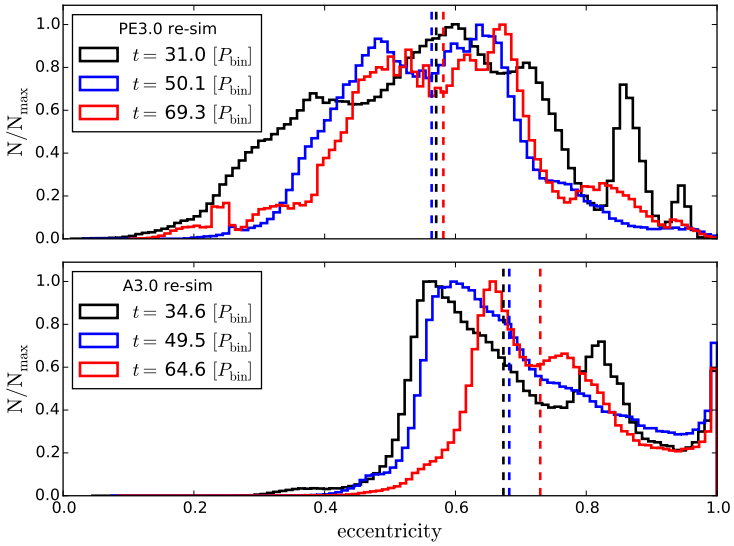

FIGURE 3.11: Eccentricity distribution of the gas for PE3.0 (top) and A3.0 (bottom) re-simulations at different times. Each distribution is normalised by its maximum value. The vertical, dashed lines indicate the median of each distribution. For the perpendicular disc the distribution narrows, keeping roughly constant its median value, while for the aligned disc the distribution shifts towards higher values with time.

observed; the orbits become more eccentric as time advances, which is reflected in the shifting of the distribution towards higher values and a clear increase of the median.

Finally, a clear circumbinary ring also appears in my simulations of the counter-aligned cases, for all the investigated initial parameters (see upper middle row of Fig. 3.3). In this configuration, the formation of a clear circumbinary structure is extremely quick, and mass adds-up as the very eccentric tail joins it. I show the evolution of the gas eccentricity distributions in Fig. 3.13. At the beginning the distribution is completely skewed towards high eccentricities due to the initial conditions, but after the interaction with the binary the gas eccentricity shifts towards lower values, and a striking bi-modality appears. This is clearly related to the formation of the ring, and it occurs on shorter time-scales for smaller impact parameters.

All the circumbinary discs appear to evolve differently according to their relative inclination to the binary. In the aligned model, the gas tends to increase its eccentricity; in the counter-aligned it tends to become circular, while in the perpendicular the eccentricity retains its value. This is driven by the dynamical interaction with the binary: a prograde encounter of a gas particle with one of the SMBHs will tend to increase its specific energy and angular momentum, increasing the eccentricity; on the other hand, a retrograde encounter will work in the opposite direction, circularising the material. For the perpendicular encounters, the binary is unable to change the orbital angular momentum of the gas, keeping its eccentricity roughly constant during the interaction.

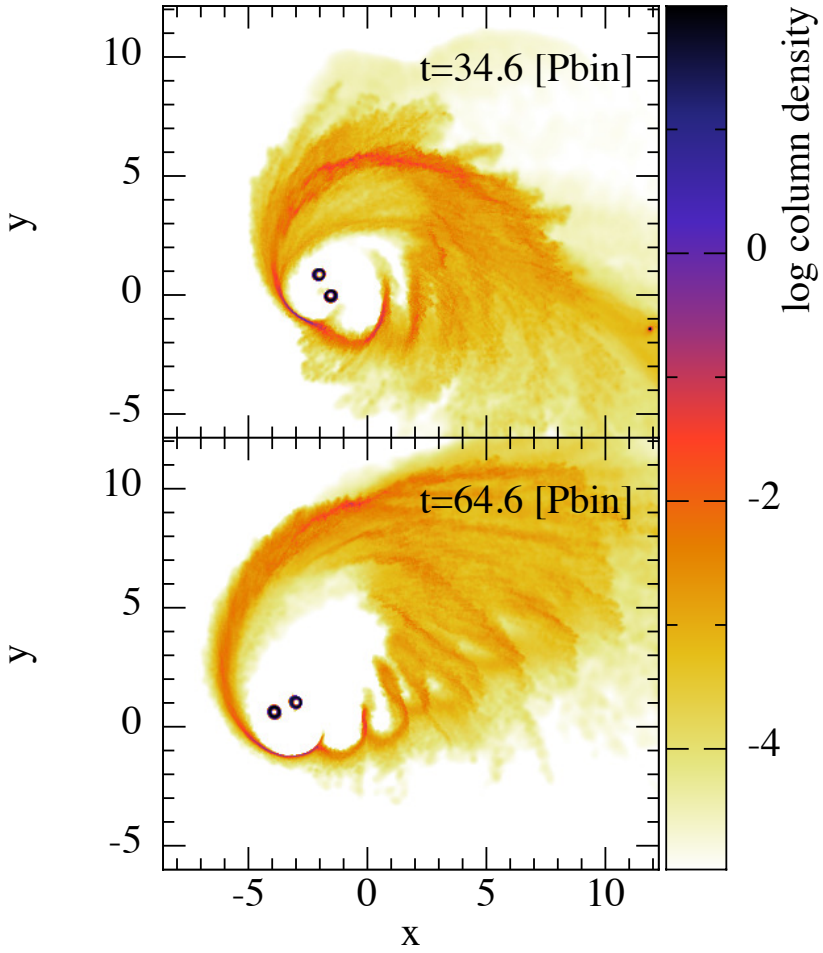

FIGURE 3.12: Column density map at the beginning and the end of the A3.0 re-simulation. In this case I only show a face-on view of the disc and the binary, because they are almost completely aligned. Here the disc increases its eccentricity.

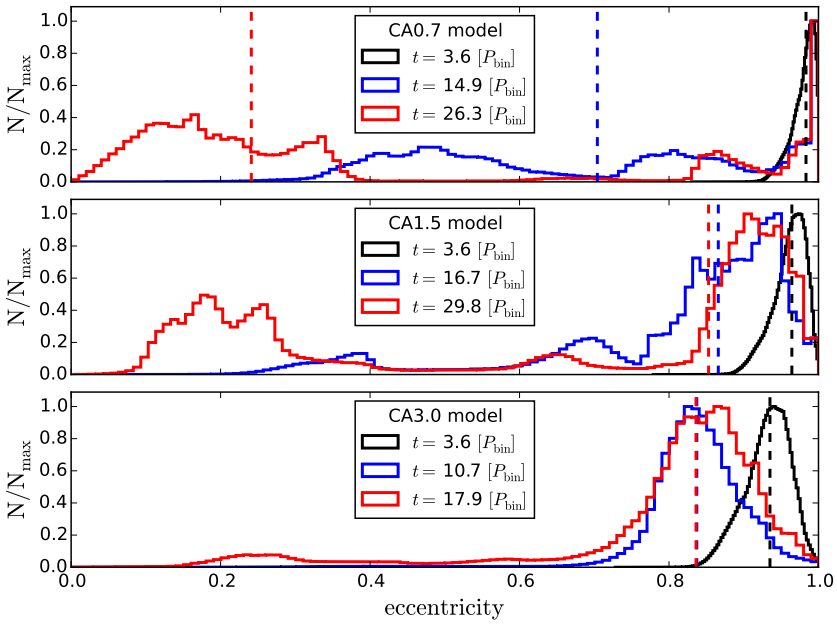

FIGURE 3.13: Eccentricity distribution of the gas for the counter-aligned simulations at different times, increasing impact parameter from top to bottom. Each distribution is normalised by its maximum value. The vertical, dashed lines indicate the median of each distribution. In the three models the material decreases its eccentricity with time, reaching values close to zero. This process occurs faster for smaller impact parameters.

3.6 Physical scaling and observational consequences

The efforts to confirm observationally the existence of SMBH binaries have increased in the last few years, motivated by their key role as probes of the hierarchical growth of galaxies (Sesana et al., 2011). Observing these objects is unfortunately very challenging, as their separations cannot be resolved by current capabilities in most galactic nuclei. Additionally, for the very few existing candidates, the observed signatures can also be explained by alternative scenarios that do not require a SMBHB (for a compilation of candidates and prospects in observational searches for SMBHBs, see Dotti, Sesana, and Decarli 2012 and Bogdanović 2015).

In the late stages of their evolution, when the binary separation is sufficiently low ($\lesssim 10^{-3}$ pc), gravitational waves will efficiently extract angular momentum and energy, rapidly leading to coalescence. The enormous amount of gravitational wave emission will be detectable by pulsar timing arrays (Sesana, 2013) or by space-based missions like eLISA (Amaro-Seoane et al., 2013). However, these detections will need to be complemented with observations in the electromagnetic spectrum in order to localise and characterise the sources.

3.6.1 Physical scaling

In order to link my results with possible observational signatures I scale all physical quantities from code to physical units. To perform the scaling, I have to choose two parameters: the mass of the binary and the critical density for the equation of state (eq. 2.36); fixing these two values will determine the rest of the units.

TABLE 3.2: Compilation of physical units of the initial values on my simulations. From left to right: binary mass, critical density for EoS, separation of the binary orbit, separation in terms of Schwarzschild radius, binary period, cloud mass, initial distance between the cloud and the binary, cloud radius, modulus of the cloud initial velocity, cloud velocity at the periastron for the smaller impact parameter, initial temperature of the cloud.

$M_{\rm bin}$ ($M_\odot$)	$\rho_{\rm cr}$ (g cm^{-3})	a (pc)	$a/R_{\rm sch}$	$P_{\rm bin}$ (yrs)	$M_{\rm cl}$ ($M_\odot$)	$R_{\rm cl}$ (pc)	$v_{\rm ini}$ (km/s)	$v_{\rm peri,0.7}$ (km/s)	$T_{\rm ini}$ (K)
10^6	10^{-14}	0.2	10^6	8370	10^4	0.5	40.8	342.9	100
10^6	10^{-12}	0.04	2×10^5	837	10^4	0.1	85.7	720	470
10^6	10^{-10}	0.009	5×10^4	84	10^4	0.02	187.7	1577.3	2170
10^7	10^{-14}	0.4	2×10^5	8370	10^5	1	85.7	720	470
10^7	10^{-12}	0.09	5×10^4	837	10^5	0.2	187.7	1577.3	2170
10^7	10^{-10}	0.02	10^4	84	10^5	0.05	408	3429	10^4
10^8	10^{-14}	0.9	5×10^4	8370	10^6	2.3	187.7	1577.3	2170
10^8	10^{-12}	0.2	10^4	837	10^6	0.5	408	3429	10^4
10^8	10^{-10}	0.04	2×10^3	84	10^6	0.1	877.2	7372.5	4.6×10^4

In Table 3.2 I present physical scaling down to 84 years. Shorter periods would require too large densities compared to what is observed for molecular clouds. Moreover, for the more massive systems, a period of 84 years already implies a cloud temperature of $\sim 10^4$ K, which is already unrealistically high (see e.g. Meijerink, Spaans, and Israel, 2007) and cannot be pushed further. A period of roughly a century is too long to look for the variability associated to it in observed data. Nevertheless, even if my model is unable to represent directly more compact systems, I still expect that the behaviour I find is qualitatively representative of those more rapidly varying systems, and below I discuss several possible observational signatures.

3.6.2 Observational signatures

The feeding rates onto the binary and each SMBH show variability for all the configurations I model, always related with the orbital period. Recall that I measure the accretion rates at the sink radius $R_{\rm sink}$, which is large compared to the Schwarzschild radius. Still, what AGN observations reveal is the luminosity of the accretion disc at different radii depending on the measured wavelength. I expect the variable accretion rate obtained at $R_{\rm sink}$ to represent actual variability of the accretion disc at large radii, which in some AGN shows up in optical or infrared light curves (e.g., Lira et al., 2011).

Variability due to binary feeding could thus appear in AGN light curves (see Sillanpaa et al., 1988, for the iconic case of OJ 287), and be detected with future time-domain surveys like the Large Synoptic Survey Telescope (LSST; Ivezic et al., 2008). Interestingly, periodicity has been recently claimed for a couple of systems proposed as binary candidates (Graham et al., 2015a; Liu et al., 2015).

The presence of the mini-discs in my simulations, with their misalignment and evolution, allows to explore novel and promising observational features. Graham et al. (2015a) showed that the blazar PG 1302-102 has a roughly sinusoidal light curve with a period of ≈ 5 years, and mentioned as a possible explanation the precession of a jet. Assuming that the orientation of a possible jet is given by the mini-disc[3], I expect to observe variability related to the mini-disc wobbling found in my models and predicted earlier by Bate et al. (2000), specially if the jet is close to the line of sight. Graham et al. (2015a) fitted the observed light curve with a wobbling amplitude of around 0.5° which is actually very close to what I find in Fig. 3.7. Therefore, I suggest that the observed variability of this source could be due to mini-disc wobbling as shown in my models. Notice that this interpretation would imply a rest-frame orbital period for the binary of eight years, one order of magnitude longer than under the assumption that the variability is due to lumps in the circumbinary disc (D'Orazio et al., 2015).

In the cases where the viscosity of the individual discs is low, the differential precession induced by the companion SMBH is not communicated efficiently throughout the discs, which then could break. The disruption of the disc into rings that precess independently could also be a source of variability, as the dissipation between the gaseous rings is enhanced and this promotes stronger accretion onto the central SMBH (Doğan et al., 2015). There is recent observational evidence for this process in a proto-planetary disc (Casassus et al., 2015).

Additional observable features could be due to warps in the misaligned mini-discs. I do not find warps in the simulations due to the relatively low

[3]The jet orientation could also be given by the spin of the SMBH, which is not necessarily related with the mini-disc orientation, specially at these scales.

resolution afforded. However, they are expected due to the gravitational pull of the companion (Moeckel and Bally, 2006). The presence of a warp can cause part of the disc to block other parts of the disc or a central source. Additionally, it can change the viewing angle which is important for synchrotron emission. Both effects occur periodically, on the dynamical time-scale of the disc. The effects of warps have been observed in several astrophysical objects such as active galactic nuclei, circumstellar discs and stellar mass black holes through variability in (i) the photometry (e.g. Herrnstein et al., 2005; Manset et al., 2009; Bouvier et al., 2013); (ii) the spectrum (e.g. Reynolds et al., 2009; Looper et al., 2010); and (iii) polarisation (e.g. Manset et al., 2009; Roland et al., 2009; Cheng et al., 2016).

Circumbinary discs can also have variable emission. In particular, Figures 3.9 and 3.12 show a series of discrete shock fronts propagating from the binary into the tail of the eccentric disc. Such regular features are not seen in comparable simulations featuring a single SMBH (Bonnell and Rice, 2008). Material approaching the periastron is accelerated and flung away into the tail when it is in phase with one of the two SMBHs. This creates ejected waves with a periodicity of half the binary orbital period that compress and shock the surrounding material, possibly leading to periodic enhancements in luminosity and discrete episodes of star formation. As the gas is located farther from the black holes ($r \gtrsim 2a$, for a prograde disc), I expect the period of such variability to be typically longer than the binary period (e.g. Farris et al., 2015b). Then, a source with a photometric period shorter than the spectroscopic period could be interpreted as a binary surrounded by a disc – the binary varies on one, or half, an orbital period due to accretion, while the circumbinary varies on its own dynamical time. Moreover, the ratio between both variability periods could be a tool to study the geometry and extension of the gas around the binary.

I have shown that increasing the impact parameter results in more clumping for the gas. The presence of clumps could have indirect implications on the observability of a binary through star formation and posterior tidal disruption events (TDEs). Amaro-Seoane, Brem, and Cuadra (2013) showed that fragmentation in a circumbinary disc results in *in-situ* star formation and an increase of the rate of TDEs with respect to what is expected for typical galaxies. Later on, Brem et al. (2014) demonstrated that the presence of the binary instead of a single SMBH will produce a distinctive signature on the reverberation mapping after such an event. Based on this, I might expect to detect these circumbinary structures through TDEs. However the rate will depend on the efficiency of star formation in the gas tail and the disc itself, which I do not model here. In any case, LSST will detect thousands of TDEs, greatly increasing the chances of detecting this kind of events even if they are relatively rare.

Finally, star formation in a circumbinary disc could also refill the loss-cone and affect the evolution of the binary orbit by exchange of energy and angular momentum with the stars via 3-body interactions (Amaro-Seoane, Brem, and Cuadra, 2013). Moreover, eccentric discs of stars, which is the most likely outcome of the near-radial infall of clouds (Figures. 3.11 and 3.13), will be subject to instabilities (see e.g. Madigan, Levin, and Hopman, 2009) that can increase even further the amount of stars with orbits that will interact directly with the binary, enhancing the probability of TDEs and/or evolving the binary orbit.

Chapter 4

Single cloud infall: binary dynamical evolution and the final parsec problem

In this chapter I model the dynamical effects that the interaction with an infalling cloud has on the SMBHB orbit, using very similar simulations as in the previous chapter. I focus on the angular momentum transfer and on the evolution of the binary orbital elements, paying particular attention to the early phases of the interaction, when most of the angular momentum transfer occurs.

4.1 The numerical model

I model the interaction between the gas clouds and the SMBHBs using the SPH technique, similar to what I described in the previous chapter. The binary consists of two sink particles, initially having equal masses and a circular orbit. On the other hand, the cloud is initially spherical with uniform density, a turbulent velocity field, and a total mass 100 times smaller than the binary.

By changing the initial orbit of the cloud, I model a total of 13 systems. The first 12 systems are the same described in Chapter 3, which correspond to the combination of 4 different orientations relative to the binary orbit (Aligned, Counter-aligned, Perpendicular edge-on and Perpendicular face-on) and 3 pericentre distances ($r_{\rm p} = 0.7, 1.5, 3 R_{\rm bin}$, where $R_{\rm bin} = 0.5a$ is the initial binary radius). I model an additional impact parameter ($r_{\rm p} = 6 R_{\rm bin}$) for the Aligned configuration, needed to reach a significant decrease of both the accreted mass and orbital changes (more details on this choice are given in § 4.4.1).

Throughout the chapter I use the same nomenclature for the different models as before, namely, the letters indicate the orbit orientation (A: aligned, CA: counter-aligned, PE: perpendicular edge-on, PF: perpendicular face-on) and the number is the pericentre distance.

The only significant difference with respect to the models presented in the previous chapter is that this time, to avoid numerical issues in the orbit integration, I follow the dynamics of the SMBHs using a fixed time-step, set equal to $10^{-4} P_0$, where P_0 is the initial binary orbital period. Finally, as the changes produced by the low-mass clouds are expected to be small, I improved the time resolution compared to the simulations shown in the previous chapter by decreasing the Courant factor from 0.1 to 0.03. This factor determines the size of the hydrodynamical time-step for each gas particle. With this increase in time resolution I ensure a better conservation of the total angular momentum of the system during the early interaction between the binary and the gas. This change allows to disentangle the binary evolution from

the numerical noise (§ 4.2.1) without the need to remove the SMBHs from the tree calculation of the gravitational forces (see e.g. Roedig et al., 2011).

4.2 Dynamical evolution of the system

4.2.1 Angular momentum conservation

I expect only small changes in the binary orbit because its mass is significantly larger than that of the cloud. Therefore, it is important to establish whether these simulations have the accuracy to measure these effects. With that aim, I measure the conservation of angular momentum in the different models, as shown in Fig. 4.1. The figure shows that the $\Delta L/L$ experienced by the binary is much larger than the fluctuations in total $\Delta L/L$ due to inaccuracy of the code. The upper panels show that $\Delta L_{\rm bin}$ is much larger than the level of total L conservation in the code, generally by a factor of five, but typically much better. The lower panels allow to identify *when* the binary evolution is trustworthy, as explained below.

Notice that due to the finite size of the sink radius, I expect some loss of angular momentum throughout the binary evolution as the gas is accreted by each SMBH. However, I estimate that the cumulative effect of this loss is at most of the order of $\sim 10^{-4} L_0$, which is significantly smaller than the changes observed for the total angular momentum of the system in Fig. 4.1. Therefore, these deviations are due to the numerical inaccuracies of the code.

The Lagrangian formulation used by SPH codes to solve the hydrodynamical equations conserve angular momentum exactly. However, the numerical integration of these equations using individual particle time-steps, coupled with the approximation of gravitational forces through a tree algorithm, introduce numerical noise in the quantities that the code computes, in particular, the angular momentum (Springel, 2005). Given these inaccuracies, the simulations can only be trusted to the point where the numerical noise starts to dominate the evolution of the system. This is defined as the time at which the fluctuations of the total angular momentum are of the order of the changes in the binary's angular momentum, and it is indicated in Fig. 4.1 by the dashed vertical lines. In practice, I compute the amplitude of the fluctuations in $\Delta L/L$ for both the entire system and the binary in chunks of half binary orbital periods. When the ratio of the former to the latter becomes larger than $1/2$, I discard the subsequent binary evolution. In these models this always happens at $T \gtrsim 8P_0$, being P_0 the initial binary period. Note that most of the evolution of $L_{\rm bin}$ occurs at $T < 8P_0$, corresponding to the phase in which most of the mass is accreted by the SMBHB. For the PE and PF simulations this period is actually longer because of the prolonged accretion, but angular momentum fluctuations are correspondingly smaller. This indicates that significant $\Delta L_{\rm bin}$ is driven by torques exerted by accreting particles, closely interacting with the SMBHB. When accretion stops, also the binary evolution is dumped to a level consistent with the numerical accuracy of the code. This is because the cloud is light, and gas that does not interact strongly with the binary hardly modifies its dynamics. The robust study of the secular evolution of the system requires refining some parameters of the simulations (e.g. opening angle of the tree), which translates in considerable computing times not affordable with the standard configuration.

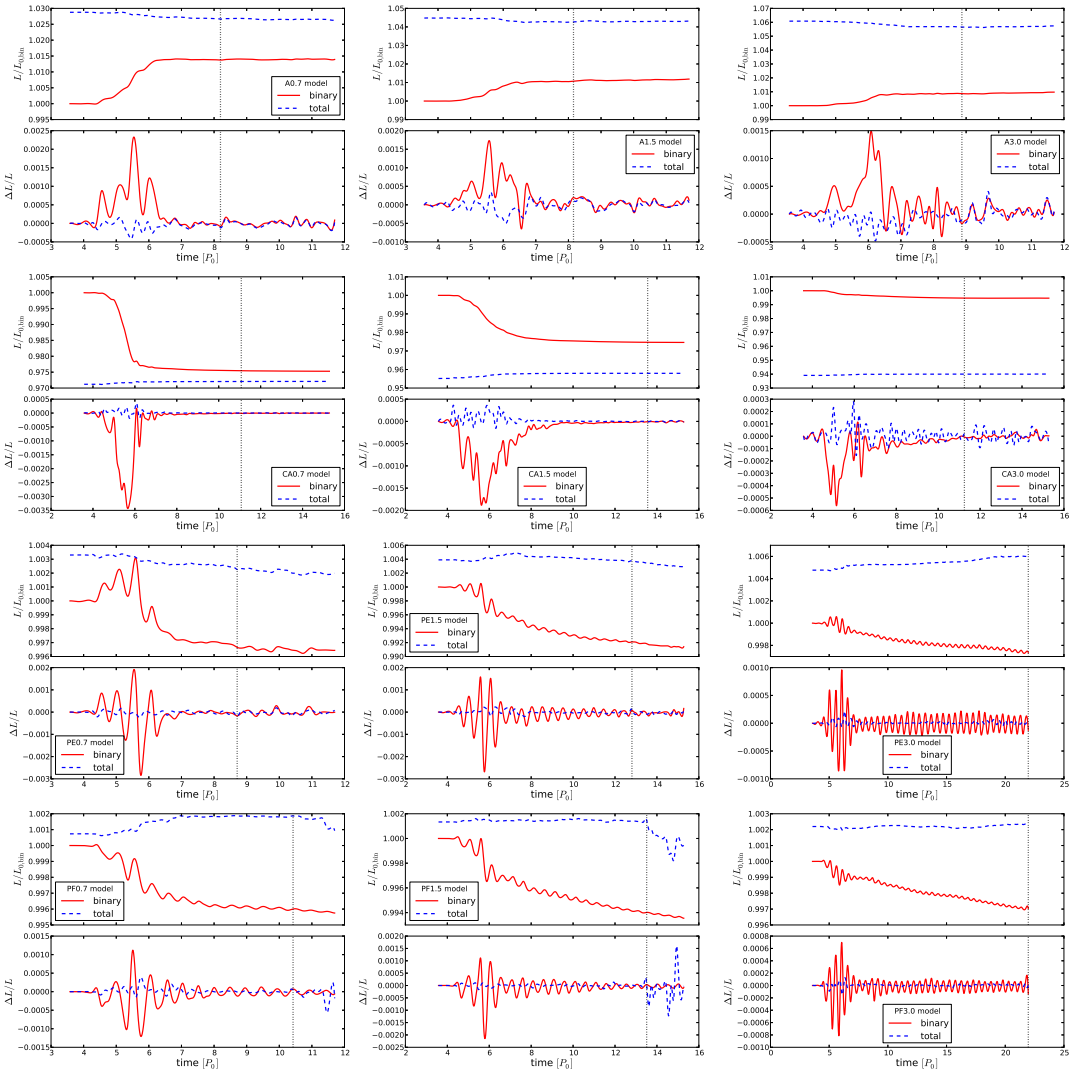

FIGURE 4.1: Evolution of the angular momentum of the entire system (blue) and the binary (red) for twelve of my models. The upper plots of each panel show the total magnitude of the angular momentum vector normalised by the binary initial value, while the lower plots show the relative change between successive snapshots. The impact parameter increases from left to right, and each row represents a different inclination, as indicated in the legends. The vertical dashed line indicates the time when the fluctuations of the total angular momentum are larger than half of the changes of the binary angular momentum. Note the different vertical scales in each panel.

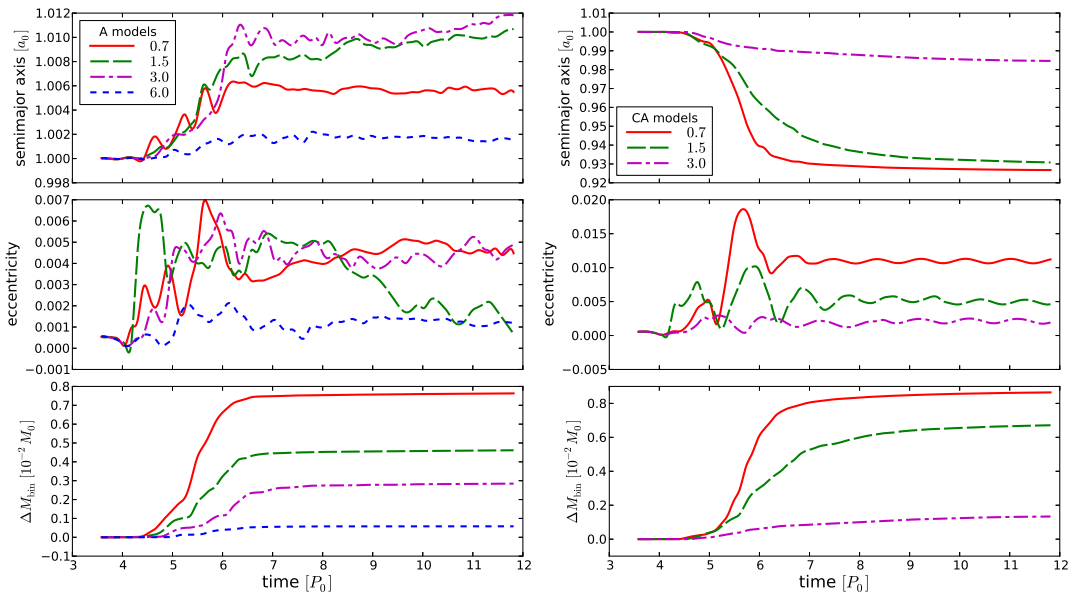

FIGURE 4.2: Evolution of the binary semimajor axis (upper panels), eccentricity (middle panels) and accreted mass (lower panels) for the A and CA models. The different lines in each panel represent the different pericentre distances, as indicated in the legend.

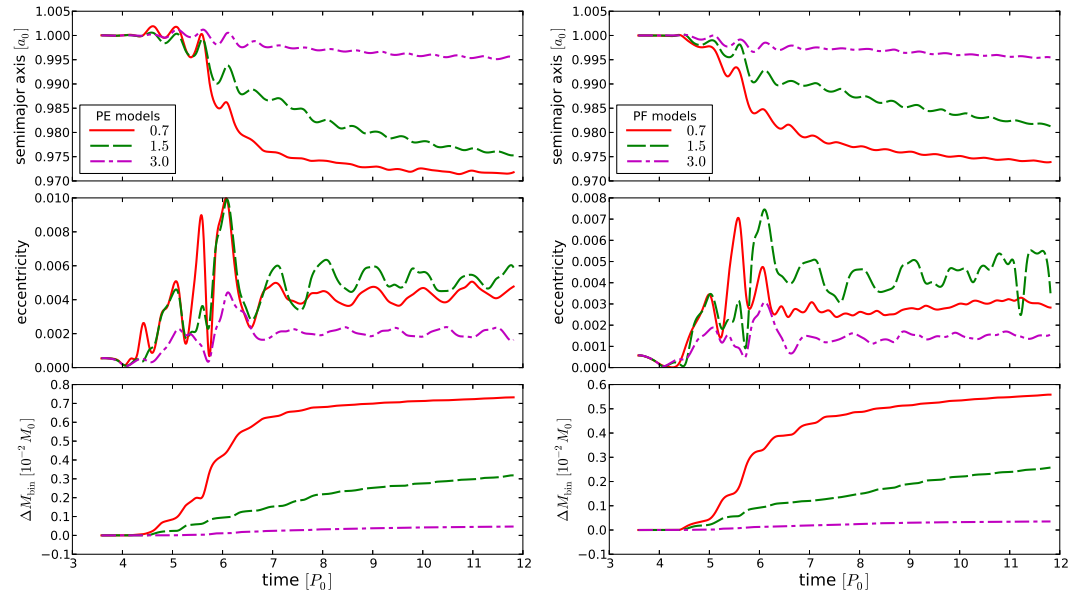

FIGURE 4.3: Same as Fig. 4.2, but for the perpendicular simulations (PE and PF models).

TABLE 4.1: Total change of the binary angular momentum (ΔL), mass (ΔM) and semimajor axis (Δa) for the different orbits modelled, from the beginning of the simulation up to $t_{\rm conf}$, which is the time where it is no longer possible to disentangle the physical interaction from the numerical noise.

Model	$t_{\rm conf}$ (P_0)	ΔL (L_0)	ΔM (M_0)	Δa (a_0)
A0.7	8.1	0.01380	0.00754	0.00545
A1.5	8.1	0.01058	0.00453	0.00829
A3.0	8.9	0.00864	0.00278	0.00982
A6.0	8.8	0.00137	0.00058	0.00160
CA0.7	11.1	−0.02456	0.00862	−0.07312
CA1.5	13.5	−0.02532	0.00678	−0.06988
CA3.0	11.3	−0.00529	0.00132	−0.01521
PE0.7	8.7	−0.00335	0.00695	−0.02707
PE1.5	12.8	−0.00790	0.00334	−0.02547
PE3.0	22.0	−0.00265	0.00080	−0.00764
PF0.7	10.4	−0.00399	0.00542	−0.02389
PF1.5	13.5	−0.00600	0.00281	−0.02013
PF3.0	21.8	−0.00283	0.00076	−0.00796

4.2.2 Binary evolution

I present the results of the transient evolution of the binary orbital components and mass in Figures 4.2 and 4.3. The bulk of accretion occurs during the first few orbits ($\approx 4-8$), which correspond to the first passage of the cloud. This is the same period where a significant change of the orbital parameters occurs, especially the semimajor axis, which implies that the dynamical evolution of the binary is intimately related to the accretion. The eccentricity evolution for every system is extremely small, typically less than 1%, which means that the binary remains roughly circular during the transient interaction with the gas cloud. For this reason I restrict the analysis to the semimajor axis evolution.

Finally, I summarise the total change of the binary angular momentum, mass and semimajor axis for every configuration in Table 4.1, up to the time where numerics can be trusted, as described in the previous section.

4.3 Angular momentum exchange

In order to link the evolution of the binary angular momentum to that of the semimajor axis and mass, I write the magnitude of the angular momentum as a combination of the binary properties, similar to what is shown in Roedig et al. (2012). However, instead of writing it as a function of the total binary mass M and the reduced mass μ, I consider M and the mass ratio q. This way, the effect of total accretion (changing M) from that of differential accretion onto the two masses (changing q) can be separated.

The magnitude of the binary angular momentum is

$$L_{\rm bin} = \frac{q}{(1+q)^2} M^{3/2} \sqrt{Ga(1-e^2)}, \tag{4.1}$$

where G is the gravitational constant. Differentiating with respect to all the parameters I get

$$\frac{\Delta L_{\rm bin}}{L_{\rm bin}} = \frac{1-q}{q(1+q)}\Delta q + \frac{3}{2}\frac{\Delta M}{M} + \frac{1}{2}\frac{\Delta a}{a} - \frac{e}{1-e^2}\Delta e. \tag{4.2}$$

In these models the binary remains approximately equal-mass and circular, $(1-q) \ll 1$ and $e \ll 1$, throughout the different simulations (see Figures 4.2 and 4.3). This means that the factors in front of Δq and Δe in eq. 4.2 are negligible compared to the $3/2$ and $1/2$ in front of $\Delta M/M$ and $\Delta a/a$, respectively. I can therefore approximate the total change in angular momentum based on the change in a and M only,

$$\frac{\Delta L_{\rm bin}}{L_{\rm bin}} \approx \frac{3}{2}\frac{\Delta M}{M} + \frac{1}{2}\frac{\Delta a}{a}. \tag{4.3}$$

This approximation is confirmed by the upper panels of Fig. 4.4, where I show the decomposition of the binary total angular momentum into its individual components. The contribution due to the evolution in mass ratio (dotted red lines) and eccentricity (long dashed cyan lines) is negligible compared to that due to the change in total mass (dotted-dashed green lines) and semimajor axis (dashed blue lines). The solid lines in each panel represent the binary angular momentum, black is the value measured directly form the simulations, while red is the one recovered by integrating the individual components of equation (4.2). Note that the black and red solid lines are indistinguishable from each other on this scale. In order to establish the resolution of the simulations, I compute the difference between these two lines, shown in the lower panels of Fig. 4.4. The differences displayed here are usually within the range $\sim 10^{-5} - 10^{-4} L_0$, which implies that the binary orbital elements are related to the angular momentum through the first order expansion (eq. 4.2) very accurately. These results, together with what I show in Fig. 4.1, confirm that the evolution of the systems is dominated by the physical interaction with the gas rather than numerical noise, at least during the prompt accretion phase.

4.3.1 Analytical estimate of the binary evolution

In order to estimate the expected evolution of L and a, I develop a simple analytical model based on the exchange of angular momentum through accretion only (i.e., ignoring the non-accreted gas). The initial angular momentum of the gas is determined by the initial conditions imposed for the cloud, as described in Chapter 3. Then, the average angular momentum of a portion of gas with mass $M_{\rm gas}$ is

$$L_{\rm gas} = dM_{\rm gas} v_{\rm ini} \sin\theta_{\rm vel}, \tag{4.4}$$

where $d = 15a$ is the initial distance of the cloud, $v_{\rm ini} = 0.25\sqrt{GM/a}$ is its initial orbital velocity, and $\theta_{\rm vel}$ is the angle between its velocity vector and the binary plane. Replacing the different values I obtain

$$L_{\rm gas} = \alpha M_{\rm gas}\sqrt{GMa}, \tag{4.5}$$

where

$$\alpha = \frac{15}{4}\sin\theta_{\rm vel} \approx 0.7, 1.1, 1.4, 1.8 \tag{4.6}$$

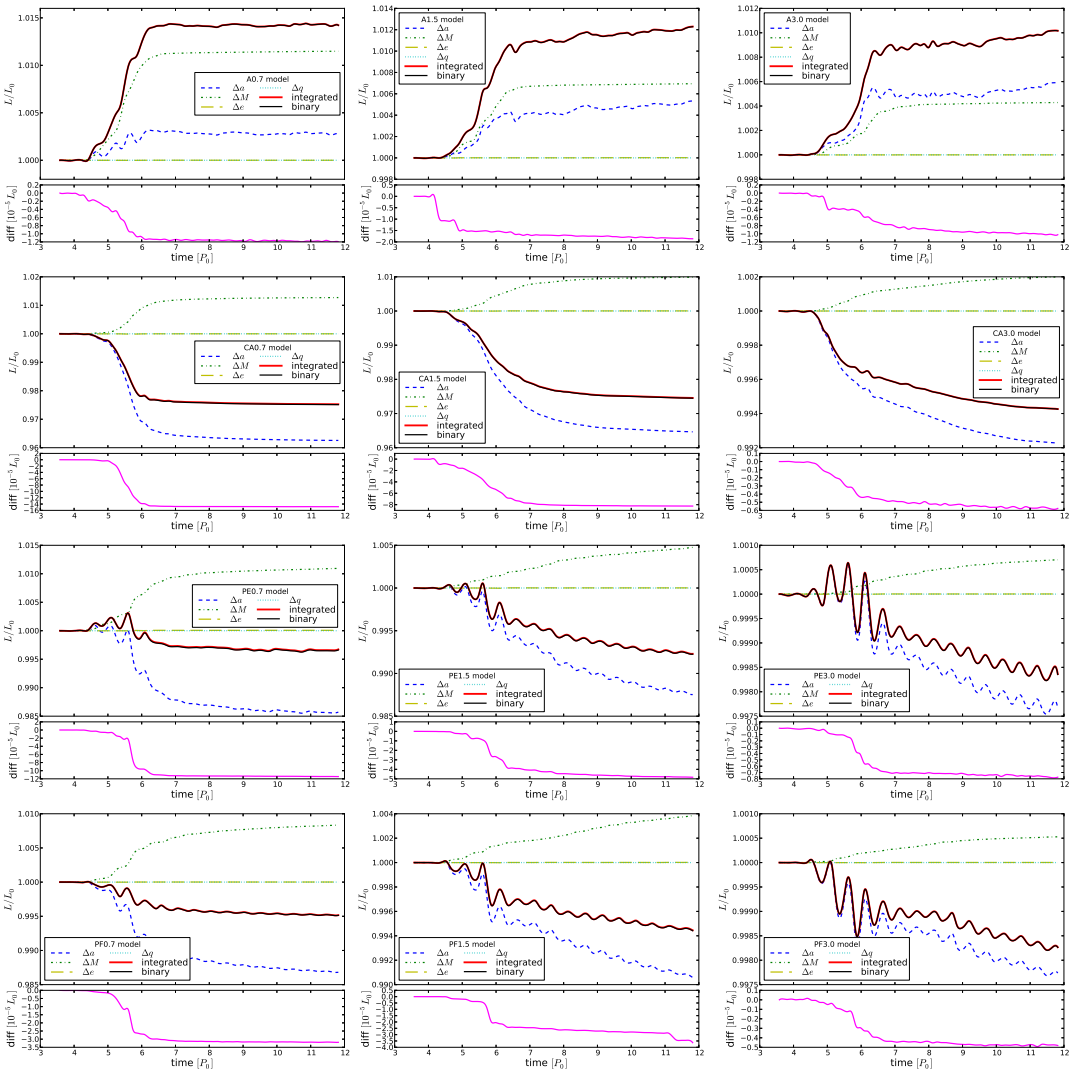

FIGURE 4.4: *Upper plots:* Decomposition of the binary total angular momentum following eq. 4.2 (non-solid lines), the sum of all components (solid red line) and the angular momentum of the binary computed directly from the snapshots (solid black line). The impact parameter increases from left to right, while the different inclinations are shown from top to bottom, as indicated on each legend. Notice that the Δq and Δe components of the angular momentum are indistinguishable from unity in these plots. *Lower plots:* Difference between the momentum measured from the snapshots and the value recovered from the contribution of all components.

for increasing impact parameter. Expressed in terms of the initial angular momentum of the binary $L_0 = \mu\sqrt{GMa}$

$$\frac{L_{\rm gas}}{L_0} = \alpha\frac{M_{\rm gas}}{\mu} = 4\alpha\frac{M_{\rm gas}}{M}. \tag{4.7}$$

In order to check if this approximation is correct I compute the equivalent α of the cloud as a whole at the beginning of the simulation. I obtain

$$\alpha_{\rm sim} = 0.73, 1.14, 1.55, 1.9 \tag{4.8}$$

which are very close to the values derived from the initial conditions, as expected. The small differences are due to the initial random turbulent velocity field.

Angular momentum evolution

I take the simple assumption that each accreted gas particle brings its initial angular momentum to the SMBHB. For the aligned (A) and counter-aligned (CA) cases, where the majority of the accretion occurs on the same plane to that of the binary, I simply add or subtract the angular momentum estimated using equation (4.7) by considering the appropriate $M_{\rm gas}$ (i.e., the total mass accreted in each case, see Table 4.1). The values obtained using this approximation and the comparison with the actual values measured from the simulations are shown in Table 4.2.

TABLE 4.2: Total evolution of the angular momentum magnitude (ΔL) and semimajor axis (Δa) for the A and CA models. The subscript 'est' corresponds to a value estimated using the initial simple model, while 'corr' is the corrected estimation using the appropriate α and including the slingshot, and 'meas' means that is measured directly from the simulations.

Model	ΔL_{meas} (L_0)	ΔL_{est} (L_0)	$\frac{\Delta L_{\text{est}}}{\Delta L_{\text{meas}}}$	ΔL_{corr} (L_0)	$\frac{\Delta L_{\text{corr}}}{\Delta L_{\text{meas}}}$	Δa_{meas} (a_0)	Δa_{est} (a_0)	$\frac{\Delta a_{\text{est}}}{\Delta a_{\text{meas}}}$	Δa_{corr} (a_0)	$\frac{\Delta a_{\text{corr}}}{\Delta a_{\text{meas}}}$
A0.7	0.0138	0.0211	1.53	0.0145	1.06	0.0053	0.0196	3.70	0.0064	1.20
A1.5	0.0106	0.0199	1.88	0.0114	1.06	0.0085	0.0263	3.09	0.0092	1.08
A3.0	0.0086	0.0156	1.81	0.0105	1.21	0.0098	0.0228	2.33	0.0127	1.29
A6.0	0.0014	0.0042	2.98	0.0013	0.93	0.0016	0.0066	4.13	0.0019	1.19
CA0.7	-0.0246	-0.0241	0.98	-0.0239	0.97	-0.0731	-0.0741	1.01	-0.0737	1.01
CA1.5	-0.0253	-0.0298	1.18	-0.0261	1.03	-0.0699	-0.0800	1.14	-0.0725	1.04
CA3.0	-0.0053	-0.0071	1.34	-0.0052	0.98	-0.0148	-0.0180	1.22	-0.0144	0.97

Comparing to the observed L evolution, those numbers are a factor of $\lesssim 3$ too large in the A cases and a $\leq 40\%$ overestimate in the CA cases. The first source for this discrepancy could be the non-accreted material, which interacts with the SMBHB taking away some extra angular momentum. This remaining gas is clearly seen in the form of minidiscs and circumbinary discs. In order to compute the amount of angular momentum acquired by the non-accreted gas, I directly identify from the simulations the remaining particles after the first passage of the cloud. Only for these particles I then compute the angular momentum difference with respect to the initial state, which comes from the interaction with the binary. For the A models I obtain

$$\left(\frac{\Delta L_{\rm out}}{L_0}\right)_{\rm A} \approx 0.0021,\, 0.0024,\, 0.0011,\, 0.0016, \tag{4.9}$$

for increasing impact parameters. Similarly, for the CA models

$$\left(\frac{\Delta L_{\rm out}}{L_0}\right)_{\rm CA} \approx 0.0029,\, 0.0036,\, 0.0031. \tag{4.10}$$

These values are around one order of magnitude too small to explain the overestimate of the angular momentum evolution.

The second effect that could account for these differences is that the accreted particles might have on average more angular momentum than their non accreted counterparts. In order to compute this, I estimate the average α of the accreted particles, which is an indication of their angular momentum budget. For the A models I obtain

$$\alpha_{\rm accr,A} = 0.55, 0.76, 1.04, 1.25 \tag{4.11}$$

while for the CA models

$$\alpha_{\rm accr,CA} = 0.61, 0.83, 0.98. \tag{4.12}$$

All these values are smaller than the ones I use based on the initial conditions (equation 4.6), which implies that I am overestimating the average angular momentum of the gas accreted by the binary. This is because the gas with larger angular momentum will typically have orbits with a periapsis further away from the SMBHB, avoiding being captured.

I estimate again the angular momentum change using a modified version of equation (4.7), where I implement these corrections described as follows:

$$\frac{\Delta L_{\rm bin}}{L_0} = 4\alpha_{\rm accr}\frac{\Delta M}{M} - \frac{\Delta L_{\rm out}}{L_0}. \tag{4.13}$$

The values obtained with this equation are shown in Table 4.2. These numbers are now in remarkable agreement with the actual binary evolution. The largest difference I obtain with this approximation is 20% for the A3.0 model – for all the other cases the discrepancies are not larger than 7%.

TABLE 4.3: Total evolution of the angular momentum inclination angle ($\Delta\theta$), semimajor axis (Δa) for the perpendicular models. The definition of the subscripts is the same as Table 4.2.

Model	$\Delta\theta_{\rm meas}$ (deg)	$\Delta\theta_{\rm est}$ (deg)	$\Delta\theta_{\rm corr}$ (deg)	$\Delta a_{\rm meas}$ (a_0)	$\Delta a_{\rm est}$ (a_0)	$\Delta a_{\rm meas}/\Delta a_{\rm meas}$	$\Delta a_{\rm corr}$ (a_0)	$\Delta a_{\rm corr}/\Delta a_{\rm meas}$
PE0.7	0.88	1.11	0.81	-0.0271	-0.0208	0.77	-0.0276	1.02
PE1.5	0.67	0.84	0.54	-0.0255	-0.0101	0.40	-0.0258	1.01
PE3.0	0.23	0.26	0.18	-0.0076	-0.0024	0.32	-0.0077	1.01
PF0.7	0.53	0.87	0.53	-0.0239	-0.0162	0.68	-0.0242	1.01
PF1.5	0.49	0.71	0.46	-0.0201	-0.0084	0.42	-0.0204	1.02
PF3.0	0.15	0.24	0.17	-0.0080	-0.0028	0.28	-0.0079	0.99

In the case of the perpendicular configurations, the main effect of the accreted gas will be to tilt the binary in the direction of the orbital angular momentum of the cloud, because the typical gas velocity will be perpendicular to that of the SMBHB. This is clearly seen in Fig. 4.5, where I show the time evolution of the angular momentum inclination angle respect to its initial orientation. I can quantify the tilt angle $\Delta\theta$ by applying the same approximation as before:

$$\sin(\Delta\theta) = \frac{\Delta L_{\rm bin}}{L_{\rm bin}} = 4\alpha\frac{\Delta M}{M}. \tag{4.14}$$

The values estimated using this expression are shown in Table 4.3, and are an overestimate of the measured ones. Similar as the other configurations, this is due to the mean α value of the accreted particles. For the PE models those are

$$\alpha_{\rm accr,PE} = 0.51, 0.71, 0.98, \tag{4.15}$$

while for the PF models I get

$$\alpha_{\rm accr,PF} = 0.44, 0.71, 0.98, \tag{4.16}$$

which appear to be consistent with the overestimations for both configurations. I estimate the inclination angles with equation (4.14), but using the values of $\alpha_{\rm accr}$, and present them in Table 4.3 ($\Delta\theta_{\rm corr}$). With this correction, I obtain values much closer to the measured ones, especially for the PF configurations. For the PE models, the corrected values are only a slight underestimate of the simulated ones.

In summary, using a simple analytical model based only on the angular momentum exchange between the accreted material and the binary I reproduce all the trends for the total evolution of the angular momentum vector (either magnitude or inclination). This confirms the hypothesis that the transient evolution of a binary during the near-radial infall of gaseous clouds is dominated by the accretion onto the SMBHB.

Semimajor axis evolution

I can now use equation (4.3) to estimate, in the same manner, the evolution of the binary semimajor axis, and compare it to what it is found in the simulation.

I start with the prograde and retrograde cases. By equating the right hand side of equation (4.3) to the right hand side of equation (4.7), and keeping in mind that the A case adds to the L budget, whereas the CA case subtracts, I get

$$\left(\frac{\Delta a}{a}\right)_{\rm A,CA} = -8\left(\frac{3}{8} \mp \alpha\right)\frac{\Delta M}{M}, \tag{4.17}$$

where the '$-$' sign corresponds to the A case and the '$+$' to the CA case. Comparing these estimates with what was measured in the simulation (Table 4.3), there is an overestimation of the binary shrinking in the corotating case, but I get close to the observed values in the retrograde case. All the discrepancies are consistent with the overestimation of the angular momentum change. If I compute Δa using an appropriate angular momentum change (i.e., $\Delta L_{\rm corr}$ from equation 4.13), I obtain values much closer to the measured ones, typically within a few percent. These values are presented in Table 4.2 denoted with $\Delta a_{\rm corr}$.

I apply the same reasoning to the PE and PF simulations, assuming now that the $L_{\rm gas}$ brought by the accreted gas is perpendicular to $L_{\rm bin}$, and thus does not change

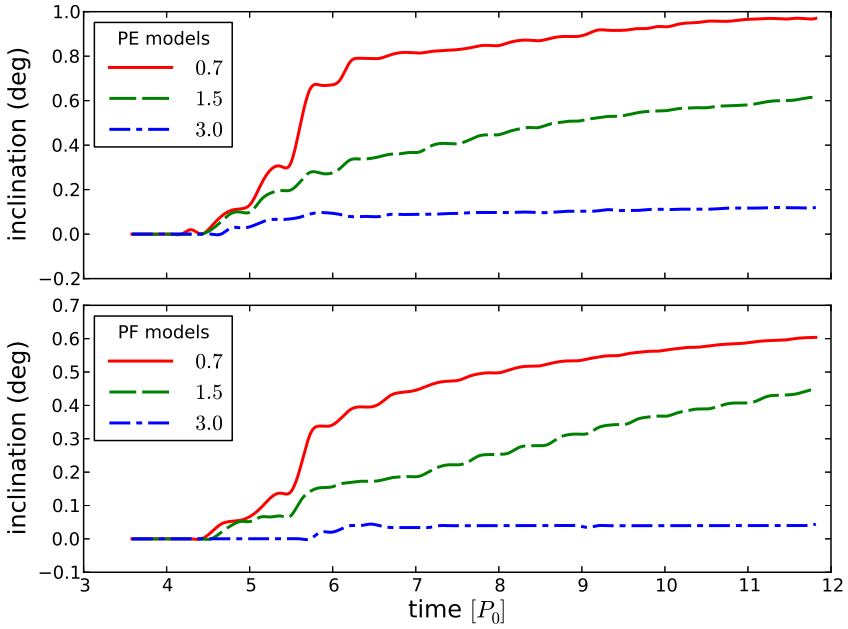

FIGURE 4.5: Evolution of the binary inclination with respect to its initial orientation for the perpendicular models, edge-on (upper panel) and face-on (lower panel). The colours represent the different impact parameters, as indicated in the legend.

its magnitude but only its direction. Therefore

$$0 \approx \frac{3}{2}\frac{\Delta M}{M} + \frac{1}{2}\frac{\Delta a}{a}, \tag{4.18}$$

simply meaning

$$\frac{\Delta a}{a} = -3\frac{\Delta M}{M} \tag{4.19}$$

regardless of the impact parameter. The estimations for the semimajor axis evolution in the perpendicular models are shown in Table 4.3. These numbers show that with this simple model I underestimate the evolution. A likely reason is that the binary slingshots away some of the non-accreted material, preferentially in its direction of motion. The gas therefore takes away further angular momentum from the binary increasing the shrinking which is not included with these simplifications. This effect increases with the impact parameter, as less mass is accreted and much of it is subject to this slingshot. To compute the angular momentum taken away by the remaining gas, I use the fact that the angular momentum magnitude does change in the perpendicular configurations (see Fig. 4.1). I assume that this total change comes from the slingshot. Similar to what I did in the A and CA models, I include this $\Delta L_{\rm out}$ in the LHS of equation (4.18) to estimate the corrected semimajor axis evolution. I show these estimations in Table 4.3. Note the remarkable accuracy with which it is possible to reproduce the measured values from the simulations, with differences no larger than 2%.

In summary, as for the angular momentum evolution, with the analytical model considering only the accreted particles I am able to reproduce the trends of the semimajor axis evolution for all configurations. All the discrepancies found with respect to the simulated values are consistent with the simplifications imposed. When I implement the effect of the non-accreted material and the appropriate

angular momentum budget of the accreted counterparts, I can reproduce the values with much better accuracy.

Caveat: outflows

The peak accretion rates found in these simulations, when scaled to physical units, are usually highly super-Eddington. In the previous chapter, I found that the accretion rates vary between $\approx 1 - 50\,\dot{M}_{\rm edd}$ for a $10^6 M_\odot$ binary during the prompt accretion phase. Naturally this will depend on the orbital configuration, with the smaller impact parameters having the highest peaks, but typically the accretion rates will be super-Eddington during the first few orbits. Certainly the material could be accreted through a slim disc (e.g., Abramowicz et al., 1988). However, taking the conservative approach that accretion is capped to the Eddington rate, the rest of the material will likely be ejected by radiation-pressure driven outflows (e.g., King and Pounds, 2003). Therefore, part (possibly most) of the material which is accreted in the simulation, will be instead ejected in an outflow, making the description of the dynamics inaccurate. To estimate how much this can affect the SMBHB dynamics I take for simplicity the (reasonable) working hypothesis of an isotropic outflow *in each of the BHs' reference frames*. It is easy to show that if a mass $\Delta M_{\rm out}$ is ejected, the angular momentum loss for the binary (assumed to be equal mass, circular) is $\Delta L_{\rm out} = (\Delta M_{\rm out}/4)\sqrt{GMa}$, that can be also written as $\Delta L_{\rm out}/L = \Delta M_{\rm out}/M$. This is the same as in equation (4.7), with $\alpha = 0.25$. So even if all the captured mass is ejected in an outflow instead of being accreted, this amounts to including a factor 0.25 into the parenthesis of equation (4.17), which does not change the evolution significantly. For the PE and PF cases, equation (4.19) becomes $\Delta a/a = -2\Delta M/M$, i.e. the shrinkage of a is 33% less. Hence, even if all the captured mass is ejected in an outflow instead of being accreted, the evolution of the semimajor axis is only mildly affected. This is confirmed by the results shown in Appendix A, where I re-simulate the A0.7 model with different accretion radii. By shrinking the accretion radius by a factor of eight, the mass accretion decreases by about 25%, however there seems to be no correlation with the semimajor axis evolution. This is particularly true for all runs with $r_{\rm sink} \leq 0.1$, for which the binary evolution is essentially identical. This is because the relevant exchange of angular momentum occurred during the capture of the material, which is quite well resolved, instead of the accretion itself.

Finally, radiation driven outflows can also affect the dynamics of the rest of the infalling cloud, inhibiting further accretion, but I cannot quantify this possible effect with the current approach.

4.4 Application: long term evolution of binaries via accretion of incoherent gas clouds

I explore in this section the implications of the results for an evolutionary scenario in which a SMBHB interacts with a sequence of gas clouds. In Fig. 4.6 I show the total change of the binary semimajor axis as a function of the cloud's pericentre distance. From this figure the different behaviour of Δa for the Aligned orientation is clear, still increasing for $r_{\rm p} = 1.5a$, in contrast to the other inclinations for which the total shrinkage is approaching zero at that point. This stems from the larger capture cross-section of each SMBH in corotating encounters due to the smaller velocity

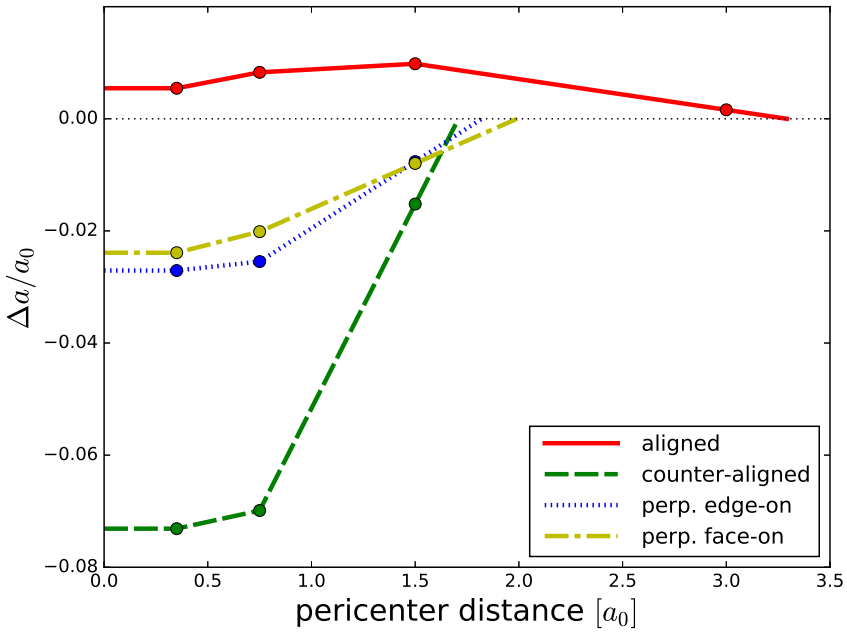

FIGURE 4.6: Total change of the binary semimajor axis as a function of the cloud's pericentre distance. The filled circles are the values measured from the simulations, while the lines are the linear interpolation/extrapolation of those points. The extrapolation after the largest impact parameters define the maximum value of the pericentre distance for the different inclinations, where the evolution of the semimajor axis is zero (dotted black line). For smaller values than $0.35a$ I assume that the relative change of semi-major axis per event remains constant.

relative to the gas particles. This is why I run an additional simulation (A6.0) in the aligned case, as mentioned in Section 4.1.

Using the information shown in Fig. 4.6 I construct a simple model for the evolution of a SMBHB accreting clouds from different directions and with different impact parameters. If I assume a distribution of similar clouds, as the SMBHB semimajor axis changes, the relative size of the cloud increases with respect to the SMBHB. Therefore, my extrapolation is based on the ansatz that the important quantity is the total angular momentum of the cloud (i.e., its impact parameter) and not the spread around the mean (i.e., the relative size of the cloud). This is not necessarily true when the binary becomes more compact because then the size of the cloud with respect to it becomes bigger. However, this approximation is more accurate when the gravitational focusing of the gas is important, e.g. when the cooling is efficient.

4.4.1 Monte Carlo evolution

In order to compute the evolution of a binary I need to determine the orbital parameters of the approaching clouds. For a uniform number density, clouds approach the SMBHB with an impact parameter b following a distribution with a probability density given by $P(b) \propto b\,\mathrm{d}b$, i.e. increasing with the geometrical cross-section. I can use gravitational focusing to link the impact parameter with the

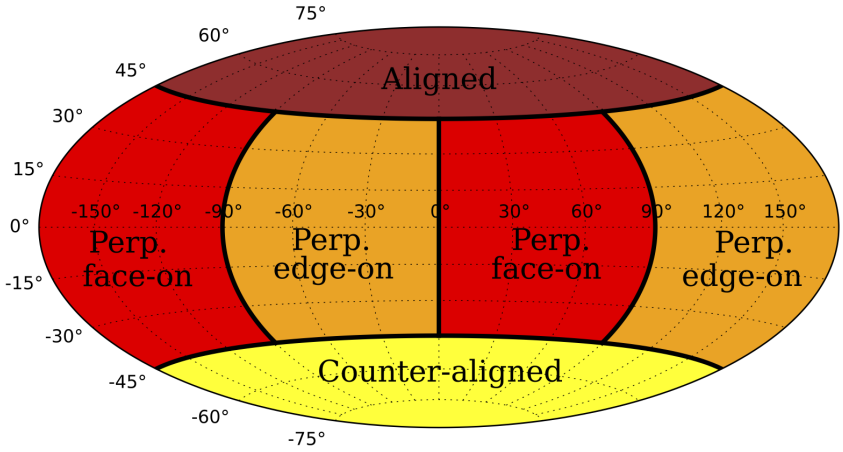

FIGURE 4.7: Map of the four zones I define in the angular momentum direction distribution to determine the relative inclination of the cloud orbit with respect to the binary.

pericenter distance ($r_{\rm p}$) as follows:

$$r_{\rm p} = \frac{v_\infty^2}{2GM_{\rm c}} b^2, \tag{4.20}$$

where I used the fact that the binary is significantly more massive than the individual clouds ($M_{\rm c} \ll M$). Differentiating this expression I obtain $\mathrm{d}r_{\rm p} \propto b\,\mathrm{d}b$, or simply $P(r_{\rm p}) \propto \mathrm{d}r_{\rm p}$, which means that the pericentre distance is distributed uniformly between zero and some maximum value. I compute this maximum value for each inclination using the extrapolation shown in Fig. 4.6.

The impact parameter defines only the magnitude of the cloud angular momentum, not its direction. The cloud angular momentum ($\boldsymbol{L}_{\rm c}$) will point in some direction in the 2D sphere. I need to map this sphere into the four relative orientations I modelled (A, CA, PE and PF). I do so by dividing the 2D sphere in 4 different zones, each assigned to one of the orientations simulated (Fig. 4.7). If θ is the angle between $\boldsymbol{L}_{\rm c}$ and $\boldsymbol{L}$ (with $\boldsymbol{L}$ being the SMBHB angular momentum), I assign to the Aligned encounters the 2D region enclosed in $45° < \theta < 90°$. Similarly, Counter-aligned events correspond to the region defined by $-45° > \theta > -90°$. The rest of the sphere maps into perpendicular encounters. In order to separate between edge-on and face-on, noting that by fixing $\boldsymbol{L}_{\rm c}$ I am still free to rotate the orbit by an azimuthal angle. Let O be the origin of the coordinate system (corresponding to the binary CoM) and $\hat{x}$ a unit vector along the two planes defined by the SMBHB and the cloud orbits. If $r_{\rm p}$ is the periapsis of the cloud orbit, the angle ϕ defined by $\hat{x} - O - r_{\rm p}$ can be used to discriminate between edge-on (PE) and face-on (PF) encounters. If $45° < \phi < 135°$ or $225° < \phi < 315°$, then the encounter is PF, otherwise it is PE. This translates into perpendicular encounters being evenly distributed between PE and PF, as schematically represented in Fig. 4.7. Furthermore, Fig. 4.6 shows that the difference between PE and PF is minimal in terms of semimajor axis evolution. In practice, with this procedure I am assigning a fixed probability to each of the four inclinations. This will be given by the fraction of the solid angle that the zone subtends in the sky of the binary.

With the mapping in hand, I just need to determine the distribution of $\boldsymbol{L}_{\rm c}$. I set the z axis such that $\boldsymbol{L} = (0, 0, L_z)$, with $L_z > 0$, and define F to be the fraction of events with $L_{{\rm c},z} < 0$. Therefore, following Dotti et al. (2013), F represents the

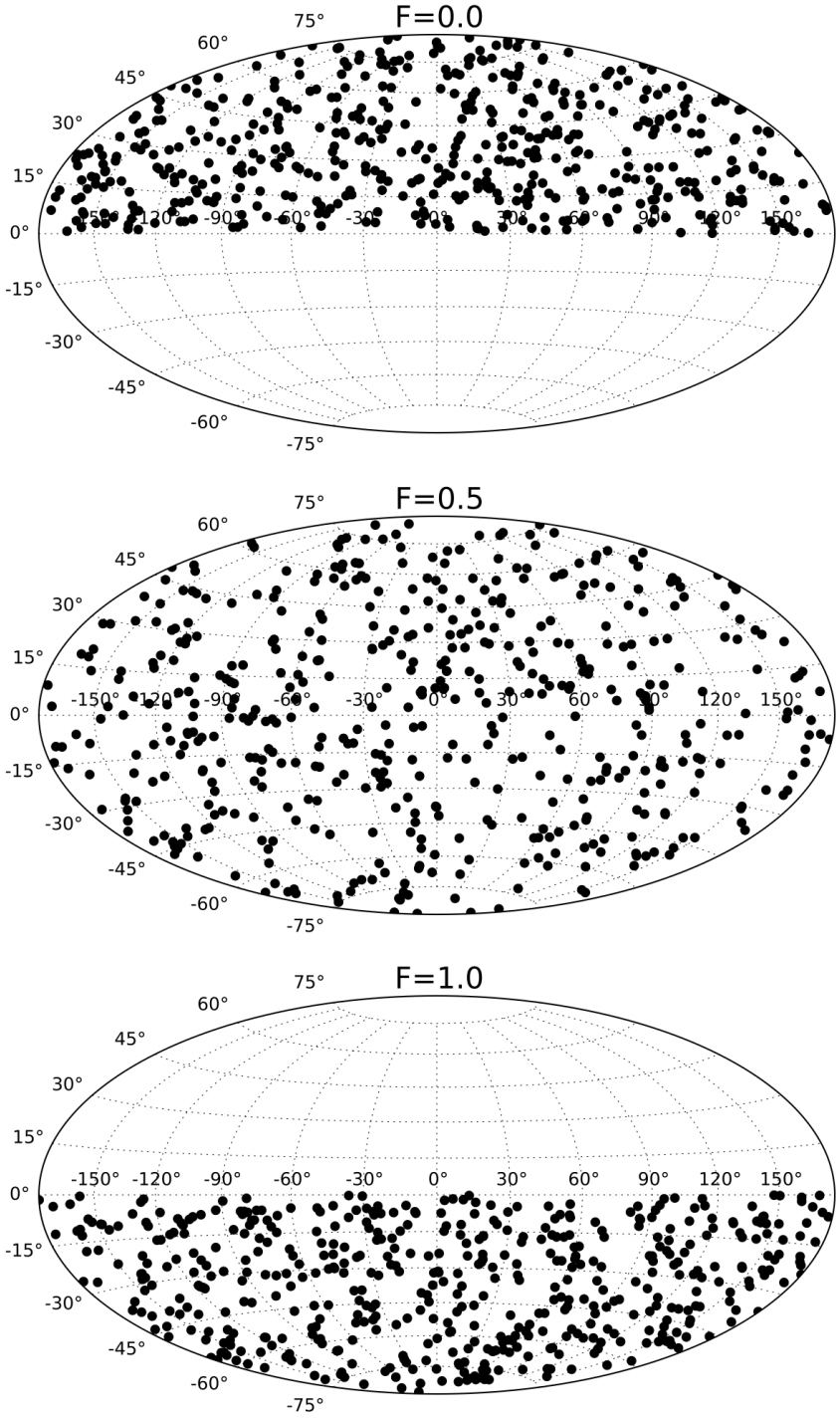

FIGURE 4.8: Realisations of cloud angular momenta distributions for the different adopted values of F, as indicated at the top of each projection. The number F represents the probability of having events in the 'southern hemisphere'. The model $F = 0.5$ is usually referred to as 'chaotic accretion', where portions of gas are accreted from uniformly distributed directions around a SMBH, while for $F = 0.0$ all accretion events are prograde, and for $F = 1.0$ they are retrograde. Figure adapted from Dotti et al. (2013).

probability of having clouds coming from the southern hemisphere, where the northern hemisphere is defined by the direction of the z axis (see Fig. 4.8). Besides the constraint imposed by F, the events are assumed to be isotropic. Therefore, when $F = 0.5$ the events are uniformly distributed over the whole sphere around the binary (known as 'chaotic accretion', King and Pringle, 2006), while for $F = 0.0$ and $F = 1.0$ the events are uniformly distributed over the northern and southern hemisphere, respectively. Note, however that these latter cases are different from coherent aligned/anti-aligned accretion, which would imply all $\boldsymbol{L}_{\rm c}$ along the z axis. Sesana et al. (2014) linked these distributions to the morphological and kinematical properties of the host galaxies in order to explain the spin measurements of SMBHs. Disc galaxies, where the gas dynamics is dominated by rotational velocity, will produce mainly coherent accretion events (prograde or retrograde depending on the binary orientation); while bulge galaxies, dominated by velocity dispersion, will tend to produce more uniformly distributed events.

Finally, using the distributions described above, I generate Monte Carlo populations of clouds with different levels of anisotropy (i.e., different F values) interacting with the binary and evolving its semimajor axis according to their pericentre distance and relative orientation, as given by the curves shown in Fig. 4.6. The results of these models are shown in Fig. 4.9. In order to erase the stochasticity of a single run, each line is the average of 1000 Monte Carlo realisations. On the left panel I show the evolution of the semimajor axis as a function of the number of encounters for the different distributions. To translate this into a temporal evolution I set an initial rate (Γ_0) at which the clouds will interact with the binary. As the binary shrinks the encounters will be less frequent because of the decrease on the binary cross section. This effect can be simulated by adapting the timescale at each encounter as

$$\Delta T = \Gamma_0^{-1} \left(\frac{a_0}{a} \right), \tag{4.21}$$

which becomes longer as the semimajor axis decreases. Using this characteristic timescale I draw the clouds from a Poisson distribution. On the right panels of Fig. 4.9 I show the results obtained for the evolution of the semimajor axis as a function of time for the different distributions.

So far, I have not included in my description the growth of the SMBHB mass. However, in order to evolve significantly its semimajor axis, the SMBHB needs to interact with at least a few hundred gas clouds (see thin lines in the upper left panel of Fig. 4.9), which, in the long run, will imply an accreted mass comparable to the binary initial mass. I therefore need to include mass accretion in these models. The net effect will be a slowdown of the shrinking process: by adding mass to the binary, the mass ratio of the interacting clouds to the SMBHB decreases, meaning that each accretion episode becomes progressively less effective in affecting the binary orbital elements. I therefore include the accreted mass onto the binary after each encounter as follows. Using the same method I used to evolve the semimajor axis, I compute the total mass change according to each cloud's pericentre distance and relative orientation, as given by the values measured from the simulations and their extrapolation. Therefore, each accretion episode causes a change in both the SMBHB semimajor axis and its total mass. In Fig. 4.9 I show the evolution of the SMBHB both when the mass growth is ignored (thin lines) and when it is properly taken into account (thick lines). As expected, the evolution of the binary orbit slows down in the latter case.

It is important to mention that even though perpendicular encounters change the

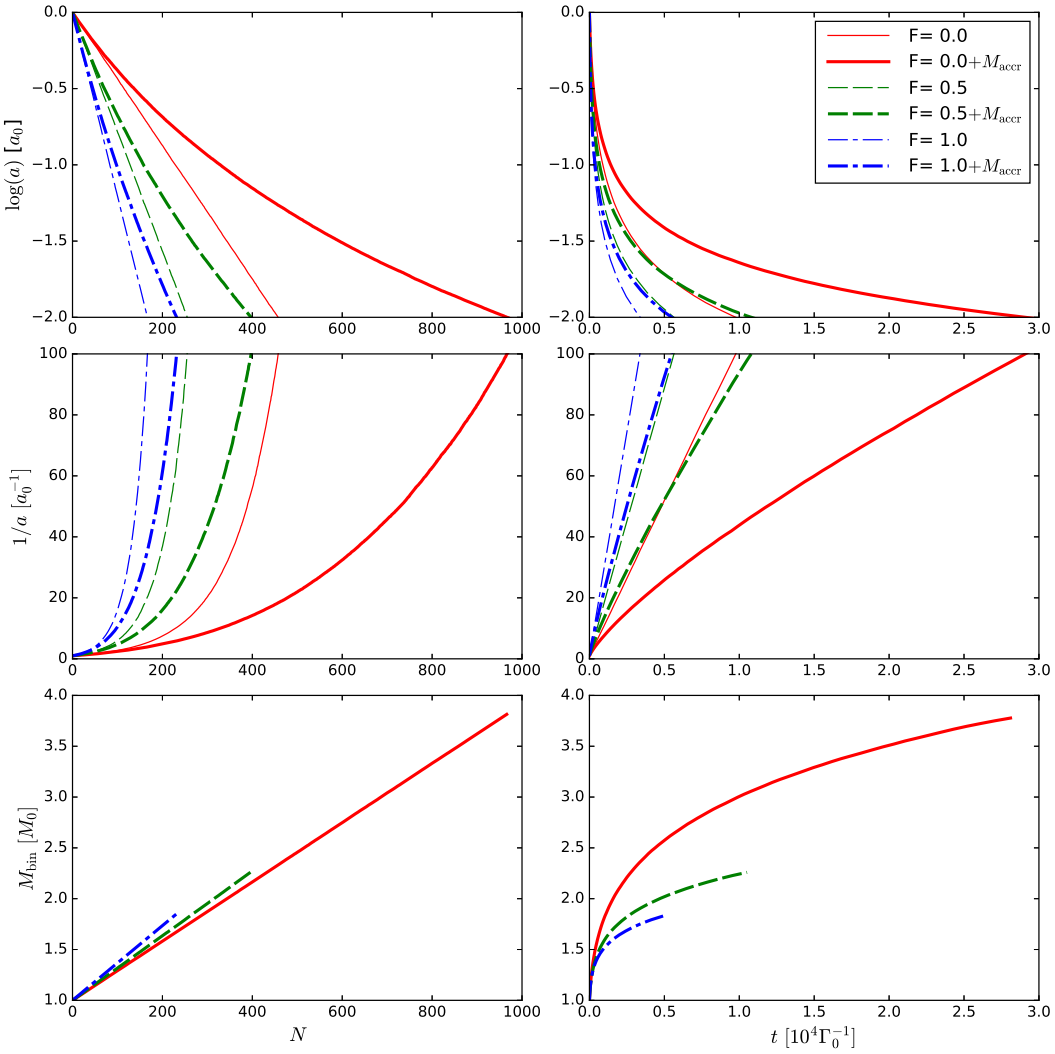

FIGURE 4.9: Evolution of the binary as a function of the number of cloud encounters (left column) and as a function of time (right column). From top to bottom: semimajor axis, inverse of the semimajor axis, and binary mass. The different lines represent models with different distributions of clouds. The thick lines show models that consider the evolution of the binary mass, while the thin lines correspond to models that do not consider this evolution. Each line is the result of averaging 1000 different Monte Carlo runs.

SMBHB inclination angle (see Fig. 4.5), I do not consider this effect in the evolution of the binary angular momentum. Due to the symmetry in the azimuthal angle of all the distributions used, the net evolution of the binary orientation will be roughly zero after a significant number of interactions.

4.4.2 Analytical model

The results of the Monte Carlo runs can be used to calibrate a simple analytical model for the evolution of the SMBHB. In general, this can be written as

$$\frac{\mathrm{d}a}{\mathrm{d}t} = \Gamma \Delta a, \tag{4.22}$$

where Γ is the rate at which clouds are supplied to the binary and Δa is the average relative change in semimajor axis caused by each cloud. Assuming a uniform density distribution of clouds n, travelling at an average speed v, one can write

$$\Gamma = n\Sigma v = n\pi b^2 v = 2\pi n \frac{GM}{v}(\chi a) = \Gamma_0 \frac{a}{a_0}, \tag{4.23}$$

where I defined $\Gamma_0 = 2\pi n(\chi a_0)GM/v$. Here I used the fact that the geometric cross section is $\Sigma = \pi b^2$. Since $M_c \ll M$, encounters are gravitational focusing dominated, and the impact parameter b is related to the maximum approach r_p through $b^2 = 2GMr_\mathrm{p}/v^2$. I consider encounters with a maximum approach $r_\mathrm{p,M} = \chi a$ ($\chi = 3$ in my experiment). On the other hand, I showed in Section 4.2.1 that $\Delta a \propto \Delta M$, where ΔM is the mass accreted by the SMBHB. I can therefore write

$$\Delta a = -\eta\delta \frac{M_c}{M} a, \tag{4.24}$$

where δ represent the average mass fraction of the cloud captured (and eventually accreted) by the binary, and η is an average efficiency coefficient. In each individual encounter, both parameters depend on the cloud inclination and impact parameter, but I am concerned here with finding their average values only. As shown in Chapter 3, for $r_\mathrm{p} < 3a$ I have $\delta \approx 0.3$ (averaged over impact parameters), with little dependence on the cloud–SMBHB orientation. Conversely, the angular momentum transfer efficiency strongly depends on the SMBHB–cloud orientation, as shown by Equations (4.17) and (4.19). Therefore the exact value of η will depend on the level of anisotropy of the cloud distribution.

In the interaction process, the binary also gains mass at the same rate defined by equation (4.23), so that the evolution of the system is given by the coupled linear differential equations:

$$\begin{cases} \frac{\mathrm{d}a}{\mathrm{d}t} = -\eta\delta M_c \frac{\Gamma_0}{a_0}\frac{a^2}{M} \\ \frac{\mathrm{d}M}{\mathrm{d}t} = \delta M_c \frac{\Gamma_0}{a_0} a \end{cases}, \tag{4.25}$$

which combined trivially give the evolution of semimajor axis with mass

$$\frac{\mathrm{d}a}{\mathrm{d}M} = -\eta \frac{a}{M}, \tag{4.26}$$

which is immediately solved to get

$$M_f = M_0 \exp\left\{-\frac{1}{\eta}\ln\left(\frac{a_f}{a_0}\right)\right\}. \tag{4.27}$$

The analytical evolution described by the system of equations (4.25) depends on the values of η and δ, that can be calibrated to match the results of the Monte Carlo runs shown in Fig. 4.9. By doing so, I obtain $(\delta, \eta) = (0.29, 3.45), (0.31, 5.6), (0.36, 7.4)$ for $F = 0.0, 0.5, 1.0$ respectively. I also note that by setting $\mathrm{d}M\,/\,\mathrm{d}t = 0$ (i.e., the gas is not eventually accreted by the SMBHB), the system evolution is analogue to that of a SMBHB scattering intervening stars from a uniform distribution. This is because the underlying physical description is the same: individual objects drawn from some uniform distribution transfer an amount of energy and angular momentum which is dictated by the binding energy of the binary. A major difference, however, resides in the fact that in the cloud case, the SMBHB shrinking is mainly due to absorption of angular momentum from the accreted portion of the cloud, which is a strong function of the incoming cloud direction. Therefore, prograde and retrograde encounters result in different SMBHB shrinking rates, and the evolution of the binary semimajor axis depends on the level of anisotropy of the cloud distribution. This is not true in the stellar scattering case, where the SMBHB shrinking is mostly due to binding energy taken away by each scattered star which, contrary to the angular momentum exchange, is insensitive to its incoming direction. The net result is that in the stellar case, for different levels of anisotropy of the interacting stellar distribution, the binary semimajor axis evolution is the same but the eccentricity evolution is extremely different, as demonstrated in Sesana, Gualandris, and Dotti (2011).

4.4.3 Scaling to astrophysical systems

To study the final fate of the binary, I introduce in equation (4.25) the GW emission term (Peters and Mathews, 1963), to get

$$\begin{cases} \frac{\mathrm{d}a}{\mathrm{d}t} = -\eta\delta M_{\mathrm{c}} \frac{\Gamma_0}{a_0} \frac{a^2}{M} - \frac{64}{5} \frac{G^3}{c^5} \frac{M^3}{4a^3} \\ \frac{\mathrm{d}M}{\mathrm{d}t} = \delta M_{\mathrm{c}} \frac{\Gamma_0}{a_0} a \end{cases} \tag{4.28}$$

where I assumed circular binaries and $M_1 = M_2 = M/2$ throughout the process (i.e. I assume each individual SMBH gets the same share of accretion). The interaction rate is connected to the physical properties of the system via $\Gamma_0 = 2\pi n(\chi a_0) GM/v$. One can either specify the cloud number density n and infall velocity v, or assume a certain gas mass inflow rate $\dot{M}_{\mathrm{g}}$. As an example, I take two Milky Way like SMBHs, $M_1 = M_2 = M/2 = 5 \times 10^6\,\mathrm{M}_\odot$, at 0.5 pc semimajor axis (roughly corresponding to the hardening radius $a_{\mathrm{h}} \approx GM/(4\sigma^2)$ for a Milky Way galaxy), with a mass inflow rate $\dot{M}_{\mathrm{g}}$ of either $1\,\mathrm{M}_\odot\mathrm{yr}^{-1}$ or $10\,\mathrm{M}_\odot\mathrm{yr}^{-1}$, corresponding to $\Gamma_0 = 10^{-5}\mathrm{yr}^{-1}$ or $\Gamma_0 = 10^{-4}\mathrm{yr}^{-1}$ (the cloud mass is $M_{\mathrm{c}} = 0.01M = 10^5\,\mathrm{M}_\odot$ for $M = 10^7\,\mathrm{M}_\odot$). Such inflow rates might be typical in the central regions of relatively gas-rich post-merger galaxies.

Results are shown in Fig. 4.10, both for the binary shrinking and the mass growth. The SMBHB coalesce within ≈1 Gyr and ≈0.2 Gyr for the two gas inflow rates assumed. The degree of anisotropy of the gas inflow has only a mild impact on the evolution of the system, affecting the coalescence timescale by a factor of ≈ 2. More relevant is the impact on the mass growth. While in the $F = 1.0$ case the SMBHB barely doubles its mass, the mass growth is almost an e-fold larger in the $F = 0.0$ case. This is because the prograde cloud distribution is less efficient ($\eta \approx 3.5$) than a retrograde one ($\eta \approx 7$) in shrinking the SMBHB, and consequently the process requires more accreted mass.

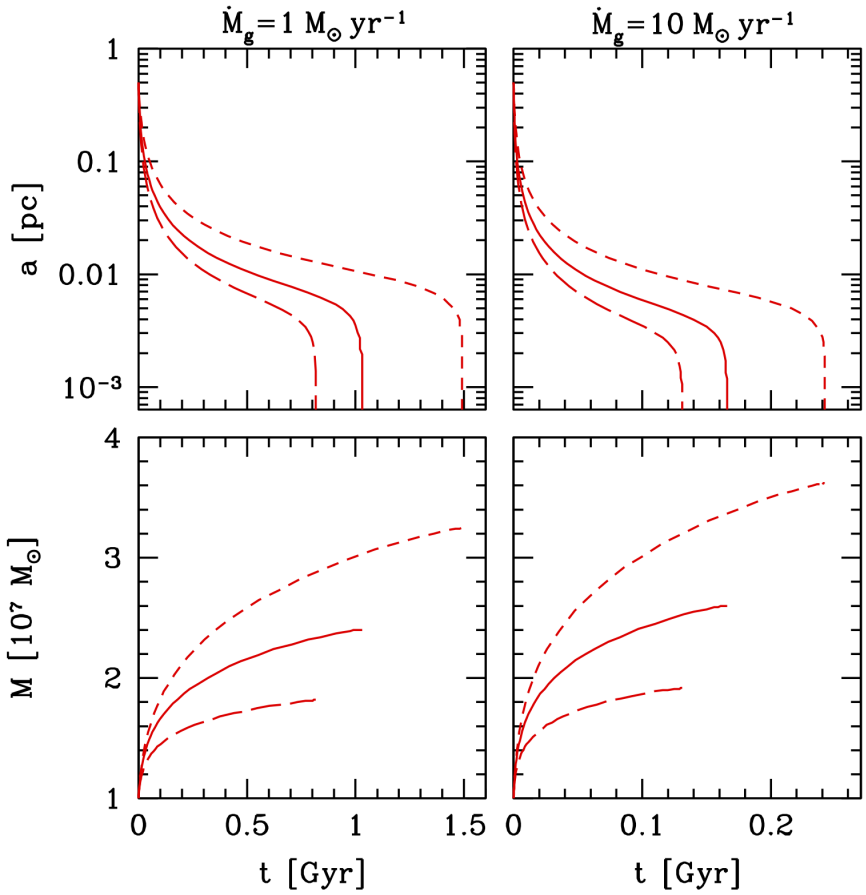

FIGURE 4.10: Evolution of a binary with $M_1 = M_2 = 5 \times 10^6\,\mathrm{M}_\odot$ as a function of time for two different gas inflow rates as indicated at the top of the figure. The top panels show the semimajor axis evolution, while the bottom panel show the SMBHB mass evolution. Long–dashed, solid and short–dashed curves are for $F = 1.0,\ 0.5,\ 0.0$ respectively. The late, fast evolution of the semimajor axes is driven by the emission of gravitational waves.

4.4.4 Robustness of the model

The model described above is subject to limitations arising from some of my simplifying assumptions. In this subsection, I explore the extent that some of these assumptions have on the results I present.

Discrete orientations

I am collapsing the parameter space of the cloud angular momentum direction into four selected configurations (A, CA, PF, PE), with rather arbitrary boundaries. Most of the events given by any of the F values I am using will be neither exactly parallel (aligned or counter-aligned) nor perpendicular (edge or face on) to the SMBHB, so this approximation is bound to introduce some error in the estimate of the binary evolution. In particular, it would be important to simulate the infall of clouds with $\boldsymbol{L}_{\rm c}$ partially aligned to $\boldsymbol{L}$, since here lies the separation between events leading to shrinking (perpendicular) and expanding (aligned) SMBHBs. In order to observe the transition between these two regimes I would need to cover that parameter range with a series of simulations, which is unfortunately not feasible with my current computational capabilities.

Nevertheless, I can roughly estimate the uncertainty of the long-term model by using different functions to interpolate between the values obtained with the simulations. As I discuss in Section 4.3, for the parallel orbits (A and CA models) a fraction of the cloud's initial angular momentum is directly added to the binary. Hence, for an arbitrarily inclined orbit, I expect that the main contribution comes from the projection of the gas velocity onto the binary plane. I propose the following function that captures this behaviour

$$\left(\frac{\Delta a}{a}\right)_{\rm tot} = \left(\frac{\Delta a}{a}\right)_{\parallel} \cos\beta + \left(\frac{\Delta a}{a}\right)_{\perp} \sin\beta, \tag{4.29}$$

where I define the subscripts as

$$\parallel = \begin{cases} \text{A} & \text{if} \quad 0^\circ < \theta < 90^\circ \\ \text{CA} & \text{if} \quad -90^\circ < \theta < 0^\circ \end{cases}, \tag{4.30}$$

$$\perp = \begin{cases} \text{PE} & \text{if} \quad 0^\circ < \phi < 90^\circ \text{ or } -180^\circ < \phi < -90^\circ \\ \text{PF} & \text{if} \quad 90^\circ < \phi < 180^\circ \text{ or } -90^\circ < \phi < 0^\circ \end{cases}, \tag{4.31}$$

and the angle β as

$$\beta = \begin{cases} \theta & \text{if} \quad 0^\circ < \theta < 90^\circ \\ \theta + 90^\circ & \text{if} \quad -90^\circ < \theta < 0^\circ \end{cases}. \tag{4.32}$$

While conceptually simple, the main disadvantage of equation (4.29) is that it does not reproduce a scenario where both parallel and perpendicular changes are equal. In consequence, I propose an alternative form that takes into account this fact,

$$\left(\frac{\Delta a}{a}\right)_{\rm tot} = \left(\frac{\Delta a}{a}\right)_{\parallel} \cos^2\beta + \left(\frac{\Delta a}{a}\right)_{\perp} \sin^2\beta, \tag{4.33}$$

where I use the same definitions described above.

I refer to these two equations (Eqs. 4.29 and 4.33) as 'Continuous model 1' and 'Continuous model 2', respectively. Despite the rather arbitrary nature of these

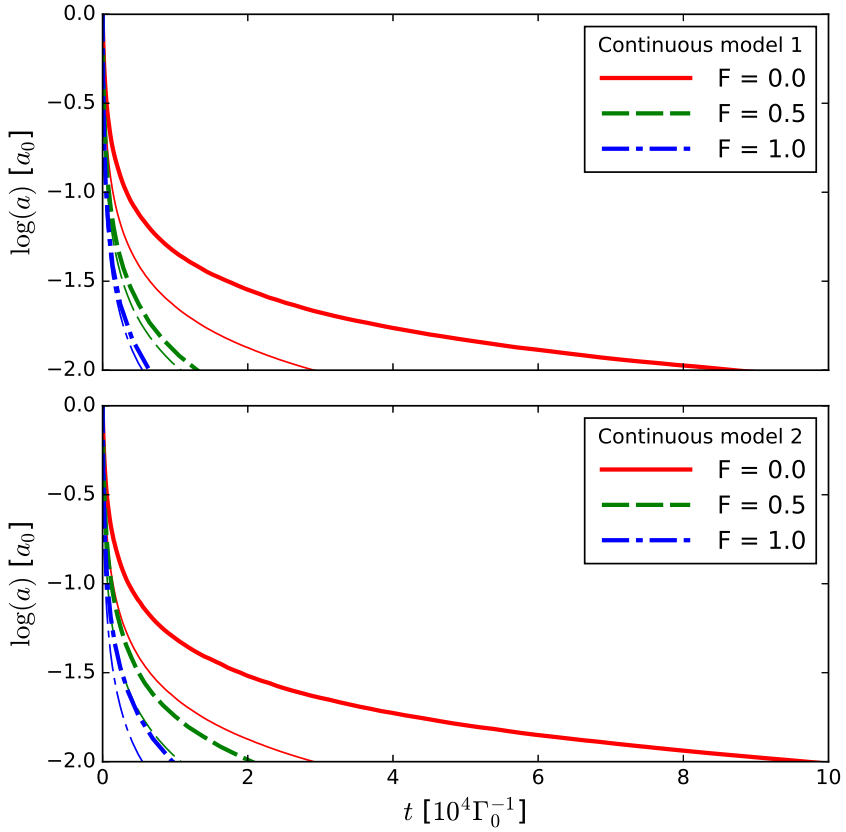

FIGURE 4.11: Evolution of the binary semimajor axis as a function of time, computed with Monte Carlo runs. The different lines represent models with different distributions of clouds as indicated in the legend. The upper panel shows the result using equation (4.29), while the lower panel corresponds to equation (4.33). Both new models are depicted with thick lines, while the thin lines represent the original runs using the discrete orientations.

interpolations, I expect they, together with the discrete model presented in § 4.4.1, illustrate a reasonable range of possible evolutions for the binary population. I show the results obtained with the two models in Fig. 4.11. I find that the timescale to reach the GW regime somewhat increases compared with the discrete scenario (Fig. 4.9). This occurs because the aligned configuration has a maximum impact parameter larger than the others (see Fig. 4.6), which means that an important fraction of the events would only expand the binary. In fact, the evolution timescale increases by ≈ 3 in the $F = 0.0$ scenario, but only by a factor $\lesssim 2$ in all other cases. Although highlighting the uncertainties related to the model, these tests essentially confirm the basic SMBHB evolution scenario.

Effects of the non-accreted material

I am considering a sequence of cloud infall events, treating them separately from each other. In fact, a fraction of the cloud is not accreted by the binary, forming circumbinary structures. As more clouds interact with the binary, those left-over structures can accumulate and give rise to a massive envelope (either a circumbinary cloud or a massive circumbinary disc) that can efficiently extract the binary angular momentum, overall making the shrinking process faster. For example, the prograde encounters tend to expand the SMBHB, because only the angular momentum transfer in the initial encounter is relevant, and the mass of the leftover circumbinary disc is negligible. However, following many such events, a massive circumbinary disc will eventually form. This type of structure has been shown to be efficient in transporting angular momentum outwards and shrinking the binary.

As shown by Nixon, King, and Pringle (2011), randomly-oriented events around a circular binary can produce external discs that efficiently either align or anti-align with the binary due to differential precession and dissipation within the disc. Consequently, I expect that some of the non-accreted material will result in coplanar circumbinary discs, either prograde or retrograde with respect to the binary. The condition for counter-alignment is

$$\theta < 0, \quad L_{\rm d} < 2L_{\rm b}, \tag{4.34}$$

where $L_{\rm d}$ and $L_{\rm b}$ are the angular momentum of the disc and the binary, respectively (Nixon et al., 2011; Nixon, King, and Pringle, 2011; Nixon, 2012). Assuming that all of the non-accreted material will form a disc with the original orientation of the cloud, I use eq. (4.5) to estimate its angular momentum. I derive the counter-alignment condition of $\alpha \lesssim 70$ for events coming from the south hemisphere ($\theta < 0$). Given that I am modelling clouds with almost radial orbits and little initial angular momentum ($\alpha \lesssim 2$), I assume that every cloud from the south hemisphere will tend to counter-align, while events from the north hemisphere will always tend to align with the binary. This will be particularly relevant for the $F = 0.0$ and $F = 1.0$ distributions, where the events are somewhat coherent, thus increasing the probability of having a well defined disc.

Cuadra et al. (2009) showed that a binary surrounded by a massive circumbinary disc evolves mostly due to the action of gravitational torques. They find a semimajor axis evolution of $\dot{a}_{\rm circumb} \sim -10^{-5} a_0 \Omega_0$ for a disc with 20% the mass of the binary, with a dependence of the merger timescale on the system parameters that follows $t_{\rm disc} \propto (M_2/M)^{1/2} M^2 \Sigma_0^{-5/2}$ (see eq. 5 from Cuadra et al., 2009). I then scale the

semimajor axis evolution as follows:

$$\dot{a}_{\rm circumb} \sim -10^{-5} a_0 \Omega_0 \left(\frac{M}{M_0}\right)^{-2} \left(\frac{M_{\rm disc}}{0.2 M_0}\right)^{5/2} \left(\frac{a}{a_0}\right)^{-2}, \tag{4.35}$$

where Ω_0 represents the binary initial orbital frequency and $M_{\rm disc}$ the disc mass. Assuming that some of the non-accreted material aligns (or counter-aligns) efficiently, this gas will eventually form a massive, coplanar circumbinary disc. Then, I can use equation (4.35) as a rough estimate of the maximum effect that the non-accreted gas can have on the binary arising from gravitational torques. For the disc mass I adopt the entire non-accreted material after each encounter. Finally, since Roedig and Sesana (2014) showed that, despite substantial differences in the underlying physical processes, the semimajor evolution is similar when the binary is surrounded by a prograde or by a retrograde disc, I use the same expression for $F = 0.0$ and $F = 1.0$.

Alternatively, in the isotropic case ($F = 0.5$) the clouds are highly misaligned with respect to the binary *and* between one another, hence most of the material will not be able to precess enough times to change significantly its inclination before the infall of a new cloud. For instance, recall that in Chapter 3 I derived an alignment timescale of the order of 1000 orbits for a completely perpendicular disc. I therefore expect this gas behaving as independently precessing rings, similar to what occurs when a misaligned circumbinary disc breaks under the gravitational pull of the binary (Nixon, King, and Price, 2013; Aly et al., 2015). In this scenario, the gas interaction causes partial cancellation of angular momentum that sends material plunging to the binary, increasing the accretion rate. Assuming this gas does not bring net angular momentum to the binary, I expect a semimajor axis evolution similar to eq. (4.18), namely,

$$\dot{a}_{\rm cancelled} = -3\dot{M}_{\rm cancelled} \frac{a}{M}, \tag{4.36}$$

where $\dot{M}_{\rm cancelled}$ is the accretion rate onto the binary arising from the plunging material. Since the interaction of these misaligned discs is a highly non-linear process, it requieres direct numerical modelling to establish how much material reaches the SMBHs. Nevertheless, in order to have an order of magnitude estimate I use the fiducial value of $\dot{M} \sim 10^{-7} M_0 \Omega_0$ from Nixon, King, and Price (2013, their Fig. 5), exploiting the similarities with the disc tearing model. To apply this accretion rate in my model I make the reasonable assumption that this quantity will be proportional to the available gas surrounding the binary ($M_{\rm av,gas}$) as follows:

$$\dot{M}_{\rm cancelled} \sim 10^{-7} M_0 \Omega_0 \left(\frac{M_{\rm av,gas}}{10^{-2} M_0}\right). \tag{4.37}$$

Since on average there is 70% of the cloud's mass left after each event, $M_{\rm av,gas}$ will increase with time.

To model the presence of the surrounding gas, I include an additional term $\Delta a = \dot{a}\Delta T$ to the Monte Carlo evolution of the binary explained in § 4.4.1, where ΔT is given by equation (4.21), and $\dot{a}$ by equation (4.35) or (4.36) depending on the distribution. In Fig. 4.12 I show the results obtained with this model. As expected, the SMBHB shrinks faster compared with the original runs due to the action of the surrounding material, where the stronger effect is produced from the presence of the self-gravitating circumbinary disc. The largest difference is observed for the $F = 0.0$

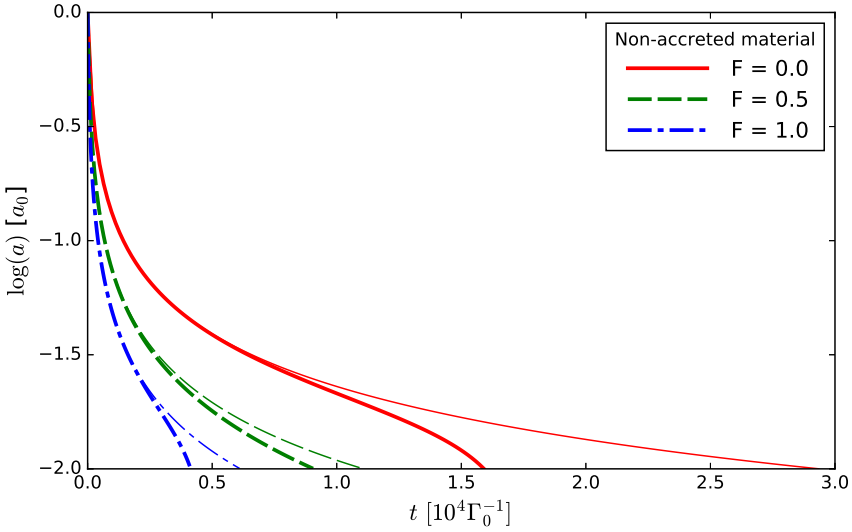

FIGURE 4.12: Evolution of the binary semimajor axis as a function of time, computed with Monte Carlo runs. The thick lines represent the model including the effects of the non-accreted material, while the thin lines show the original runs where the clouds were treated on isolation. For the $F = 0.0$ and $F = 1.0$ distributions I model the presence of a coplanar massive circumbinary disc as an extra source of angular momentum transport, while for $F = 0.5$ I am enhancing the accretion onto the binary due to cancellation of angular momentum in the gas.

distribution, with a decrease of a factor ≈ 2 respect to the standard model.

Chapter 5

Multiple infalling clouds

In the previous chapters I have presented a series of high resolution hydrodynamical simulations of individual gaseous clouds interacting with SMBHBs. Using different orbital configurations of incoming gas, I studied the dynamical response of the binary. Building on these results, I constructed a simple model for evolving a binary interacting with a sequence of clouds, and showed that the binary efficiently evolves down to the GW emission regime within a few hundred million years, overcoming the "final parsec problem". This approach, however, is subject to a number of caveats and limitations. In particular, i) discretising the angular momentum space into just four configurations, which does not take into account intermediate inclinations, and ii) neglecting the non-accreted material that will eventually accumulate, forming circumbinary structures and/or increasing accretion onto the binary.

In this chapter I present the results of a new suite of simulations to study the evolution of a binary embedded in a turbulent environment, where I expect several gaseous clumps to infall and dynamically interact with the binary. The main goal is to overcome these limitations in the binary evolution by numerically modelling the interaction of a SMBHB with a sequence of incoherent accretion events.

5.1 The numerical model

Similar to the simulations presented in the previous chapters, I model the system's evolution using the SPH code GADGET-3, as described in detail in Chapter 2. The numerical setup is based on the single cloud simulations.

While conceptually similar, these new simulations are much more computationally expensive compared with the single cloud models presented in the previous chapters because (i) there is a continuous increase in the number of particles with the addition of new clouds, and (ii) they require a better conservation of angular momentum if one wants to study the binary orbital evolution throughout the whole simulation, especially the much smaller effects of the gas after the prompt phase.

To improve the angular momentum conservation it is necessary to compute the gravitational forces with the smallest error possible. As explained in Chapter 2, GADGET uses the Barnes-Hut tree-algorithm to approximate the gravitational forces, which is the dominant source of numerical noise. In this method, distant particles are grouped together into cells and their contribution to the potential is approximated at the cell centre of mass plus a monopole expansion. For gas particles this is sufficient, as they are well distributed at high N and can be accurately approximated with this method. However, for the two sink particles, this is not good enough, and more accurate gravitational forces are required to

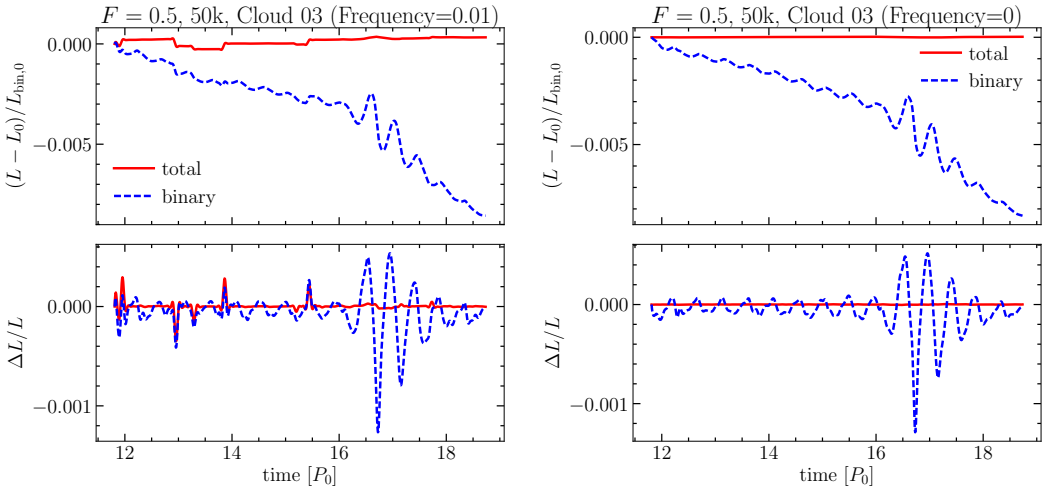

FIGURE 5.1: Angular momentum evolution of one of two simulated systems using different values of the parameter `TreeDomainUpdateFrequency`. The upper plots show the total angular momentum of the system (solid red lines) and the binary (dashed blue lines), and the lower plots show the relative change between snapshots. On the left panel the simulation was performed using a `TreeDomainUpdateFrequency` of 0.01, while on the right panel this parameter is 0. This comparison shows that the source of the spurious jumps displayed on the left panel is the finite frequency of tree reconstruction.

resolve the effect of the gas on their dynamics. To this end, I have modified the code to remove the sink particles from the gravity tree, and their forces are instead summed directly. As this is only done for only two particles in each simulation, the additional computational expense involved is not high.

A more critical modification with respect to the previous simulations is the frequency at which the code makes the domain decomposition and full tree reconstruction. This is determined by the input parameter `TreeDomainUpdateFrequency`. In the single cloud models, the domain was recomputed when at least 1% of the particles were active (`TreeDomainUpdateFrequency` = 0.01), which was sufficient to resolve the transient phase in the single cloud models. However, due to "violent" changes produced by inflow of material from different directions and large accretion, this frequency is not enough to study the dynamical evolution of the multi-cloud scenario, as the spurious changes in the total momentum are also present in the binary. An example of this situation is shown on the left panel of Fig. 5.1, where the numerical noise is producing noticeable jumps in the binary evolution. To decrease the force errors I have set `TreeDomainUpdateFrequency` to zero, forcing the code to reconstruct the tree at *every* time-step. On the right panel of Fig. 5.1 I present the same previous system, simulated using this new feature. While this increases greatly the computational cost of the new models (typically a factor of 10-20), the numerical fluctuations in the total angular momentum have been reduced, allowing a robust study of its dynamical evolution during the phases of the interactions (see §5.2.1 below).

To make these simulations feasible, I have decreased the resolution elements of the individual clouds with respect to the single cloud models. In order to study

the convergence of the binary dynamical evolution with resolution I model the gas clouds using 5×10^4, 2×10^5 and 5×10^5 particles for each cloud, in contrast with the 4×10^6 used before. To identify these different resolutions throughout this chapter I use `50k`, `200k` and `500k`, respectively.

5.1.1 External potential

During the single cloud simulations the system was treated in isolation, i.e with no external forces acting upon it. In reality, such a binary would be placed deep in the potential well of a galaxy where stars and dark matter exert some gravitational influence. To mimic the presence of the galactic spheroid I have included an external potential with a Hernquist profile (Hernquist, 1990) which can be written as

$$\rho(r) = \frac{M_{\rm H}}{2\pi} \frac{r_{\rm H}}{r} \frac{1}{(r + r_{\rm H})^3}, \tag{5.1}$$

and an enclosed mass given by

$$m(r) = M_{\rm H} \frac{r^2}{(r + r_{\rm H})^2}, \tag{5.2}$$

where $M_{\rm H}$ and $r_{\rm H}$ are scaling constants that represent the total mass of the spheroid and the size of core, respectively. Based on a typical $M_{\rm BH} - M_{\rm bulge}$ relation (Magorrian et al., 1998) and a radius-to-stellar-mass relation Dabringhausen, Hilker, and Kroupa (2008), I have chosen $M_{\rm H} = 4.78 \times 10^2 M_0$ and $r_{\rm H} = 3.24 \times 10^2 a_0$, thus implying

$$m(a_0) \approx 0.1 M_0. \tag{5.3}$$

In consequence, this external force represents only a small perturbation at the scales of interest and the dynamics of the system is still dominated by the binary's gravitational potential. Moreover, because this external potential is spherically symmetric, orbits experience precession only, and the energy and angular momentum are conserved. This implies that the oscillations induced by this potential in the binary orbit are not expected to have a secular effect. In practice, this potential maintains the binary close to the centre of the reference frame by applying a restoring force when it drifts away due to the interaction with the incoming material.

For the single cloud simulations this potential was not needed, as drifts produced by the interaction with the cloud or by numerical inaccuracies did not affect the prompt phase studied. For these new models the computation of each cloud's pericentre distance was made *a priori* with the binary centre of mass static at the origin of the cartesian coordinates, thus this restoring force guarantees the values to remain close to those originally calculated.

5.1.2 Initial conditions

The binary consists of two sink particles, initially having equal masses and a circular orbit placed on the $x - y$ plane. The orbit was initialised without taking into account the external potential, thus some small deviations from the circular orbit are expected.

On the other hand, all the clouds are initially spherical with uniform density, a turbulent velocity field, and a total mass 100 times smaller than the binary. And

similar to the single cloud models, the turbulent velocity field is drawn from a random distribution with power spectrum $P_v(k) \propto k^{-4}$. It is worth mentioning that the random seed is exactly the same for all clouds. With these choices all clouds are identical except for their initial orbit, which simplifies the comparison between the different distribution of clouds.

The initial setup of these simulations is motivated by the Monte Carlo models presented in Chapter 4. Namely, I use the F-distributions for the angular momentum orientation (Fig. 4.8), and a flat distribution for the pericentre distances. I have generated a total of 10 clouds with orientations shown in Fig. 5.2 and periapsis shown in Fig. 5.3. The same pericenter distances are used for the 3 different levels of anisotropy F. The maximum value of the pericentre distribution was chosen to be $r_{\rm p,max} = 2a_0$. This value ensures that the incoming clouds will produce a transient evolution with the first impact, independent of the relative inclination (see Fig. 4.6). Finally, the time difference between events exhibited on figure 5.3 was determined by considering a Poisson process with a characteristic timescale of $\Delta T = 5P_0$. For a binary with $M_0 = 10^6 M_\odot$ and $a_0 = 0.2$ pc, this rate of clouds corresponds to a mass inflow of $\approx 1 M_\odot$ yr^{-1} to the central parsec.

In order to make a robust comparison of the dynamical impact of each distribution it is necessary to reduce some of the stochasticity produced by the low number of events. With that goal in mind, the different angular momentum distributions were not sampled independently from each other. Only the angles from the isotropic distribution ($F = 0.5$) are randomly drawn. I then generate the co-rotating distribution ($F = 0.0$) by reflecting symmetrically the negative inclination angles ($\theta < 0°$) with respect to the binary's orbital plane onto the northern hemisphere. The same is done for the counter-rotating clouds ($F = 1.0$), but mirroring the angles $\theta > 0°$ onto the southern hemisphere. The azimuthal angles are kept unchanged. This means that the only distinction between distributions is the inclination angle θ of the cloud's orbits.

Note that by sampling only the initial angular momentum vector (orientation and magnitude), the orbit of each cloud is not fully determined, as a Keplerian trajectory is defined by a total of 6 parameters. Having (θ_ℓ, ϕ_ℓ, r_p), together with the initial distance and speed of the cloud, leaves one degree of freedom, which basically means that I can choose the initial position to be oriented in *any* direction as long as it lies on the plane defined by the unitary vector

$$\hat{\boldsymbol{\ell}} = (\cos\phi_\ell \sin\theta_\ell, \sin\phi_\ell \sin\theta_\ell, \cos\theta_\ell), \tag{5.4}$$

where θ_ℓ and ϕ_ℓ are the polar and azimuthal angles of the angular momentum direction, respectively.

The initial position and velocity vectors are generated by first obtaining an arbitrary unitary vector $\hat{\boldsymbol{e}}$ lying on the aforementioned plane by taking the cross product with the x-axis

$$\hat{\boldsymbol{e}} = \hat{\boldsymbol{\ell}} \times \hat{\boldsymbol{x}}. \tag{5.5}$$

Then I rotate this vector by a random angle β, drawn uniformly between 0 and 2π, using the expression

$$\mathbf{r}' = \hat{\boldsymbol{e}} \cos\beta + (\hat{\boldsymbol{\ell}} \times \hat{\boldsymbol{e}}) \sin\beta. \tag{5.6}$$

This ensures that there is no preferential direction of incoming gas.

On the other hand, the velocity vector also lies on the plane defined by the angular momentum ($\hat{\boldsymbol{\ell}}$), but is rotated by an angle $\theta_{\rm vel}$ with respect to the position

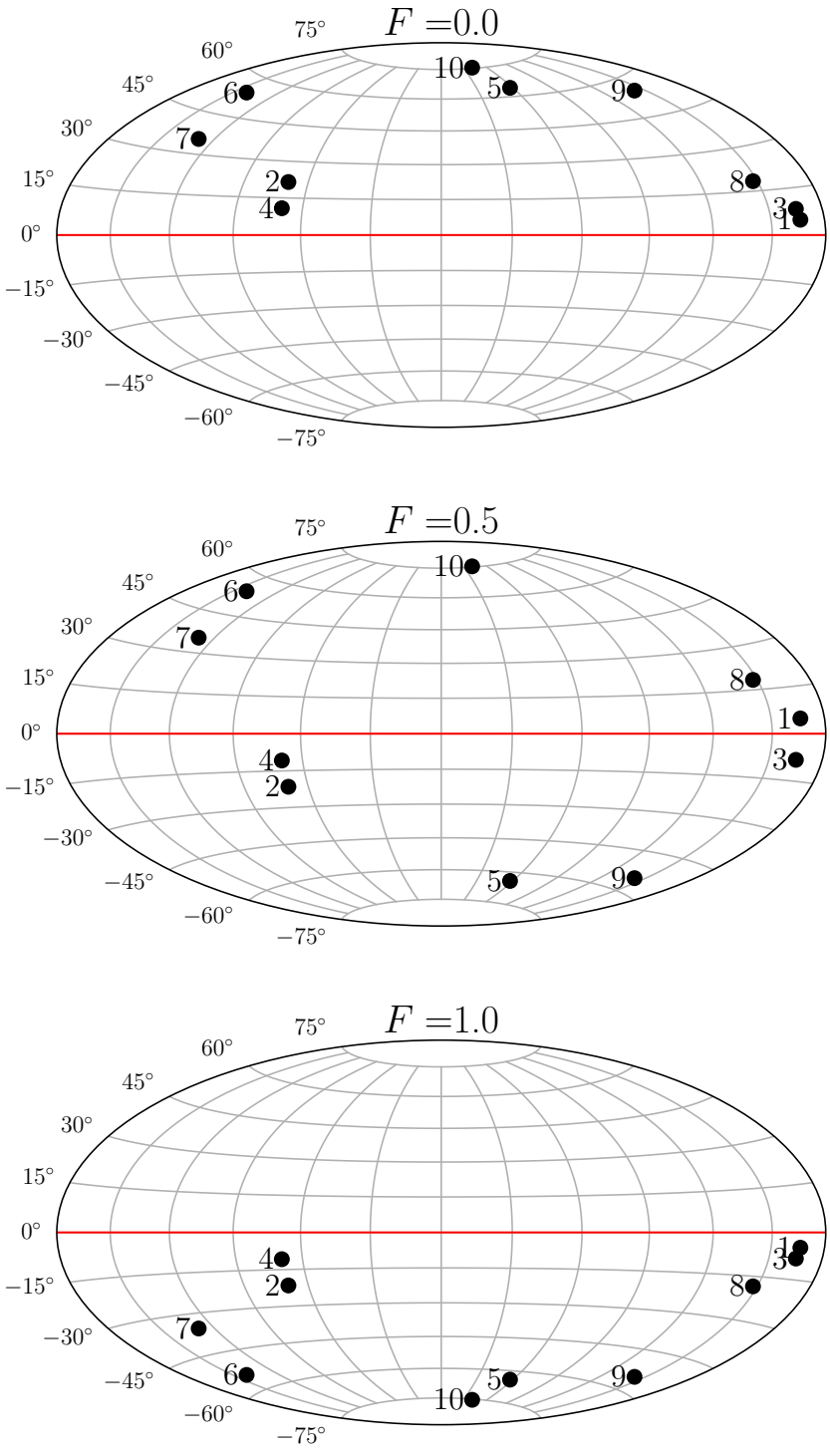

FIGURE 5.2: Angular momentum orientations of the initial orbit for 10 randomly selected clouds from different F distributions, as indicated at the top of each projection. Note that $F = 0.0$ and $F = 1.0$ cloud orbits are generated by mirroring the inclination angle θ from $F = 0.5$ with respect to the binary's orbital plane (red solid line) to swap between one hemisphere to the other. Labelled numbers on each circle indicate the order in which the clouds are introduced.

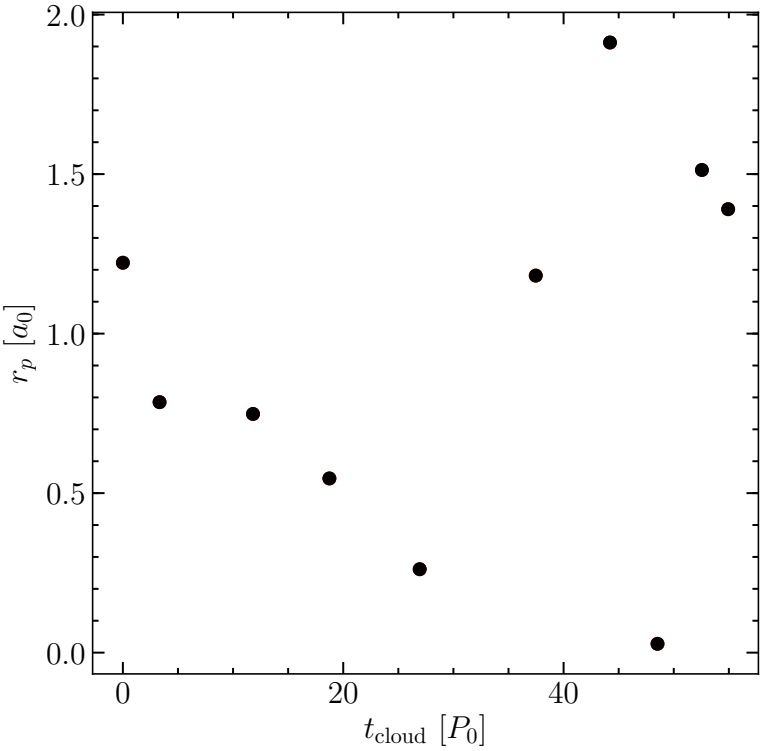

FIGURE 5.3: Distribution of pericentre distances as a function of the time difference between events. This distribution is used for the 3 levels of anisotropy F.

vector and therefore it can be obtained using a similar expression

$$\mathbf{v}' = \hat{\boldsymbol{e}}\cos(\beta - \theta_{\rm vel}) + (\hat{\boldsymbol{\ell}} \times \hat{\boldsymbol{e}})\sin(\beta - \theta_{\rm vel}), \tag{5.7}$$

where β has the same value as used in eq. (5.6). As presented in Chapter 3, $\theta_{\rm vel}$ is directly related to the pericentre distance as follows

$$\theta_{\rm vel} = \arcsin\left(\frac{v_{\rm p}}{v_{\rm ini}}\frac{r_{\rm p}}{d_{\rm ini}}\right), \tag{5.8}$$

where $d_{\rm ini} = 15a$ is the initial distance to the binary centre of mass, $v_{\rm ini} = 0.25\sqrt{GM/a}$ is the initial velocity and $v_{\rm p}$ is the velocity at periapsis.

Finally, I normalise these vectors to the initial distance and velocity,

$$\mathbf{r} = \frac{d_{\rm ini}}{\|\mathbf{r}'\|}\mathbf{r}', \tag{5.9}$$

$$\mathbf{v} = -\frac{v_{\rm ini}}{\|\mathbf{v}'\|}\mathbf{v}', \tag{5.10}$$

which yields the orbit defined by the sampled angular momentum vector. The initial position and velocity vectors of each cloud are displayed in Table 5.1, listed here so that the results can be reproduced by future studies.

All the simulations described in this chapter are run in different "sections". Initially one cloud is placed with the corresponding initial vectors as given by eqs. (5.9) and (5.10). This system is evolved until the time set for the following cloud to enter has been reached, at which point the simulation is stopped. The new cloud is added to the final snapshot to generate the initial conditions for the following section.

5.2 Binary orbital evolution

Given the coarse resolution of the individual clouds, the gaseous structures in these simulations are probably not well sampled, thus the robust study of their formation and evolution is likely not resolved with these models. Nevertheless, I expect the overall dynamics of the system to be only mildly affected by the low resolution because the individual gas particles have nearly ballistic orbits during the infall and subsequent interaction. In consequence, in this chapter I focus exclusively on the dynamical evolution of the binary and the variations between the different levels of anisotropy of the infalling clouds.

5.2.1 Angular momentum

Similar to what I explained in Chapter 4, the first step is to establish whether the simulations have the accuracy to measure the effects of the interaction between the binary and the sequence of clouds. With that aim, I measure the conservation of angular momentum in the different models, as shown in Fig. 5.4. This corresponds to the evolution in the lower resolution simulation, but because the binary evolution is almost independent from the number of particles (see below), these examples illustrate the evolution of the higher resolution models as well.

Consistent with the single cloud models, the largest effect in the binary angular momentum occurs during the interaction with the first incoming material, depicted as vertical shaded areas. The fluctuations after the first encounter with one cloud

TABLE 5.1: Initial position and velocity vectors of each cloud in the different distributions.

Distribution, cloud	$\mathbf{r}$ (a_0)	$\mathbf{v}$ (v_0)
$F = 0.0$, 01	(1.67, 10.44, -1.06)	(-0.05, -0.23, 0.09)
$F = 0.0$, 02	(-11.00, -7.21, -7.20)	(0.22, 0.10, 0.05)
$F = 0.0$, 03	(-0.38, 6.18, -13.66)	(-0.02, -0.17, 0.18)
$F = 0.0$, 04	(-10.65, -5.84, -8.80)	(0.21, 0.09, 0.09)
$F = 0.0$, 05	(-13.12, 7.25, 0.43)	(0.19, -0.16, 0.01)
$F = 0.0$, 06	(-12.88, -0.82, -7.64)	(0.22, -0.08, -0.09)
$F = 0.0$, 07	(-4.79, 11.49, 8.36)	(-0.03, -0.15, -0.19)
$F = 0.0$, 08	(6.41, 12.84, -4.38)	(-0.11, -0.22, 0.06)
$F = 0.0$, 09	(-13.07, -0.03, -7.35)	(0.18, -0.11, 0.14)
$F = 0.0$, 10	(12.04, 8.12, -3.75)	(-0.24, -0.03, 0.05)
$F = 0.5$, 01	(1.67, 10.44, -1.06)	(-0.05, -0.23, 0.09)
$F = 0.5$, 02	(-11.00, 0.12, -10.20)	(0.22, 0.04, 0.11)
$F = 0.5$, 03	(-0.38, -8.35, -12.46)	(-0.02, 0.07, 0.24)
$F = 0.5$, 04	(-10.65, -1.93, -10.39)	(0.21, 0.06, 0.11)
$F = 0.5$, 05	(-13.12, -4.87, -5.39)	(-0.19, 0.12, 0.10)
$F = 0.5$, 06	(-12.88, -0.82, -7.64)	(0.22, -0.08, 0.09)
$F = 0.5$, 07	(-4.79, 11.49, 8.36)	(-0.03, -0.15, -0.19)
$F = 0.5$, 08	(6.41, 12.84, -4.38)	(-0.11, -0.22, 0.06)
$F = 0.5$, 09	(-13.07, -5.28, 5.12)	(0.18, 0.18, -0.02)
$F = 0.5$, 10	(12.04, 8.12, -3.75)	(-0.24, -0.03, 0.05)
$F = 1.0$, 01	(1.67, 1.55, -14.83)	(-0.05, -0.12, 0.02)
$F = 1.0$, 02	(-11.00, 0.12, -10.20)	(0.22, 0.04, 0.11)
$F = 1.0$, 03	(-0.38, -8.35, -12.46)	(-0.02, 0.07, 0.24)
$F = 1.0$, 04	(-10.65, -1.93, -10.39)	(0.21, 0.06, 0.11)
$F = 1.0$, 05	(-13.12, -4.87, -5.39)	(-0.19, 0.12, 0.10)
$F = 1.0$, 06	(-12.88, 6.29, 4.42)	(0.22, -0.01, -0.11)
$F = 1.0$, 07	(-4.79, -7.30, 12.19)	(-0.03, 0.18, -0.17)
$F = 1.0$, 08	(6.41, 1.77, -13.45)	(-0.11, -0.04, 0.22)
$F = 1.0$, 09	(-13.07, -5.28, 5.12)	(0.18, 0.18, -0.02)
$F = 1.0$, 10	(12.04, -8.91, 0.81)	(-0.24, 0.05, -0.04)

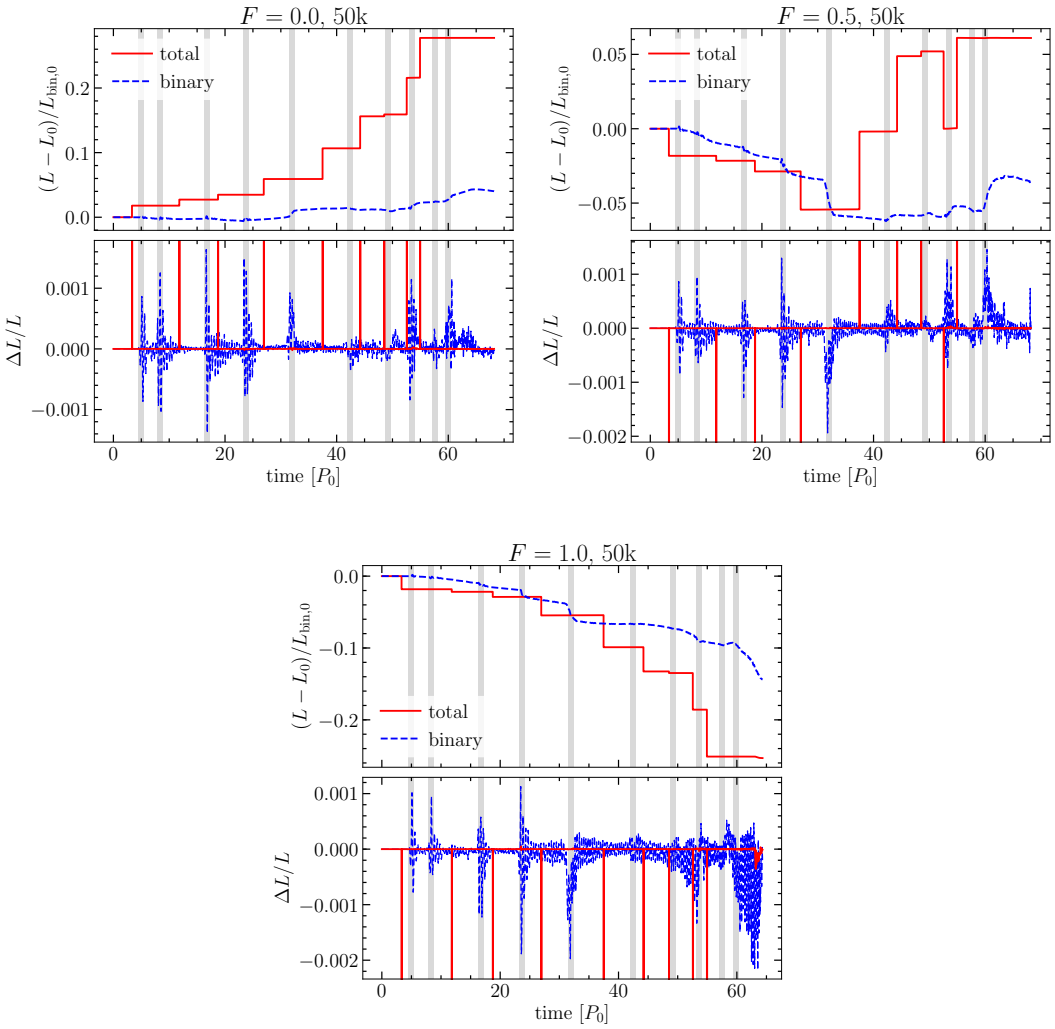

FIGURE 5.4: Angular momentum evolution for the lower resolution runs (`50k`). The upper panels of each plot show the evolution of the angular momentum magnitude of the entire system (solid red lines) and the binary (dashed blue lines). The lower panels display the relative change between snapshots of the same lines. The vertical shaded areas indicate the arrival of one of the clouds to the binary. The extreme "jumps" seen in the red lines are caused by a new cloud entering the system, which does not spuriously affect the binary evolution.

rapidly decrease. It is important to clarify that the rather extreme jumps observed in the total angular momentum are not numerically driven, but produced by the addition of new clouds into the system. From the lower panels of figure 5.4 it is clear that this does not translate into spurious jumps in the binary evolution, as there are no such noticeable changes in its angular momentum. Moreover, the sections delimited by the addition of clouds are extremely flat, i.e. the numerical fluctuations in the total momentum are way below the observed binary evolution and consequently they hardly can be seen at this scale. This implies that the new models have the numerical accuracy to resolve the binary evolution beyond the prompt phase, as opposed to the single cloud simulations.

During the $F = 0.0$ simulation the total angular momentum always increases with the addition of new clouds, whereas in the $F = 1.0$ model the opposite occurs and the momentum decreases. For the isotropic case ($F = 0.5$) the angular momentum increases and decreases depending on whether the new cloud is co-rotating or counter-rotating, respectively. From the top panels of figure 5.4 it is possible to observe that the evolution of the binary is somewhat following the injection of momentum in the form of clouds. In other words, the binary monotonically increases its angular momentum in the $F = 0.0$ model, while continuously decreasing for $F = 1.0$. This is in agreement with my previous results where the main effect of the infalling material is to exchange its angular momentum through capture and accretion. One important point is that an increase in the binary angular momentum does not necessarily imply an expansion of the semimajor axis; this only means that the contribution of the total accreted mass, which is always positive, is much larger to that of the likely negative semimajor axis.

To further study the source of the angular momentum evolution, I show the decomposition of the binary angular momentum on the contributions of its orbital elements (a, e, M, q), similar to what I presented in Chapter 4 (eq. 4.2). As expected, the eccentricity and mass ratio contributions are negligible with respect to the total mass and semimajor axis terms. This is due to the symmetries of the accretion and torques that keep both the mass ratio and eccentricity essentially unchanged during the simulations.

For the $F = 0.0$ model it is worth mentioning that, even though the binary angular momentum increases, the semimajor axis decreases. This can be understood with the scenario drawn by my single cloud models: the capture of the somewhat prograde material adds to the angular momentum budget, whilst the remaining gas is slingshotted away, shrinking the orbit.

5.2.2 Orbital elements

On the grounds of the angular momentum conservation shown before, it is possible to study the evolution of the binary orbital elements during the entirety of the simulations. It is worth mentioning that the computation of the semimajor axis and eccentricity were made considering only the relative energy and angular momentum of the two SMBHs and ignoring the presence of the external potential described above.

Figure 5.6 displays the time evolution of the semimajor axis, eccentricity and mass comparing the different resolutions modelled. Notice that every resolution exhibits an almost identical orbital evolution during the modelled stages, indicating convergence with the number of particles per cloud. The largest disparities are present in the eccentricity evolution. This is due to the typically low values ($e \lesssim 0.02$) of this quantity that makes it much more sensitive to noise. For this reason I restrict

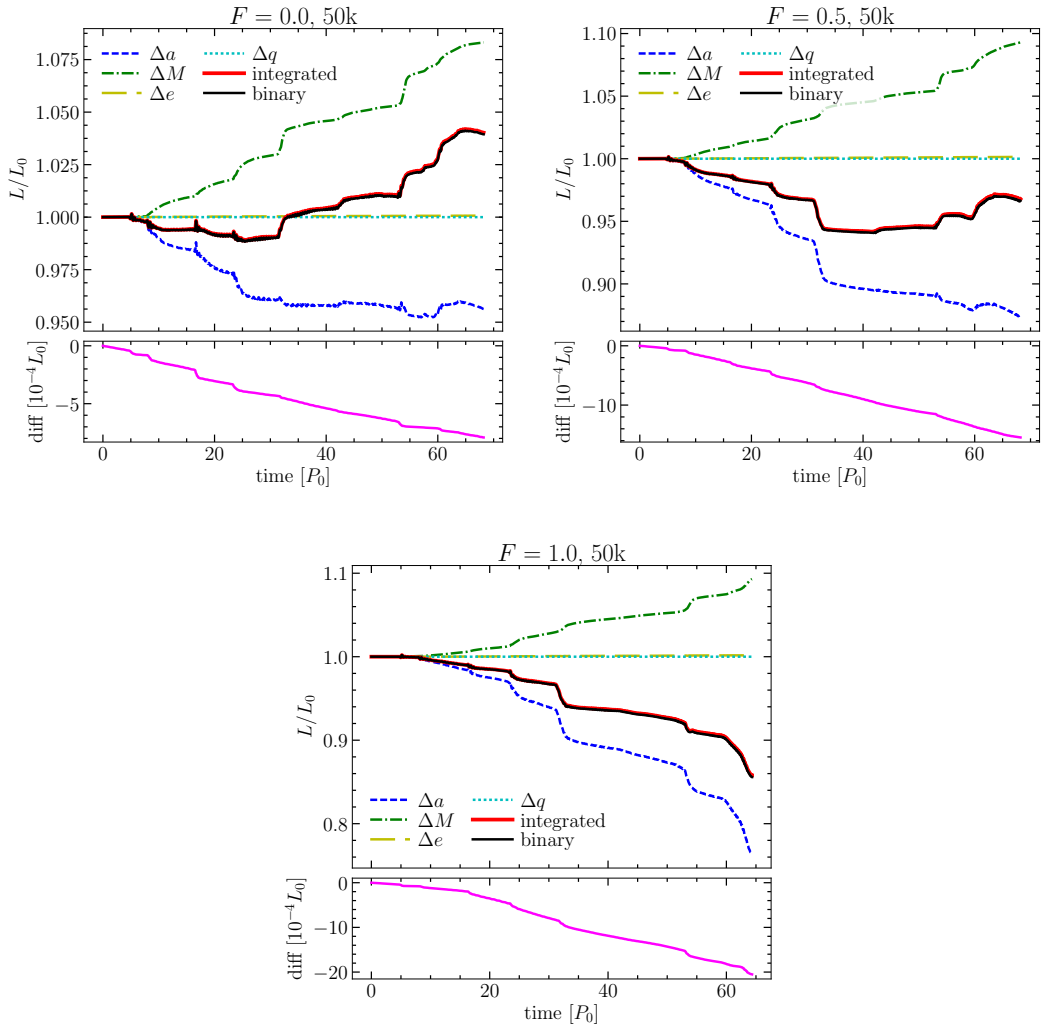

FIGURE 5.5: Decomposition of the binary angular momentum for the different F-distributions. This is similar to what I presented in Chapter 4 (eq. 4.2), where the non-solid lines represent the contribution of the individual components (semimajor axis, total mass, eccentricity and mass ratio), the red solid line is recovered from the contribution of these components, and the black solid line is the momentum directly measured from the snapshots. The lower panels show the difference between these two last lines.

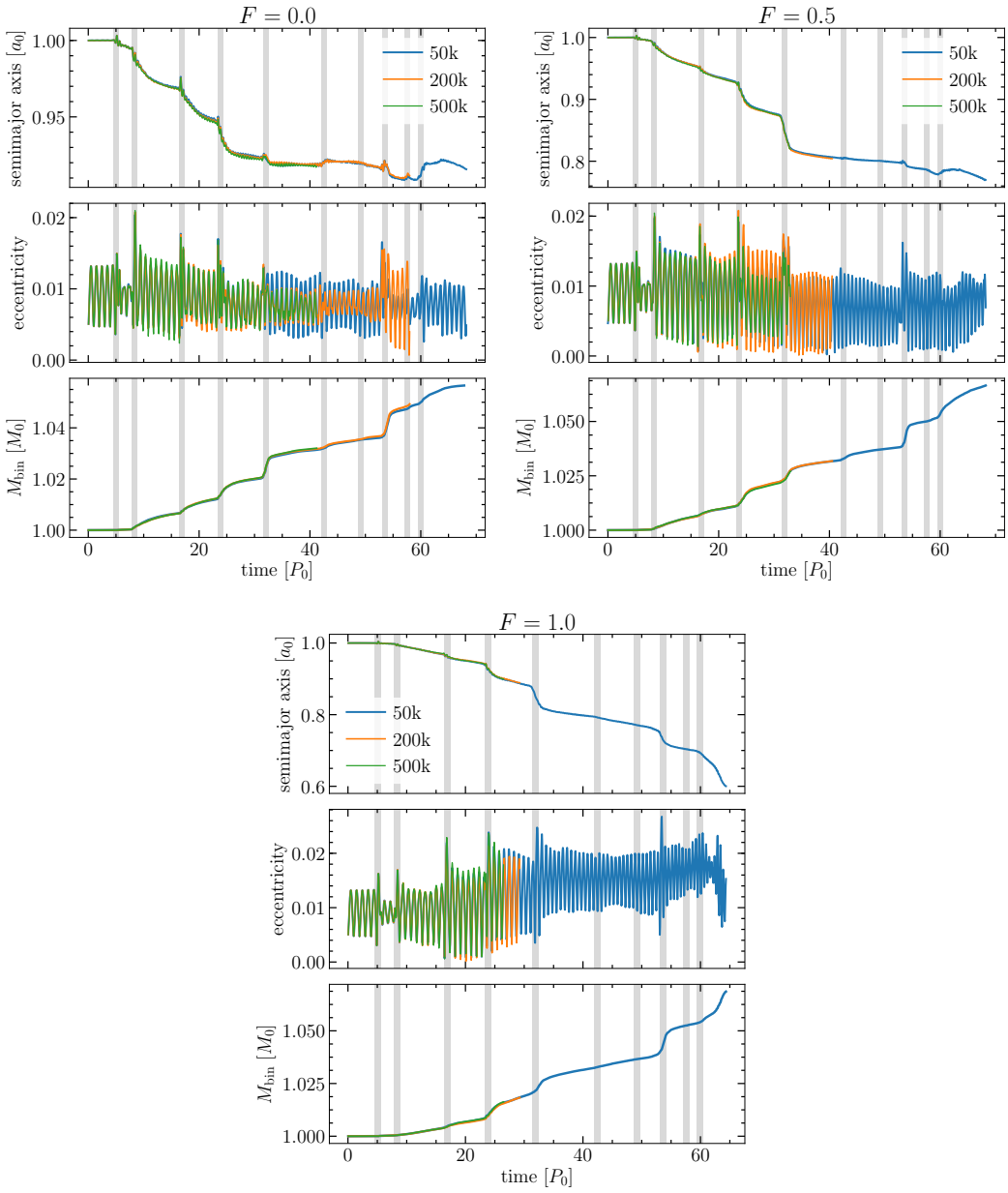

FIGURE 5.6: Evolution of the binary semimajor axis (upper panels), eccentricity (middle panels) and accreted mass (lower panels) during the different simulations. The corresponding distribution is indicated at the top of each plot. The different coloured lines in each panel represent the cloud resolutions, as indicated in the legend. The vertical shaded areas indicate the arrival of one of the clouds to the binary.

TABLE 5.2: Total change of the binary semimajor axis and mass for the different models at the end of the simulation. The model name is composed of the F distribution followed by the resolution of the individual clouds. $T_{\rm fin}$ is the final time reached by each simulation.

Model	$T_{\rm fin}$ (P_0)	Δa (a_0)	ΔM (M_0)
F0.0_50k	68.2	-0.080	0.057
F0.5_50k	68.2	-0.227	0.066
F1.0_50k	64.8	-0.401	0.071
F0.0_200k	58.9	-0.085	0.050
F0.5_200k	40.6	-0.192	0.031
F1.0_200k	29.3	-0.107	0.018
F0.0_500k	42.1	-0.079	0.032
F0.5_500k	32.9	-0.176	0.027
F1.0_500k	27.4	-0.100	0.017

the analysis to the semimajor axis and mass evolution. In any case, such small discrepancies in eccentricity should not affect the overall evolution of the system.

In table 5.2 I summarise the total change in both semimajor axis and mass at the end of the simulations. As expected, increasing the number of particles per cloud makes the simulations more computationally expensive, and consequently I have modelled a smaller number of clouds. Additionally, the $F = 1.0$ models are more expensive than the 2 other distributions because counter-rotating clouds tend to form more clumps. Based on the results showed in Fig. 5.6 and the apparent convergence of the simulation with resolution, most of the analysis in this chapter is based on the 50k runs because more clouds have interacted with the binary. I expect similar conclusions will apply for the higher resolution simulations.

To highlight the differences between distributions, in the upper panel of Fig. 5.7 I group the semimajor axis evolution for the three levels of anisotropy, while the lower panel shows the mass evolution. The solid lines on this figure represent the evolution measured from the simulations. In agreement with the results from the single cloud models, the binary shrinks more efficiently when there are more clouds with angular momentum somewhat anti-aligned with its orbit. This is because retrograde interactions are more efficient in subtracting angular momentum from the binary, while prograde encounters tend to slightly expand its orbit. More specifically, after the infall of 10 clouds the orbit shrinks $\Delta a/a \approx 40\%$ during the $F = 1.0$ simulation, $\Delta a/a \approx 23\%$ in the $F = 0.5$ model and a mere $\Delta a/a \approx 8\%$ for $F = 0.0$. In contrast with the binary semimajor axis, the mass evolution remains very similar for the three levels of anisotropy, as the capture of material does not depend strongly on the orbit of the incoming gas. However, because the gas exchanges its angular momentum with the accreting black holes, the net effect in the binary orbit does depend on the different relative inclinations.

In the Monte Carlo models presented in Chapter 4 I have extrapolated the results from the single cloud simulations to evolve a binary embedded in a clumpy environment where individual gas pockets infall with different levels of anisotropy. One of the critical assumptions made in this approach was ignoring the effects of the left-over material after the first stages of the interaction. To investigate this effect I compute the binary evolution following the same procedure explained in § 4.4.1, i.e. estimating the total change in mass and semimajor axis based on the cloud's initial orientation and pericentre distance, using the values extrapolated

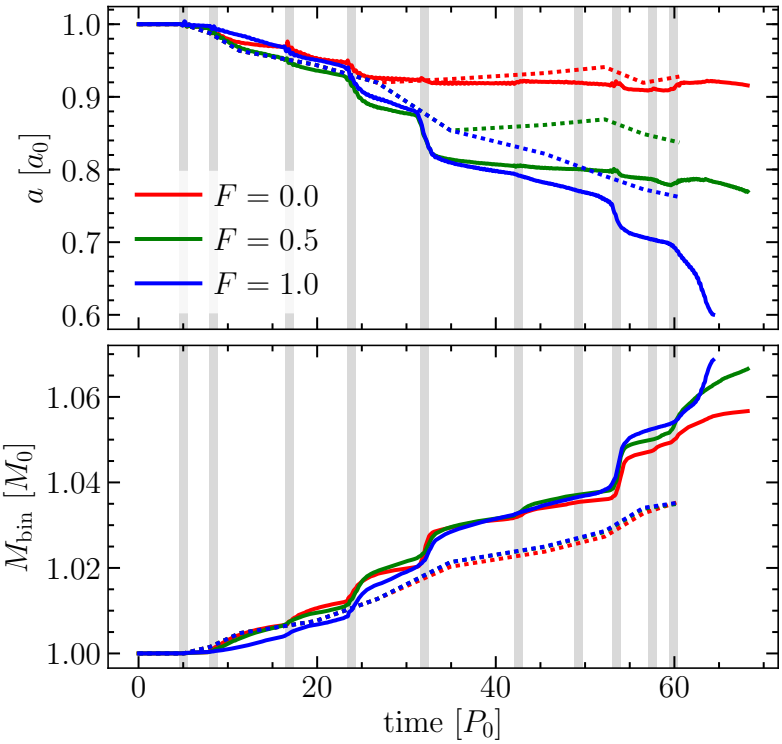

FIGURE 5.7: Time evolution of the binary semimajor axis (top panel) and mass (bottom panel) for the different cloud distributions, as indicated in the legend. The solid lines depict the evolution measured directly from the simulations, while the dashed lines correspond to predictions based on the results from the single cloud models. Similar to previous figures the shaded vertical areas illustrate the start of the interaction of the binary with a new cloud.

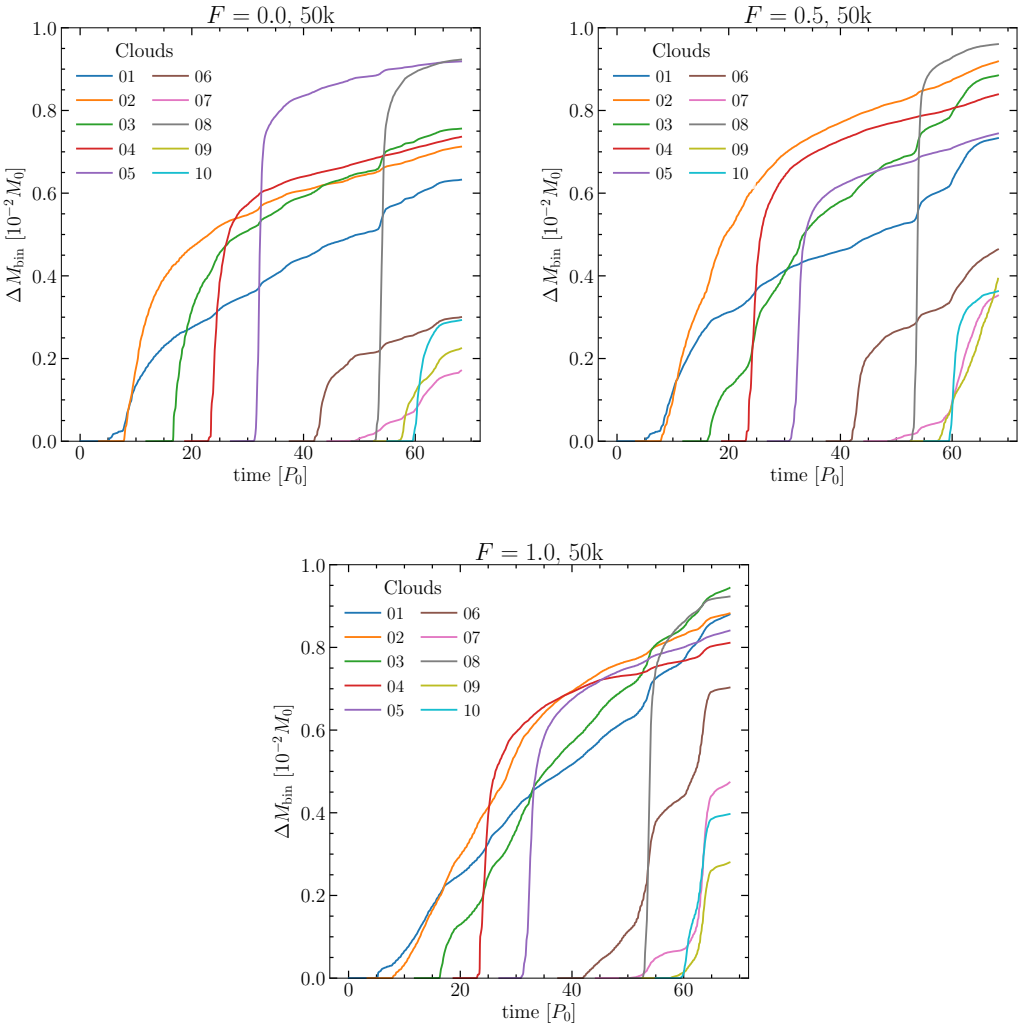

FIGURE 5.8: Time evolution of the accreted mass contributed by each cloud in the different distributions. Note that the mass is presented in unit of $10^{-2} M_0$, which corresponds to the initial mass of each cloud, thus the y-axis can be interpreted as the fraction of the cloud that has been accreted by the binary.

from the single cloud models. In this procedure I deliberately ignore any secular effects from the non-accreted gas by considering only the evolution measured during the prompt accretion phase. The results obtained are shown with dashed lines in Fig. 5.7.

During the interaction with the first few clouds the single cloud predictions agree very well with the actual binary evolution, but after a few events this simple model consistently underestimates both semimajor axis and mass evolution. For instance, the single cloud extrapolation underestimates the final mass by a factor of ~ 2. This occurs because there is an accumulation of material around the binary, and the new incoming clouds are able to drag some of it, increasing accretion and consequently the effect on the binary semimajor axis. Note that the deviation of the measured evolution from the "predicted" one is rather episodic instead of continuous.

To corroborate this point, I present the contribution from each individual cloud to the mass accreted by the binary in Fig. 5.8. Here it is possible to observe that some of

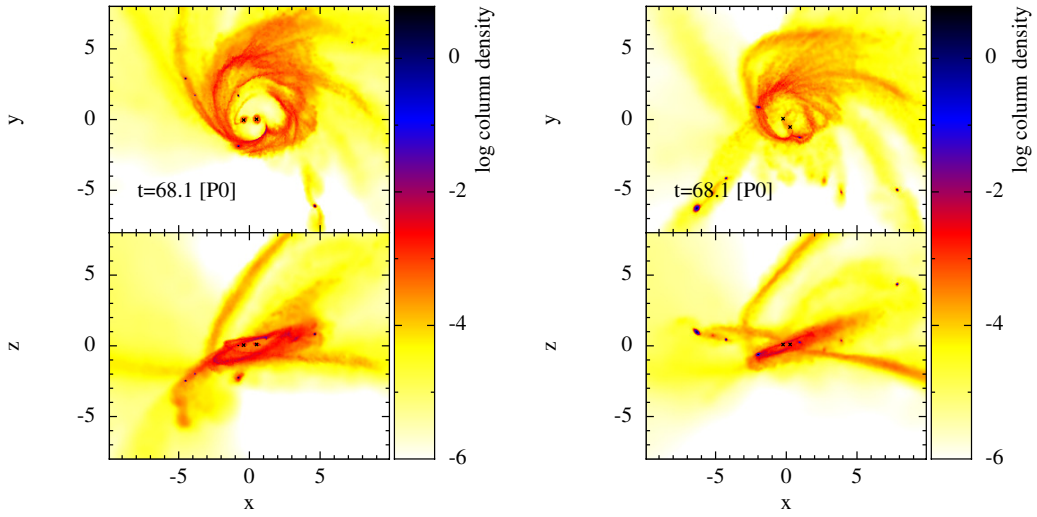

FIGURE 5.9: Column density maps of the final output from models $F = 0.0$ (left) and $F = 0.5$ (right). The top and bottom panels show a face-on and edge-on view of the circumbinary structure formed after the interaction with 10 gaseous clouds.

the incoming clouds produce an accretion spike also in some of the previous clouds. For example, one of the most noticeable cases is the arrival of cloud 8 (grey line on each panel), which brings to the binary a significant fraction of clouds 1, 3 and 6 (blue, green and brown lines, respectively). Recall from figure 5.3 that the 8th cloud has the smallest pericentre distance, very close to zero. This event produces the largest accretion in all distributions, a behaviour that is not captured by the simple model derived from the single cloud simulations (Fig. 5.7).

5.2.3 Circumbinary disc formation and secular evolution

As thoroughly discussed in Chapter 4, another effect expected from the left-over gas is the formation of circumbinary structures. This represents one of the most important limitations of the models based on the single cloud simulations. For instance, in the extreme case where every cloud comes exactly coplanar and corotating with the binary (sometimes referred as the "prolonged accretion" scenario), the extrapolation from the single cloud models predicts that the semimajor axis would only increase. In reality however, following several of such accretion events a massive circumbinary disc is expected to form. This structure can continue extracting and transporting the binary angular momentum, evolving the binary towards coalescence.

Approaching the end of the simulation, after the prompt interaction with the 10th cloud, the binary semimajor axis decreases during the $F = 0.0$ and $F = 0.5$ models (see e.g. the red and blue lines in Fig. 5.7). Furthermore, because the last cloud is almost aligned with the initial binary orbit (see Fig. 5.2), the latter expands by the addition of angular momentum. This situation shortly reverses after the first impact, when the semimajor axis shrinks. As there is no more infall of material in the form of clouds, this is produced by secular torques of the remaining gas acting onto the binary.

During the aforementioned simulations, I observe the formation of a well defined circumbinary after the interaction with 10 clouds. This is clearly seen in

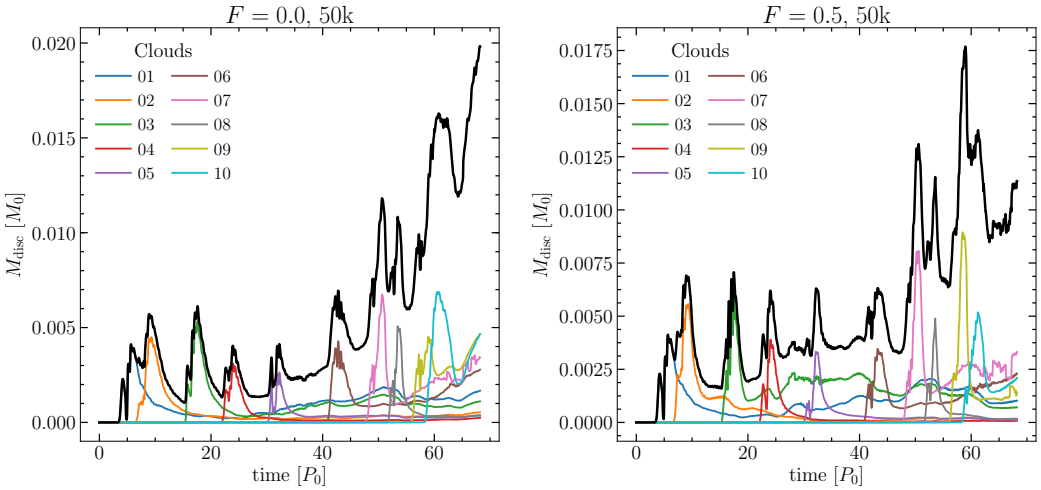

FIGURE 5.10: Mass evolution of the circumbinary discs for the models $F = 0.0$ (left) and $F = 0.5$ (right). The different coloured lines represent the contribution from each cloud, while the black line is the sum of all clouds. Because for most of the simulations there is not a well defined disc, I estimate this mass by considering all the bound gas within $5a_0$ from the binary.

Fig. 5.9, where I display density maps of the final output of these models. Both discs are corotating and roughly coplanar with the binary orbit, thus they have the potential to extract and transport outwards some of the binary angular momentum, shrinking its orbit. For the $F = 1.0$ distribution the gas has not yet settled into a clear circumbinary structure, but recall that this simulation did not reach the same time. Consequently, I will refer only to the other two models for the rest of this analysis.

After the interaction with all the simulated clouds, roughly 60% of the gaseous material has been captured and accreted by the SMBHs, leaving a total mass of $\approx 0.04M_0$ around the binary to continue influencing its evolution. In Fig. 5.10 I show the time evolution of the total bound mass around the binary ($r < 5a_0$), as well as the contribution from each individual cloud. This mass serves as an approximation of the real mass of the circumbinary disc, if present. There is a clear trend of this mass to increase in time because of the accumulation of the left-over material from the different accretion events. The disc formed in the `F0.0_50k` model has a mass of $M_{\rm disc} \approx 0.02M_0$, with the largest contributions of material from clouds 9 and 10 with 23% each, followed by cloud 7 with 17% and cloud 6 with 14%. The rest of the clouds contribute with just a few percent each. On the other hand, the `F0.5_50k` model forms a disc with a mass of $M_{\rm disc} \approx 0.01M_0$, with the largest contributions from cloud 7 with 27%, cloud 6 with 21%, cloud 10 with 19%, and cloud 9 with 13%. Again the remaining clouds contribute with only a small fraction of the remaining mass. It is interesting that in the latter case the 7th cloud is the event that yields the highest mass fraction. This is because (i) cloud 7 has the largest impact parameter ($r_{\rm p} \approx 2a_0$), which allows more mass to avoid being accreted by the SMBHs; and (ii) cloud 9 and 10 have very similar pericenter distances but almost opposite orientations (see Figs. 5.2 and 5.3), hence their combined angular momentum is very low. The opposite occurs for the $F = 0.0$ model, where these two clouds are somewhat coherent between each other and the binary, which allows them to settle into the

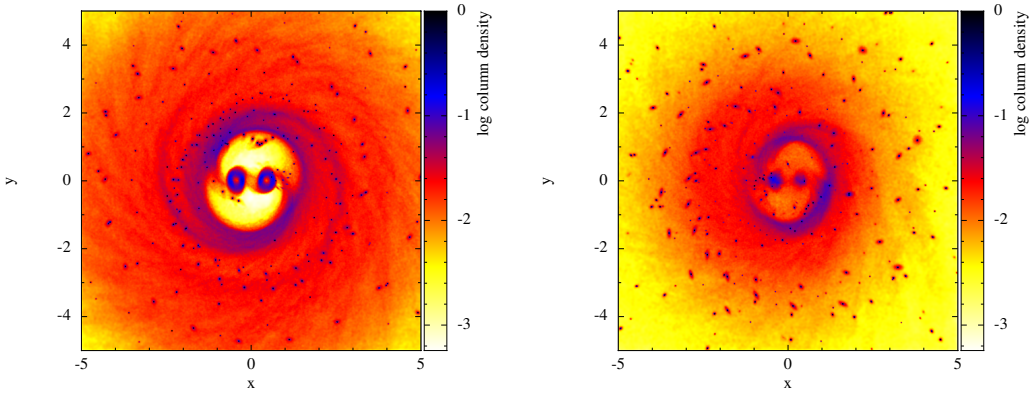

FIGURE 5.11: Density maps averaged over the last 5 binary orbits for the $F = 0.0$ (left) and $F = 0.5$ (right) models. These maps were computed in a reference frame corotating with the binary. Recall that the large amount of clumps seen in both panels corresponds to a few orbiting the binary instead of further fragmentation of the gas.

disc, contributing with almost half of the total mass.

To study any persistent structures of these developing discs I present the column density maps averaged over the last five binary orbits (100 snapshots) in Fig. 5.11. These maps were computed in a reference frame corotating with the binary, with both black holes lying on the x-axis. Recall that the large amount of clumps seen in both panels corresponds to just a few orbiting the binary instead of fragmentation of the disc (see Fig. 5.9). It is clear that the gaseous structures are better defined in the $F = 0.0$ simulation, where the binary has opened a clear cavity and each SMBH is surrounded by prominent mini-discs. In contrast, the less coherent infall of material during the $F = 0.5$ simulation delays the emergence of these features. Nevertheless, in both cases there is a dense, roughly circular ring of gas located at $r \approx 2a$. In this region the material piles up due to resonances with the gravitational potential of the binary (Artymowicz and Lubow, 1994).

Although the gravitational forces keep most of the gas confined at this radius, some material leaks thorough the cavity wall in the form of narrow streams that reach the black holes, a result that has been extensively reported in the literature (e.g. Artymowicz and Lubow, 1996; MacFadyen and Milosavljević, 2008; Cuadra et al., 2009; Roedig et al., 2012; D'Orazio, Haiman, and MacFadyen, 2013; Farris et al., 2015a; Tang, MacFadyen, and Haiman, 2017). Such inflowing gas can exert a net negative torque inside the cavity region, shrinking the binary more effectively than the resonant torques.

To establish the role of the disc in the binary evolution I compute the gravitational torques exerted by the gas. The total gravitational torque is given by directly summing the individual particle torques onto each SMBH as follows

$$\mathbf{T}_g = \sum_{i=1}^{N} \sum_{j=1}^{2} \mathbf{r}_j \times \frac{G M_j m_i}{|\mathbf{r}_i - \mathbf{r}_j|^3} (\mathbf{r}_i - \mathbf{r}_j), \tag{5.11}$$

where the index i goes through all the gas particles in the simulation, and j the black

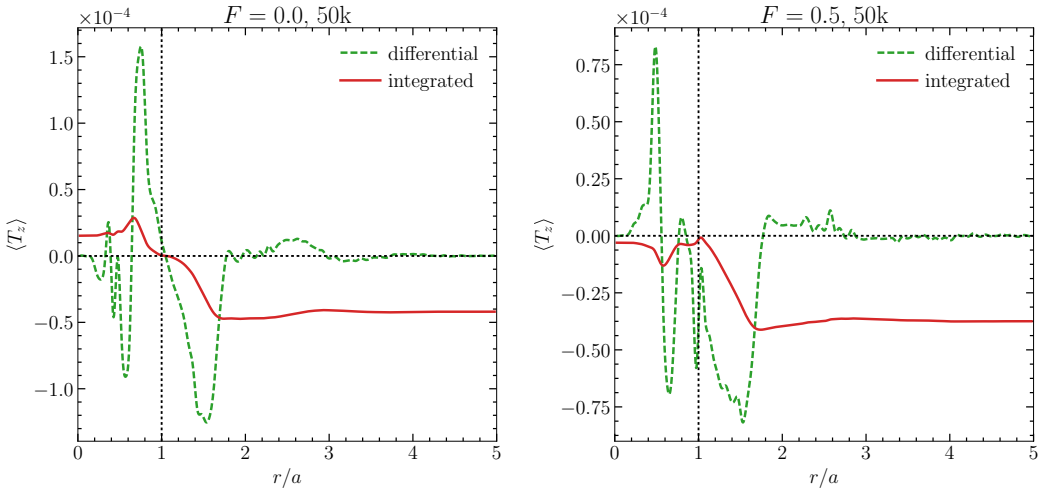

FIGURE 5.12: Torque radial profiles averaged over the last five binary orbits. The green dashed lines represent the differential torque, while the red solid lines are the total integrated torque. This latter is integrated starting from the corotation radius (vertical dotted line) inwards and outwards. The quantities are presented in code units, namely, $[GM_0^2 a_0^{-2}]$ for the differential torque and $[GM_0^2 a_0^{-1}]$ for the integrated profile.

holes. Using this expression, I compute the torque radial profiles shown in Fig. 5.12, averaged over the final 5 orbits of the simulation. I use a reference frame in which the binary angular momentum is exactly aligned with the z axis, only this component of the torque is responsible for evolving the binary orbit. Because the torques are null at the corotation radius, the integration of the differential profile is made from that point outwards and inwards.

From the profiles shown in figure 5.12 it is clear that the net effect of the circumbinary material is to produce a negative torque, hence to extract some angular momentum from the binary. The more important peak is located between a and $2a$, i.e. inside the cavity wall. This peak basically determines the total strength of the torque, which is responsible for the shrinking observed in the binary orbit. Beyond the cavity region the torques oscillate between positive and negative, cancelling each other out, and consequently making the contribution of the disc negligible.

To identify the location of the negative torques, I show the averaged surface density torque of both discs in Fig. 5.13. Similar to the gas distribution shown in figure 5.11, the location of the torques are clearer in the $F = 0.0$ model, where the cavity has been almost completely depleted of gas. Nonetheless, in both cases the gaseous streams inside the cavity provide a strong source of negative torque. This confirms that the negative peak observed in the profiles of figure 5.12 comes from the material leaking through the cavity wall. Rather than being entirely captured by the binary, a fraction of this gas is returned to the disc, via gravitational slingshot, carrying some angular momentum.

The profiles shown in figure 5.12 can be directly compared with results from previous studies of "standard" circumbinary discs. In particular, the simulations of a massive self-gravitating circumbinary disc by Roedig et al. (2012) find very similar torque profiles (cf. their Fig. 6), the main distinction being the strength of

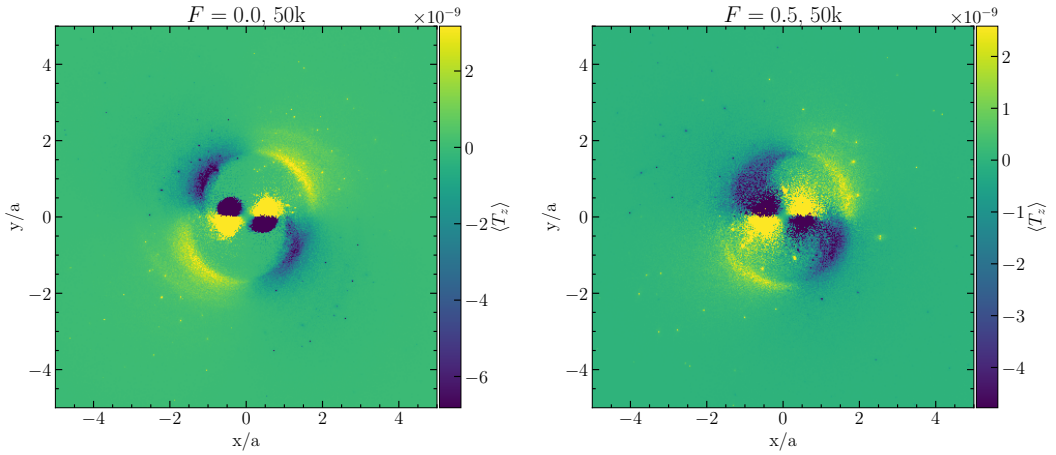

FIGURE 5.13: Averaged surface density torque exerted by the gas onto the binary for the $F = 0.0$ (left panel) and $F = 0.5$ (right panel) models. Similar to the previous figures, these maps were averaged over the last five orbits. Note that the torque values for the minidiscs are off the scale in both models.

the peaks. The torques found in my simulations are noticeably larger – Roedig et al. show a total integrated torque $\sim 2 \times 10^{-5}$ $[GM_0^2 a_0^{-1}]$, while in these simulations is $\sim 5 \times 10^{-4}$ $[GM_0^2 a_0^{-1}]$, hence a factor of ~ 25 difference. This is due to the transient nature of the discs formed from the discrete accretion events, where the binary is still clearing its orbit of gaseous material. If these circumbinary discs were to settle in a more steady-state such as the model of Roedig et al. (2012), the gaseous streams will be determined mainly by the internal viscous torques, and I would expect much less mass interacting directly with the binary. This would decrease the efficiency of the gravitational torques, especially considering their low mass with respect to the SMBHs. The larger strength of the torques in these models demonstrates that the observed evolution produced by the discs is still transient and not a long-term effect. However, provided a continuous inflow of gaseous clouds exists, the circumbinary structure would never reach a steady-state, and the transient effects of the interaction will dominate the overall binary evolution.

5.3 Discussion

The simulations presented in this chapter were motivated by the simplifying assumptions of the Monte Carlo models presented in Chapter 4, mainly, the fact that I was considering only the prompt evolution during the cloud's first impact and ignoring any secular torques by the non-accreted material. By directly modelling the interaction with several clouds, I now can study the influence of the left-over gas on the binary orbital evolution.

One striking difference with respect to the model derived from the single cloud simulations is the total accreted mass. The Monte Carlo evolution shown in Chapter 4 predicted an average accreted fraction of around 0.3, similar for every F-distribution. In these new models, however, this fraction becomes ≈ 0.6 after interacting with 10 gaseous clouds. From figure 5.7 it is clear that the models start to diverge after a few clouds. In this multi-cloud scenario, a significant amount of gas

is surrounding the binary, and the new incoming clouds are able to drag part of the surrounding material. This has the effect of bringing more angular momentum to exchange with the binary, which finally enhances the effect on the semimajor axis.

Another effect measured with these new models is the formation of circumbinary discs and their gravitational influence on the binary. Many theoretical and numerical studies over the past years have focused on the orbital evolution of a sub-parsec binary surrounded by a gaseous accretion disc. However, in most of these models relaxed steady discs are assumed as an initial condition. The evolution of the SMBHB is "decoupled" from the host galaxy, in the sense that there is no attempt to model the formation of the circumbinary disc structure, nor to link it to the fuelling mechanisms that transport gas from galactic scales down to the binary. With these models I have shown that incoherent infall of gaseous clouds can lead to the formation of a coplanar and corotating circumbinary disc. Some of the non-accreted material efficiently aligns due to dissipation, resulting in the well defined discs presented above.

By computing the gravitational torques of the surrounding gas, I have demonstrated that the semimajor axis shrinkage at late stages observed in the simulations is dominated by the presence of these discs. The outwards transport of the binary angular momentum is done by the gaseous streams that penetrate the cavity wall. As this gas interacts with the binary, a fraction is returned to the disc's edge via gravitational slingshot, depositing the extracted angular momentum in the disc.

The estimation of the disc's mass using the gravitationally bound gas around the binary shows a tendency to increase with time (Fig. 5.10), although 10 clouds is still a small number to establish whether this will continue for more events. Nevertheless, this mass grows with the contribution from all the interacting clouds, albeit some of them with a tiny fraction, which suggests that after a sizeable amount of events the disc is likely to grow sufficiently to become self-gravitating. Such massive structures had been shown to be efficient in shrinking the binary orbit because the disc's own self-gravity acts as an effective viscosity by transporting angular momentum (e.g. Cuadra et al., 2009).

An interesting case is the isotropic scenario $F = 0.5$ where the total angular momentum of the gas should be close to zero, at least for a large number of gas clouds. In this scenario, the highly misaligned gas will tend to cancel lots of angular momentum, sending material plunging onto the binary. Therefore I would not expect a steady circumbinary disc to survive under these conditions. Following a sequence of 10 clouds, however, there is a clear circumbinary structure rising from the non-accreted material, which is already producing a noticeable effect on the binary orbit. This implies that the formation of circumbinary discs is a relevant process even for the $F = 0.5$ model, even if these discs are transient and with negligible self-gravity. Recall that one of the assumptions of the Monte Carlo models presented in Chapter 4 is that there is no circumbinary disc during the isotropic scenario due to the low total angular momentum of the gas. These results clearly refute this assumption.

During the stages modelled, the mass of the circumbinary discs is very small compared to the binary and hence their self-gravity is negligible. In this situation the outwards transport of angular momentum throughout the disc will occur through an unresolved viscosity (see e.g. Syer and Clarke, 1995; Ivanov, Papaloizou, and Polnarev, 1999). For geometrically thin and optically thick discs, this viscosity is commonly parametrised using the α-disc model (Shakura and Sunyaev, 1973), where α represents the strength of the internal viscous stresses. In

my models, however, the only source of viscosity is the artificial term introduced to capture shocks, hence the transport of angular momentum throughout the disc is likely not well resolved. Additionally, the evolution of the binary-disc system might be affected by the simple thermodynamics adopted in these models. As discussed in Roedig et al. (2012), the morphology of the streaming gas has a major impact in the binary evolution and the structure of the surrounding disc, thus it is directly influenced by the gas thermodynamics. On the other hand, Tang, MacFadyen, and Haiman (2017) using 2D hydrodynamical simulations of circumbinary accretion discs found that the torques are sensitive to the sink prescription: slower sinks result in more gas accumulating near the SMBHs, driving the binary to merge more rapidly. Nevertheless, all these effects become relevant for the *long-term* evolution of a SMBHB embedded in a circumbinary disc. During the infall of a sequence of clouds the relevant mechanisms involved in the binary's orbital response are almost purely dynamical, namely, gas capture and gravitational slingshot, which are well resolved with these models. In consequence, these simulations require a more physical treatment for the viscosity, thermodynamics and accretion only if one wants to resolve the long-term evolution of the SMBHB surrounded by a circumbinary disc arising in the aftermath of the accretion events.

A somewhat different aspect that might be impacting my results is the resolution elements of the individual clouds. For instance, Dunhill, Cuadra, and Dougados (2015) found that resolution was important in the gaseous streams going through the cavity wall. As discussed above, the streams play an important role transporting angular momentum once the circumbinary disc has formed, thus the late evolution measured using the lower resolution runs is likely affected by this issue. However, given the almost identical evolution between resolutions during the overlapping stages, I would not expect large differences in the binary's final orbit.

All the results shown in this chapter suggest that the secular effects of the left-over material increase the efficiency of the incoherent infalling clouds to bring the SMBHs towards coalescence with respect to a scenario that only considers the evolution during the prompt accretion phase.

Chapter 6

Conclusions

In this thesis I have developed a suite of different hydrodynamical simulations to explore the hypothesis of infalling clouds as a driver of the orbital evolution of supermassive black hole binaries. The first series of models, presented in Chapters 3 and 4, considers the effects produced by a single cloud as it is being captured by a binary. I then expanded this models to the infall of a sequence of clouds with different anisotropy levels in their angular momentum distributions. In this final chapter I summarise the results of each of these chapters, and I discuss possible directions for future research. I conclude with a short wrap up of this thesis as a body of work.

6.1 Chapter summaries

6.1.1 Gas dynamics and accretion

In Chapter 3, I presented numerical SPH models of the evolution of a turbulent cloud in near-radial infall onto equal-mass, circular supermassive black hole binaries. In order to explore different orbital configurations for the cloud I performed a total of 12 simulations, changing both the impact parameter and the relative inclination between orbits.

I studied the formation and dynamics of discs around the binary and each SMBH depending on those orbital configurations. My main findings can be summarised as follows:

1. I only observe the formation of stable and prominent (up to the Hill radius) mini-discs for the aligned models, independent of the cloud impact parameter. For the other orientations, where the gas trapped by the individual SMBHs has little angular momentum, the models do not have the spatial resolution to observe the possible formation of smaller mini-discs.

2. The misalignment of the mini-discs around each SMBH seems to be a natural outcome of the infall of extended gas clouds. I have confirmed the analytical result that misaligned mini-discs will precess and wobble due to the presence of a companion SMBH.

3. When the impact parameter is large enough (pericentre distance $\approx 3R_{\rm bin}$) I always observe the formation of a circumbinary disc, independent of the orbit orientation. In the counter-aligned cases there is formation of a circumbinary disc (or ring) for all impact parameters due to the less efficient slingshot effect with respect to the other orientations.

4. The circumbinary discs tend to follow the initial orientation of the cloud. I have confirmed that a misaligned disc will slowly evolve towards alignment, as expected.

5. The circumbinary discs are initially very eccentric ($e \gtrsim 0.6$), and their early evolution will depend on the relative orbital inclination. In the aligned model, the gas tends to increase its eccentricity, while the opposite is true in the counter-aligned model. In the perpendicular cases the eccentricity distribution becomes narrower without changing its median value.

6. The feeding rates onto the binary and each SMBH show variability in all models, always related to the orbital period.

Although my simulations do not allow a direct scaling to SMBHBs with orbital periods of few years (i.e., accessible to future time-domain surveys), I argue that the observed qualitative phenomenology, which is mostly driven by the gravitational torques exerted by the SMBHB onto the gas, can be safely extrapolated to shorter periods. Such phenomenology has distinctive electromagnetic signatures, which are very relevant for the future identification and characterisation of SMBHBs.

6.1.2 Binary orbital evolution

In Chapter 4 I studied the orbital evolution of an equal mass, circular SMBHB interacting with an impacting gas cloud. Exploiting a suite of 13 high resolution hydrodynamical simulations, I investigated the response of the SMBHB orbit as a function of similar orbital configurations as the ones presented in the previous chapter. In these simulations the cloud mass is only 1% of the SMBHB mass, so the binary orbit is expected to suffer only small changes. In order to establish if the models have the accuracy to reliably measure the effect, I compared the evolution of the SMBHB angular momentum to the level of angular momentum conservation during the simulations. I found that the former is appreciably larger than the numerical noise during the first few binary orbital periods, which allows to robustly measure the transient evolution of the orbital parameters in this phase. I therefore presented only results for the strong initial binary–cloud interaction, discarding the subsequent (much slower) secular evolution of the binary. My main findings can be summarised as follows:

1. I focused the analysis on the semimajor axis evolution. I found that its total change during the strong transient interaction depends on the orbital configuration of the system, and it is closely related to the fraction of mass that gets accreted. In particular, the binary shrinks the most when interacting with counterrotating clouds which carry negative angular momentum (with respect to the SMBHB orbital angular momentum) that cancels out upon accretion. Conversely, prompt accretion of corotating gas, causes the orbit to expand, in contrast to the long-term evolution seen in persistent massive circumbinary discs.

2. Using a simple analytical model, I showed that, for all configurations, the evolution of the binary orbital elements is dominated by the transfer of angular momentum from the cloud to the binary through the accretion of gas during the first stages of the interaction. Considering only the angular momentum budget of the accreted material is sufficient to satisfactorily reproduce all the trends for the total evolution of the SMBHB angular momentum vector (either magnitude or inclination) and semimajor axis.

3. By further including the effects of gravitational slingshot from the SMBHB onto the non-accreted material and by using a more accurate estimate of the accreted angular momentum, the evolution of the SMBHB semimajor axis and angular momentum was reproduced within a few percent. This confirms that the simulations are accurate enough to capture the correct evolution of the SMBHB, and that the underlying physics is under control.

4. Since the SMBHBs were initially circular, any asymmetric torque (such as the one exerted by an interacting cloud) would excite some eccentricity. This is in fact observed in all my simulations, however, the eccentricity growth is too small and noisy to draw any conclusions.

The resulting semimajor axis evolution as a function of the orbital configuration of the system was then used as the basis to construct a simple Monte Carlo model for evolving a SMBHB interacting with a sequence of incoherent impacting clouds. I take cloud distributions from reasonable populations with different levels of anisotropy in their angular momenta, based on the studies of Dotti et al. (2013) and Sesana et al. (2014). These distributions can be linked to the morphological and kinematical properties of the host galaxies. Disc galaxies, where the gas dynamics is dominated by rotational velocity, will produce mainly coherent accretion events, while bulge galaxies, dominated by velocity dispersion, will tend to produce more uniformly distributed events. I found that the evolution of the orbit is fastest when the distribution of clouds corresponds to mostly retrograde events ($F = 1.0$), whereas going to isotropic ($F = 0.5$) and then to mainly prograde ($F = 0.0$) events, the evolution progressively slows down. This is because retrograde interactions are more efficient subtracting angular momentum from the SMBHB, while prograde encounters tend to slightly expand its orbit.

Finally, I used the results from the Monte Carlo realisations to calibrate a simple analytical system of coupled differential equation that captures the long-term evolution of the SMBHB as a function of two efficiency parameters. By scaling this analytical description to astrophysical systems, I found that typical SMBHBs efficiently evolve down to the GW emission regime within a few hundred million years. This demonstrates that the interaction with individual clouds in near-radial infall is capable of efficiently shrinking the binary orbit, providing a viable solution to the final parsec problem in clumpy gas-rich environments.

This treatment is subject to a number of caveats and limitations. In particular: i) I am discretising the angular momentum space into just four configurations, which does not take into account intermediate inclinations, and ii) I treated each SMBHB–cloud interaction in isolation, neglecting the non-accreted material that will eventually accumulate, forming circumbinary structures and/or increasing accretion onto the binary. I test the robustness of the model by including approximations for these two effects into the calculations. I find that the timescale to reach the GW regime changes by no more than a factor of 3, which does not alter the already mentioned conclusions. For instance, I demonstrate that even when a massive circumbinary forms with the remaining material, the effect of the infalling clouds would be "at worst" comparable. Additionally, the accretion rates measured during the transient evolution are typically super-Eddington (up to $\approx 50\dot{M}_{\rm edd}$), thus suggesting that radiation pressure-driven outflows can alter the amount of material that actually reaches the SMBHs. I stress however that even if all the material that crosses the accretion radius is eventually ejected from the system, the semimajor axis evolution will be only mildly affected. This is because the exchange

of angular momentum occurs during the capture of the material rather than the accretion itself.

6.1.3 Multiple infalling clouds

Finally, in Chapter 5 I introduced a new suite of simulations to study the evolution of a binary embedded in a turbulent environment, where I expect several gaseous clumps to infall and dynamically interact with the binary. The main goal was to overcome the limitations of the Monte Carlo evolution presented in the previous chapter by directly modelling the interaction of a SMBHB with a sequence of incoherent accretion events. This model combines the 'discrete' evolution due to the prompt interaction of each individual cloud, with the secular torques exerted by the left-over gas. The latter was discarded for the single cloud models due to numerical considerations.

In order to directly compare with the results of the Monte Carlo evolution of Chapter 4, the cloud orbits where sampled using the same probability density functions. In particular, I have used the F-distributions for the angular momentum orientation which are an indication of the anisotropy levels in the surrounding medium.

My main findings can be summarised as follows:

1. The SMBHB angular momentum evolution follows the injection of momentum in the form of clouds. That is, the binary monotonically increases its angular momentum (even though it still shrinks) in the $F = 0.0$ model where each new cloud adds to the total momentum budget, while continuously decreasing for $F = 1.0$ where the opposite occurs. This is consistent with the scenario where the orbital evolution is dominated by the exchange of angular momentum through capture and accretion, as demonstrated with the single cloud simulations.

2. The binary exhibits an almost identical orbital evolution with every resolution during the overlapping stages. This is because the dynamical evolution of the system is dominated by capture and gravitational slingshot, which are properly resolved even with a low number of particles.

3. The largest differences are present in the eccentricity evolution due to typically low values ($e \lesssim 0.02$) that makes it much more sensitive to noise. Because of this reason, I focused the analysis on the semimajor axis and mass evolution, considering that the binary remains circular.

4. Also concordant with the single cloud simulations, the evolution of the semimajor axis is strongly dependent on the cloud distribution, being fastest when it includes more retrograde events. On the other hand, the binary mass evolution remains roughly independent of the cloud distribution during most of the interaction.

5. By directly comparing the observed binary evolution with an evolution extrapolated from the single cloud models, I found that accretion increases considerably with respect to a SMBHB considered in isolation. This occurs because the incoming material is able to drag inward a fraction of the surrounding gas. This effect also shrinks the semimajor axis more efficiently by bringing more angular momentum to exchange with the SMBHB.

6. During the last simulated stages of the $F = 0.0$ and $F = 0.5$ models there was the formation of a well-defined, coplanar and corotating circumbinary disc. By computing the gravitational torques exerted by the surrounding gas, I have demonstrated that these discs are able to transport some of the binary's angular momentum via gaseous streams that are slingshotted away once they get close to the SMBHs. This process continues to shrink the binary orbit during the absence of new impacting clouds.

Finally, I have discussed some numerical considerations to take into account to accurately resolve all the stages of evolution, in particular the long-term evolution of the SMBHB embeded in a putative circumbinary disc as a result of the multiple accretion events. In any case, the results exhibited in this chapter suggest that the secular effects of the left-over material increase the efficiency of the incoherent infalling clouds to bring the SMBHs towards coalescence respect to a scenario that only considers the evolution during the prompt accretion phase. Consequently, provided there is a reasonable rate of events, these models confirm that infalling clouds present a viable mechanism to overcome the 'final parsec problem'.

6.2 Discussion and avenues for future research

This section presents a series of aspects that were neglected in the main body of this report, but represent very interesting options for further investigation. All the following points were explored during the course of this research, yet they were not completed due to the lack of either computational resources or numerical accuracy.

6.2.1 Exploring the parameter space

All models presented in this thesis are limited to circular, equal-mass binaries. One important reason was because these binaries have the largest angular momentum possible for a given separation (see equation 4.1), thus the interaction with the individual clouds is inefficient with respect to a lower angular momentum system.

Additionally, because of the ubiquity of SMBHs in the nuclei of massive galaxies, an important amount of binaries are expected to be the result of major galaxy mergers with typical mass ratios of $q \gtrsim 1/3$ (Volonteri, Haardt, and Madau, 2003). In this context, near-equal-mass binaries are expected to be common in our Universe.

The case for circularity is much harder. Several theoretical and numerical studies suggest that the eccentricity evolution of a SMBHB is strongly dependent on its environment. When the pairing phase is driven by a self-gravitating nuclear disc, the resulting Keplerian binary has virtually zero eccentricity (Escala et al., 2005; Dotti et al., 2007). However, during the hardening phase, both stellar and gas based shrinking mechanisms have proven to be efficient in increasing the binary orbital eccentricity (e.g. Armitage and Natarajan, 2005; Sesana, Haardt, and Madau, 2008; Cuadra et al., 2009; Sesana, 2010; Sesana, Gualandris, and Dotti, 2011; Amaro-Seoane, Miller, and Freitag, 2009; Amaro-Seoane et al., 2010).

Taking into account the plethora of different binaries expected to form throughout cosmic history, the exploration of the parameter space is crucial to establish a complete spectrum of phenomenologies for sub-parsec SMBHBs evolving within gas-rich and turbulent environments. While it is easier to infer plausible trends of the results with the binary mass ratio, it would be interesting to see how eccentric binaries respond to clouds with different orientations and impact

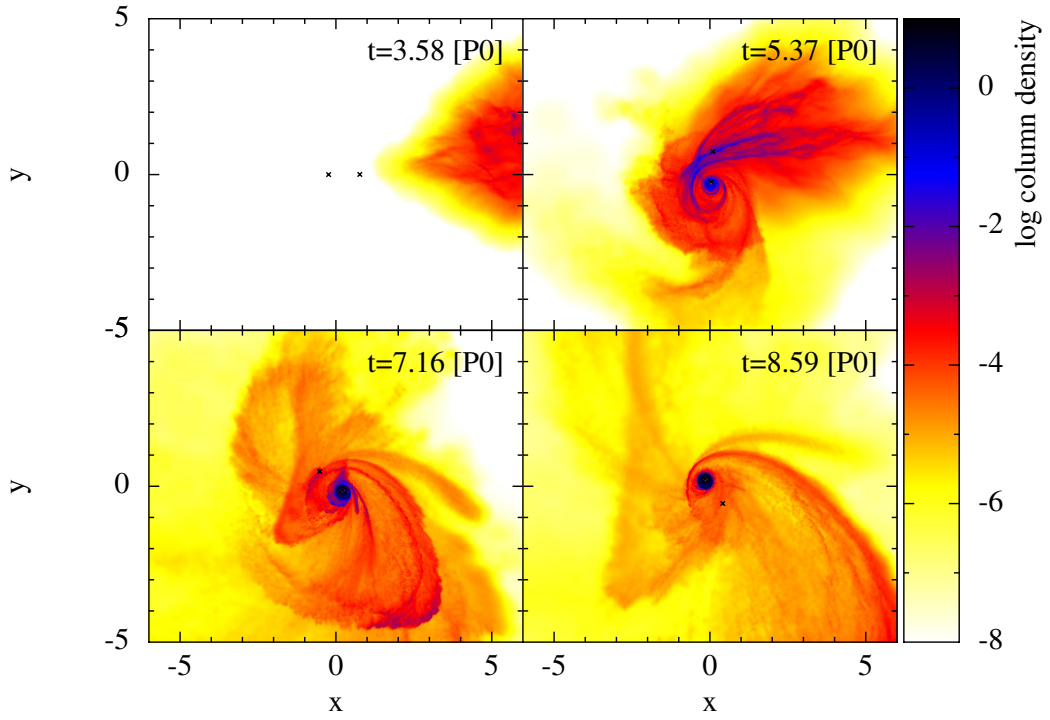

FIGURE 6.1: Density maps of the evolution of an infalling cloud onto a counter-rotating binary. This simulation is similar to the CA0.7 model presented in previous chapters, but using a binary with mass ratio of $q = 1/3$. Both cloud and binary move on the x-y plane, with the latter rotating clockwise.

parameters, especially because eccentricity may play an important role in the final coalescence, as the timescale associated with GW emission is much shorter for very eccentric binaries.

During the course of this research I have performed a modest exploration of the parameter space by modelling some of the same systems displayed in Chapters 3 and 4 with binaries spanning different mass ratios and eccentricities. Fig. 6.1 shows an example of one of these systems, where I simulate an infalling onto a retrograde binary with a mass ratio of $q = 1/3$. The gas has a pericentre distance of $0.35a_0$, which means that the cloud's orbit is equivalent to that of the CA0.7 simulation.

One very interesting result observed from the evolution displayed in figure 6.1 is the formation of a very prominent circumprimary disc. This disc however is exactly counter-rotating with respect to the binary orbit, which can have important implications on its subsequent dynamics and possible observational signatures. Recall that the mini-discs were unresolved during the CA simulations because the gas trapped by the individual SMBHs had little angular momentum.

Despite these enthralling results, the simulations were not exempt from numerical problems. An illustrative example of one of the inconsistencies is the decomposition of the angular momentum into its orbital components, as displayed in Fig. 6.2. The recovered angular momentum is not reproducing the actual evolution measured from the simulation, which basically implies that there is a (numerical) loss of angular momentum markedly affecting the binary orbit and therefore the final result cannot be considered robust. Recall that this was not a problem with the equal-mass models (e.g. figure 4.4).

A smaller binary mass ratio translates into a lower total angular momentum,

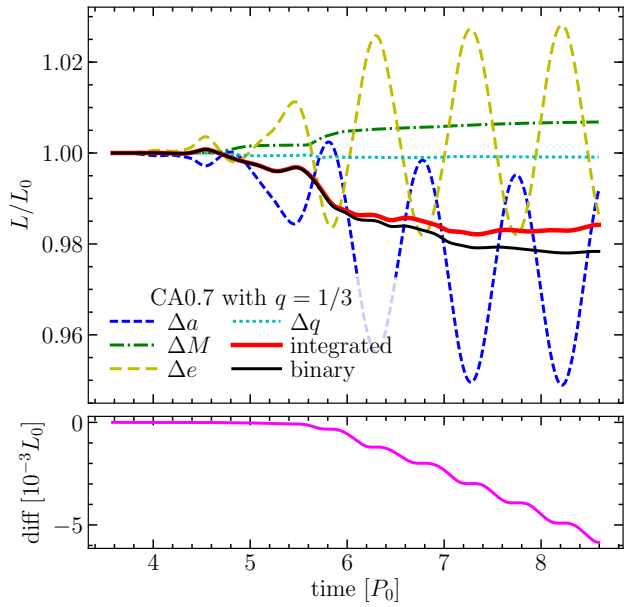

FIGURE 6.2: Decomposition of the binary's angular momentum for the CA0.7 model with $q = 1/3$. This is similar to what I presented in Chapter 4 (eq. 4.2), where the non-solid lines represent the contribution of the individual components (semimajor axis, total mass, eccentricity and mass ratio), the red solid line is the value recovered from the contribution of these components, and the black solid line is the momentum directly measured from the snapshots. The lower panels show the difference between these two last lines.

which means that the exchange with the captured material is much more sensitive to numerical noise. For the particular case shown in figure 6.2, the capture of counter-rotating material by the secondary SMBH now changes noticeably the binary eccentricity. This can be observed in the contribution of this quantity to the angular momentum budget, which was negligible during the equal-mass simulations, and now greatly oscillates. Unfortunately, throughout the simulations exhibited in this thesis, the eccentricity was always the orbital parameter more susceptible to noise.

In consequence, the robust exploration of the parameter space (i.e., q, e or higher cloud's masses) requires considerable computing resources that were not affordable with the standard configuration. Nevertheless, new simulations can be devised in the future using the implementation introduced for the multi-cloud models, where the angular momentum noise produced by the approximation of the gravitational forces was effectively lowered.

6.2.2 Alternative hydrodynamics

Although the SPH method has plenty of features that make it a great tool for modelling the type of systems presented in this thesis, it is not exempt of disadvantages that can affect the accuracy of the results. Most notably, shocks and other kind of discontinuities are not adequately captured by its Hamiltonian formulation. Recently, moving-mesh techniques based on a Voronoi tessellation[1] have been proposed, which offer a quasi-Lagrangian description that inherits some of the advantages of SPH, while retaining the accuracy of an Eulerian mesh-based description. More specifically, Springel (2010a) presents his novel code named AREPO, which solves the Euler equations using the finite-volume approach on an unstructured Voronoi mesh that is generated from set of evolving points. This scheme is Eulerian at heart, but is adjusted to work with particle-based fluid cells. One improvement over SPH is that the errors in the discrete kernel sum are avoided through the use of an explicit second-order accurate spatial reconstruction. The second difference is that the cells are allowed to exchange not only momentum, but also mass and specific entropy, hence naturally resolving mixing that may happen in a multidimensional flow.

In the context of this project, it is possible to test the robustness of some of the results presented by modelling the hydrodynamical evolution of the infalling clouds using AREPO. Particularly, I have simulated an infalling cloud with an initial orbit equivalent to the A0.7 model presented in Chapter 3, i.e aligned with respect to the binary and a pericentre distance of $0.35a_0$. The two black holes are modelled in the same fashion as with GADGET-3, as well as an equivalent barotropic equation of state for the gas thermodynamics. Figure 6.3 displays density maps after the cloud's first passage for two different resolutions.

One of the most recurring results of the SPH-modelled infalling clouds was the formation of (misaligned) mini-discs whenever the gas was somewhat corotating with the binary. For example, all the Aligned models of Chapter 3 displayed very prominent and persistent mini-discs arising from the incoming material. Strikingly, this result is not evident in a similar system modelled with AREPO (see upper panel of Fig. 6.3).

This occurs because SPH has a (numerical) surface tension that keeps these mini-discs stable, even for a low number of particles. In contrast, the absence of this

[1] A Voronoi tessellation is a partitioning of the space into cells based on the distance to a set of generating points. Each cell corresponds to all the points closer to that point than any other.

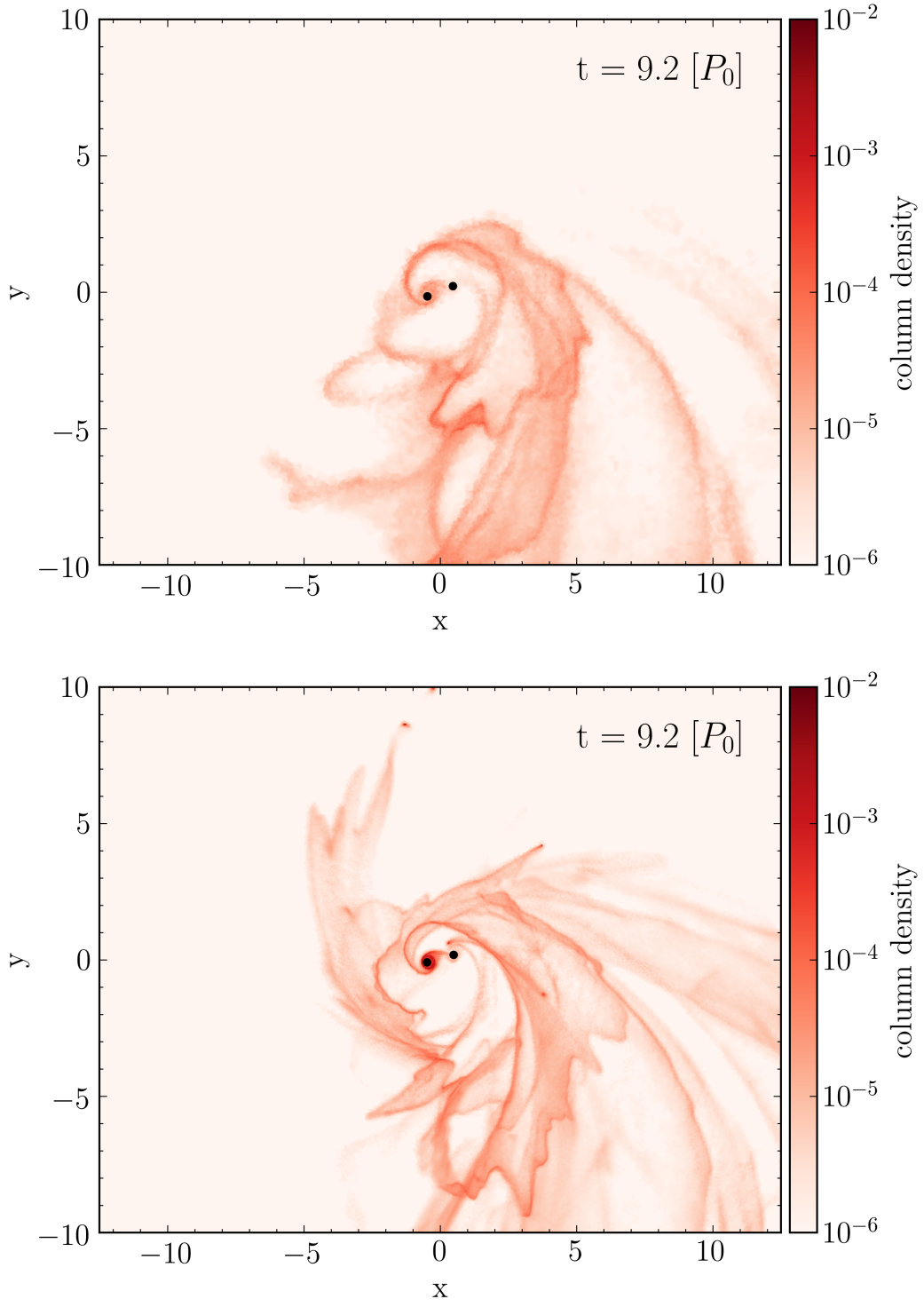

FIGURE 6.3: Density maps of sample simulations using the moving-mesh code AREPO. Both panels show the evolution of an infalling cloud with an orbit similar to the A0.7 model. The upper panel shows a simulation with a mass resolution of 3.8×10^{-8}, while the lower panel has 10 times that resolution.

effect in the moving-mesh causes the resolution to become extremely relevant to observe the formation and evolution of these discs; a certain amount of cells is essential to resolve the gradient between the disc's outer edge and the background grid of gas. When this gradient is not properly resolved the disc inevitably 'dissolves', as the gas is diffused over just a few cells. This fact becomes apparent when increasing the same simulation's mass resolution (lower panel of Fig. 6.3). Note how the gas around the 'left-side' SMBH forms a well-defined, dense mini-disc in the higher resolution simulation, while in the low resolution counter-part the same gas is extremely diffuse. For reference, the mass resolution of the single cloud models of chapters 3 and 4 is $\approx 2.5 \times 10^{-9}$, although the formation of mini-discs was also observed during the multi-cloud simulations with much cruder resolution.

Furthermore, the resolution affects also the morphology of the gas around the binary. Recall, for example, the stream of material observed in the upper left region of the higher resolution model, which is absent in the other case. Consequently, further inspection of the resolution requirements is needed to make a fair comparison with the SPH simulations.

6.2.3 Magnetic fields

Magnetic fields are ubiquitous in our Universe, present on almost all scales, from the intra-cluster medium down to stars and planets. In particular, the formation of relativistic jets by an accreting compact object is one of the fundamental mysteries of modern astrophysics, most prominently because the physics of accretion discs is governed by a combination of different complex processes: gravity, magneto-hydrodynamics, turbulent viscous fluids, and radiation fields, among others. Understanding these processes is particularly relevant for AGNs, since it is expected that jets are the main mechanism of energy injection to the interstellar or the intracluster medium, shaping their host galaxies. It is now commonly accepted that magneto-hydrodynamic (MHD) processes are essential for the launching, acceleration and collimation of the outflows and jets from accretion discs (Blandford and Payne, 1982; Pudritz and Norman, 1983; Ferreira, 1997; Pudritz et al., 2007; Hawley et al., 2015)

As discussed in Chapter 3 in the context of the mini-disc dynamics, the precession and wobbling of accretion discs could cause moving jets, provided that their dynamics are actually linked. This possibility was recently studied by Sheikhnezami and Fendt (2015), where they numerically model the formation and launching of jets from a circumprimary accretion disc that is perturbed by the presence of a secondary body. Their simulations show strong indication of a jet precession caused by the wobbling of the jet launching disc, although their models require a longer time integration to establish whether this was a long-term behaviour or just a transient effect of the disc's misalignment.

With the goal of investigating the effect of magnetic fields on these type of systems, I studied the evolution of a sub-parsec circumbinary disc using the magneto-hydrodynamics (MHD) implementation presented by Stasyszyn and Elstner (2015) in GADGET-3. Because this new implementation was first tested in the context of galactic simulations, it is important to test its applicability to the type of systems presented in this thesis.

It is straightforward to realise that an impacting cloud onto a binary is a very extreme system, with abrupt changes in velocity, density, temperature, to name a few. For that reason I chose a well-studied system with a much 'smoother' evolution;

I simulate the same system described in Cuadra et al. (2009) which consists of a SMBHB with an initial mass ratio of $q = 1/3$ and a circular orbit, embedded in a disc with 20% its mass. The initial conditions are set such that the gas is located from $r_{\rm in} = 2a_0$ to $r_{\rm out} = 5a_0$, where a_0 is the binary's initial semimajor axis. However, it is important to avoid spurious growth of the magnetic field due to violent initial evolution of the disc, therefore I use as initial condition a system that is already in a quasi-steady equilibrium. I start with a binary-disc setup that has already been evolved for 500 dynamical times ($250/\pi$ orbits) without any magnetic field. The vector potential is initialised as

$$\mathbf{A} = \frac{B_0}{2\pi\sqrt{\pi}}\left[(\cos kz + \cos 2ky)\hat{\imath} + (\cos kx + \cos 2kz)\hat{\jmath} + (\cos ky + \cos 2kx)\hat{k}\right], \quad (6.1)$$

where $B_0 = 10^{-6}$ G, $k = 2\pi/\lambda$ and $\lambda = 1$. This magnetic field has initially no preferential direction and its low value implies that it is dynamically negligible.

A crucial factor determining the evolution of magnetic fields is turbulence in the gaseous flow. Analogous to viscosity, the transport of the magnetic field lines is done through turbulence, which is not necessarily a quantity resolved in all areas of the simulation. Therefore, it is necessary to implement a sub-grid model for the magnetic diffusivity η. I simulated the evolution of the magnetic field using the following models:

1. "Ideal MHD":
$$\eta(\mathbf{x}) = 10^{-5} \quad (\approx 6\,\mathrm{pc\,km\,s^{-1}}). \quad (6.2)$$
This model represents the full turbulent case. It does not capture the real properties of the disc, because of the unresolved turbulence in the denser regions of the simulation. However, it will be valid in the rest of the domain. Note that this value is small, but not zero, because a small diffusivity is needed to avoid numerical problems (too steep gradients). In practice, this model implies the strongest magnetic field inside the cavity because the magnetic field generated through stretching and twisting of the magnetic lines close to the SMBHs is not transported efficiently outside this region.

2. "High diffusion":
$$\eta(\mathbf{x}) = 10^{-3} \quad (\approx 600\,\mathrm{pc\,km\,s^{-1}}). \quad (6.3)$$
This model is the complete opposite to the Ideal case, because it considers that turbulence is not resolved in any region of the simulation, hence there is a high and constant diffusivity in all the domain. Because this high diffusion transports a lot of magnetic field outside the cavity, this model has the smallest values of magnetic field strength inside this region.

3. "Turbulent disc and ideal corona":
$$\eta(\mathbf{x}) = \xi(\rho)\alpha\frac{c_s^2}{\Omega_K}, \quad (6.4)$$
where α is a free parameter chosen to be 0.1,
$$\xi(\rho) = \begin{cases} 0 & \text{for } \rho \leq 0.25\rho_{\rm d} \\ \dfrac{4}{3}\left(\dfrac{\rho}{\rho_{\rm d}} - 0.25\right) & \text{for } 0.25\rho_{\rm d} < \rho < \rho_{\rm d}\,, \\ 1 & \text{for } \rho \geq \rho_{\rm d} \end{cases} \quad (6.5)$$

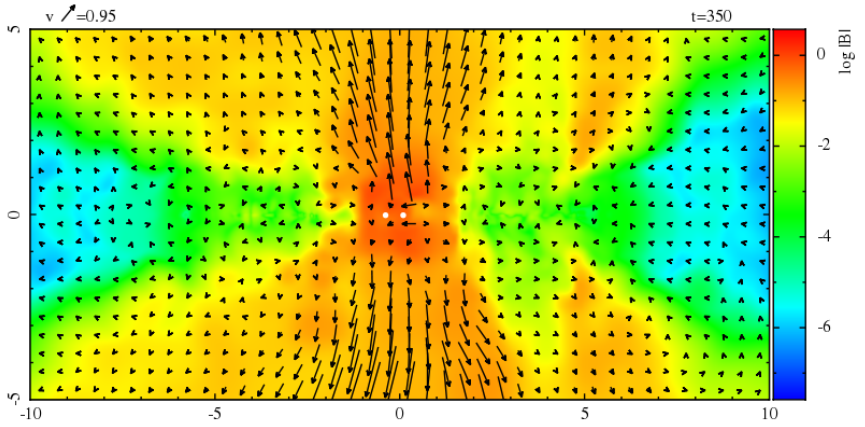

FIGURE 6.4: Edge-on view of the circumbinary disc with a magnetic field strength map. The arrows represent the velocity of the gas particles. The position of the two SMBHs is indicated by the white solid circles. Here it is possible to visualise the presence of clear outflows coming from the material close to the binary, driven by the increase of the magnetic field inside the cavity.

and $\rho_{\rm d}$ is a threshold density that captures the transition between the disc and the surrounding corona. I have chosen $\rho_{\rm d} = 10^{-4}$ (code units) based on the values observed in the gas initial conditions. This diffusivity model is based in the study of Dyda et al. (2013). It transitions between high diffusion where the turbulence is not resolved to no diffusion where the density is low enough that the flow is naturally turbulent. This model probably captures the real properties of the different regions in the simulation, and for that it is the most physical of the three. In practice, this implementation exhibits intermediate values of the magnetic field strength with respect the other two diffusivities.

One of the most compelling results with these simulations was the formation of outflows coming from the inner disc's cavity. These outflows emerged independent of the magnetic diffusivity used. Thanks to the versatility of SPH codes and their applicability to dynamic studies, this is the first time that it has been possible to study the magnetic field growth inside the cavity and the associated formation of outflows, which could have strong implications in the evolution and observability of SMBHBs. Figure 6.4 shows an example of the final state of one of these simulations. The edge-on view of the disc demonstrates very clearly that the increase of magnetic field strength inside the disc's cavity produces a bipolar outflow with typical speeds of roughly the binary's circular velocity.

To further study the impact of these outflows on the binary evolution, the left panel of Figure 6.5 displays the mass accretion as a function of time. It is noticeable how the accretion decreases with respect to a non-magnetised system, being more suppressed with the stronger magnetic fields. This could imply two things: (i) the magnetic field is providing an additional source of pressure in the cavity's wall, thus preventing some of the material to infall onto the SMBHs, and/or (ii) the outflows are expelling a considerable amount of material. To disentangle between these two options I computed the inflow of material through the cavity walls (Fig. 6.5, right top panel), as well as the expelled gas in the form of outflows (Fig. 6.5, right bottom panel). From Fig 6.5, it is evident that the material enters the cavity almost unaffected by the magnetic field because the inflowing gas does not change significantly from the control run. However, once the material has entered

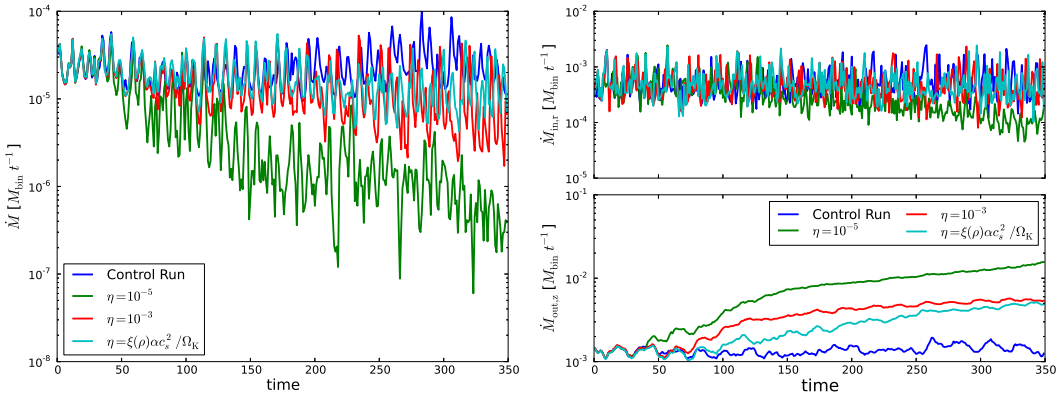

FIGURE 6.5: *Left:* Time evolution of the mass accretion onto the binary for the different models of magnetic diffusivity. This plot clearly shows that the presence of the magnetic field suppresses some of the accretion with respect to the non-magnetic control run (blue solid line). *Right:* the two panels show the inflowing (top) and outflowing (bottom) material onto the cavity. This plot demonstrates that the material enters the cavity roughly unaffected by the magnetic field, but the outflows are responsible for suppressing the accretion by expelling gas from this region.

the cavity a fraction is ejected with the outflows, thus suppressing some of the accretion onto the binary. The effect becomes stronger with higher values of the magnetic field.

The action of these outflows could have important implications. For instance, as explained before, the details of the gas dynamics inside the cavity have a major impact on the binary orbital evolution. Consequently, these results suggest that the presence of magnetic fields can completely change the standard picture drawn from previous models because the outflowing material is changing significantly the amount of gas available to torque the SMBHs.

Unfortunately, even if these results are very interesting, more investigation is required to establish whether the measured magnetic field growth is physical or numerically driven. The steep gradients produced by the abrupt changes in density inside the disc's cavity can generate spurious buildup, mimicking the presence of a dynamo. Once these models are on a firm ground, the MHD implementation can be applied to more 'extreme' systems, such as an infalling cloud or individual mini-discs being perturbed by a secondary body.

6.3 Final remarks

In this thesis I have presented a series of numerical models of gaseous clouds interacting with sub-parsec supermassive black hole binaries. This research represents the first extensive study of the impact of different configurations on the binary's orbital response, as well as on the formation of gaseous structures, for a system embedded in a turbulent environment where discrete accretion events in the form of cold molecular clouds are expected to take place. This corresponds to a new mechanism for the evolution of sub-parsec binaries that has not been considered before in the literature. I would like to leave the reader with the thought

that this type of accretion, probably ubiquitous in some galactic nuclei, has important implications in both the observability and evolution of these binaries.

Appendix A

Convergence tests with accretion radius

As discussed in Section 4.3, the transient evolution of the binary orbital elements is dominated by the exchange of angular momentum with the accreted material. Hence, resolving the accretion process properly is a key aspect of this study. Due to numerical considerations explained in Chapter 2, I model each SMBH with a very large sink radius compared to the Schwarzschild radius, producing unrealistically large accretion rates.

In order to establish the role of the chosen sink radius, I rerun some of the single cloud models changing only this parameter. I test two smaller values of the sink radius (0.05 and 0.025) and a larger one (0.2) to study the convergence of the binary orbital evolution. I choose the A0.7 and CA0.7 models because they represent two extremes in regards to accretion: in the first case there is the formation of very prominent mini-discs around each SMBH, while in the latter the material plunges almost directly due to cancelation of angular momentum in the gas. Additionally, I have chosen the smallest pericentre distance since the accretion is larger and thus any difference could be enhanced.

The binary evolution during the first orbits is shown in Fig. A.1. Since the simulations with smaller accretion radius are more computationally expensive, I run these models only until the prompt accretion stops. Nevertheless, this is the point where the transient binary evolution also stops, as showed in Section 4.2.1.

For the A0.7 models the semimajor axis evolution is roughly equal for radii smaller than 0.2, even though the accreted mass changes with each value of $r_{\rm p}$, as expected. This is because the bulk of angular momentum exchange occurs when the material is 'captured' by the SMBHs, rather than the accretion itself. For this system orientation, decreasing the accretion radius translates the inner edge of the mini-discs being closer to the MBHs, delaying the accretion somewhat, but not changing the dynamics any further.

For the CA0.7 models, the difference in Δa between the 0.2 and 0.025 simulations is $\sim 4 \times 10^{-3}$, which is $\sim 6\%$ of the total change. Interestingly, the accretion seems to converge at the end, but for the smaller $r_{\rm sink}$ there is a 'transient suppression' around $t = 6P_0$, which makes the semi-major axis decrease even more with respect to the other cases. This is because some of the gas is allowed to wander around the binary a while longer before being captured, interacting gravitationally with the SMBHs.

In conclusion, the semimajor axis evolution of the binary its only mildly dependent on the choice of sink radius. This indicates that the exchange of angular momentum between the gas and the SMBHs occurs through the *captured* material rather than the *accreted* material, since the gas that crosses the sink radius has already lost most of its initial angular momentum during the interaction with the binary.

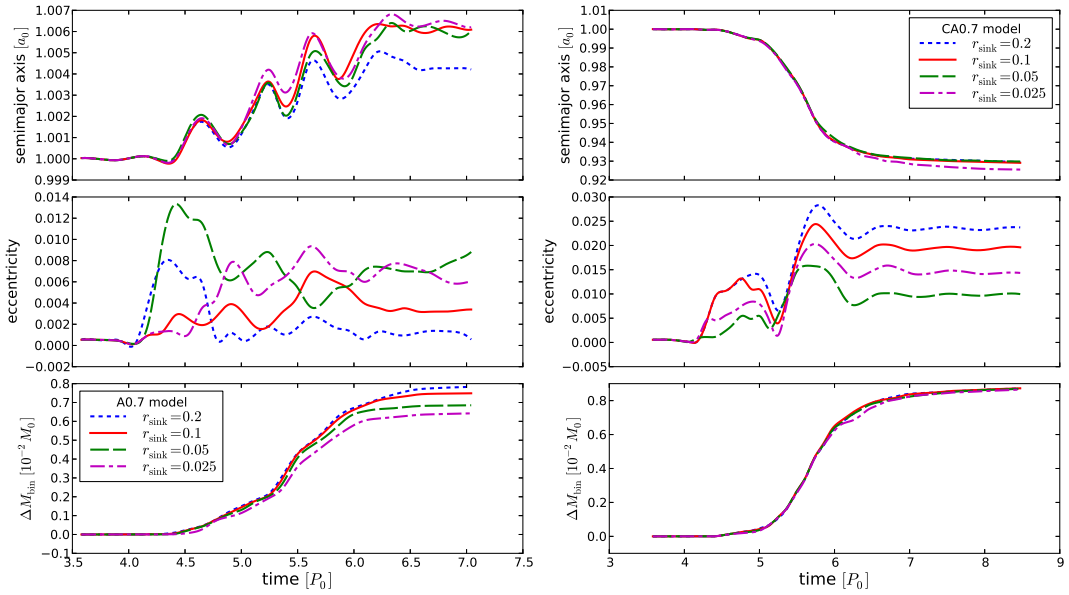

FIGURE A.1: Evolution of the binary semimajor axis (upper panel), eccentricity (middle panel) and accreted mass (lower panels) for the A0.7 and CA0.7 models with different sink radii, as indicated in the legend. Recall that the solid red line represents the 'original' system.

On the other hand, the eccentricity does not appear to converge in any of the models. This is consistent with it having always very small values, which are dominated by numerical noise instead of physical processes. Since I am not really considering the eccentricity evolution in this work, this does not affect the conclusions of my study.

Publications

The content presented in this thesis has been largely based on the following published, or accepted for publication, research papers:

Chapter 3:

Goicovic, F. G., Cuadra, J., Sesana, A., Stasyszyn, F., Amaro-Seoane, P. & Tanaka, T. L. 2016, *"Infalling clouds on to supermassive black hole binaries – I. Formation of discs, accretion and gas dynamics"*, MNRAS, 455, 1989

Chapter 4:

Goicovic, F. G., Sesana, A., Cuadra, J. & Stasyszyn, F. 2017, *"Infalling clouds on to supermassive black hole binaries – II. Binary evolution and the final parsec problem"* MNRAS. *arXiv:1602.01966*

Bibliography

Aarseth, S. J. 2003, *Ap&SS* **285**, 367–372.

Abbott, B. P. et al. 2016, *Phys. Rev. Lett.* **116** (6), 061102.

Abramowicz, M. A. et al. 1988, *ApJ* **332**, 646–658.

Alig, C. et al. 2011, *MNRAS* **412**, 469–486.

Aly, H. et al. 2015, *MNRAS* **449**, 65–76.

Amaro-Seoane, P., Brem, P., and Cuadra, J. 2013, *ApJ* **764**, 14, 14.

Amaro-Seoane, P., Miller, M. C., and Freitag, M. 2009, *ApJ* **692**, L50–L53.

Amaro-Seoane, P. et al. 2010, *MNRAS* **401**, 2268–2284.

Amaro-Seoane, P. et al. 2013, *GW Notes, Vol. 6, p. 4-110* **6**, 4–110.

Armitage, P. J. and Natarajan, P. 2005, *ApJ* **634**, 921–927.

Artymowicz, P. and Lubow, S. H. 1994, *ApJ* **421**, 651–667.

Artymowicz, P. and Lubow, S. H. 1996, *ApJ* **467**, L77.

Babak, S. et al. 2016, *MNRAS* **455**, 1665–1679.

Backer, D. C., Jaffe, A. H., and Lommen, A. N. 2004, *Coevolution of Black Holes and Galaxies*, 438.

Balsara, D. S. 1995, *Journal of Computational Physics* **121**, 357–372.

Barnes, J. and Hut, P. 1986, *Nature* **324**, 446–449.

Barnes, J. E. and Hernquist, L. E. 1991, *ApJ* **370**, L65–L68.

Barnes, J. E. and Hernquist, L. E. 1996, *ApJ* **471**, 115.

Barth, A. J. et al. 2008, *ApJ* **683**, L119, L119.

Bate, M. R., Bonnell, I. A., and Price, N. M. 1995, *MNRAS* **277**, 362–376.

Bate, M. R. et al. 2000, *MNRAS* **317**, 773–781.

Begelman, M. C., Blandford, R. D., and Rees, M. J. 1980, *Nature* **287**, 307–309.

Bellovary, J. et al. 2013, *ApJ* **779**, 136, 136.

Berczik, P. et al. 2006, *ApJ* **642**, L21–L24.

Bianchi, S. et al. 2008, *MNRAS* **386**, 105–110.

Blandford, R. D. and Payne, D. G. 1982, *MNRAS* **199**, 883–903.

Bogdanović, T. 2015, *Astrophysics and Space Science Proceedings* **40**, 103.

Bolton, C. T. 1972, *Nature* **235**, 271–273.

Bondi, H. 1952, *MNRAS* **112**, 195.

Bonnell, I. A. 1994, *MNRAS* **269**.

Bonnell, I. A. and Rice, W. K. M. 2008, *Science* **321**, 1060–.

Bouvier, J. et al. 2013, *A&A* **557**, A77, A77.

Brem, P. et al. 2014, *ApJ* **792**, 100, 100.

Callegari, S. et al. 2009, *ApJ* **696**, L89–L92.

Casassus, S. et al. 2015, *ApJ* **811**, 92, 92.

Chandrasekhar, S. 1943, *ApJ* **97**, 255.

Charisi, M. et al. 2016, *MNRAS* **463**, 2145–2171.

Cheng, Y. et al. 2016, *Classical and Quantum Gravity* **33**.12, 125015, 125015.

Colpi, M. 2014, *Space Sci. Rev.* **183**, 189–221.

Colpi, M. and Dotti, M. 2011, *Advanced Science Letters* **4**, 181–203.

Combes, F., Young, L. M., and Bureau, M. 2007, *MNRAS* **377**, 1795–1807.

Comerford, J. M. et al. 2009, *ApJ* **702**, L82–L86.

Consortium, T. e. et al. 2013, *arXiv:1305.5720*.

Coughlin, E. R. and Armitage, P. J. 2017, *arXiv:1705.04689*.

Cuadra, J. et al. 2006, *MNRAS* **366**, 358–372.

Cuadra, J. et al. 2009, *MNRAS* **393**, 1423–1432.

Curtis, M. and Sijacki, D. 2016, *MNRAS* **463**, 63–77.

Dabringhausen, J., Hilker, M., and Kroupa, P. 2008, *MNRAS* **386**, 864–886.

Dasyra, K. M. et al. 2006a, *ApJ* **638**, 745–758.

Dasyra, K. M. et al. 2006b, *ApJ* **651**, 835–852.

David, L. P. et al. 2014, *ApJ* **792**, 94, 94.

Decarli, R. et al. 2013, *MNRAS* **433**, 1492–1504.

del Valle, L. and Escala, A. 2012, *ApJ* **761**, 31, 31.

del Valle, L. and Escala, A. 2014, *ApJ* **780**, 84, 84.

del Valle, L. et al. 2015, *ApJ* **811**, 59, 59.

D'Orazio, D. J., Haiman, Z., and MacFadyen, A. 2013, *MNRAS* **436**, 2997–3020.

D'Orazio, D. J., Haiman, Z., and Schiminovich, D. 2015, *Nature* **525**, 351–353.

D'Orazio, D. J. et al. 2015, *MNRAS* **452**, 2540–2545.

Dotti, M., Sesana, A., and Decarli, R. 2012, *Advances in Astronomy* **2012**, 940568, 3.

Dotti, M. et al. 2007, *MNRAS* **379**, 956–962.

Dotti, M. et al. 2009, *MNRAS* **396**, 1640–1646.

Dotti, M. et al. 2010, *MNRAS* **402**, 682–690.

Dotti, M. et al. 2013, *ApJ* **762**, 68, 68.

Doğan, S. et al. 2015, *MNRAS* **449**, 1251–1258.

Dubois, Y. et al. 2012, *MNRAS* **423**, 3616–3630.

Dunhill, A. C., Cuadra, J., and Dougados, C. 2015, *MNRAS* **448**, 3545–3554.

Dunhill, A. C. et al. 2014, *MNRAS* **445**, 2285–2296.

Dyda, S. et al. 2013, *MNRAS* **432**, 127–137.

Eddington, A. S. 1924, *Nature* **113**, 192.

Einstein, A. 1915, *Sitzungsberichte der Königlich Preußischen Akademie der Wissenschaften (Berlin), Seite 831-839.*

Einstein, A. 1916, *Sitzungsberichte der Königlich Preußischen Akademie der Wissenschaften (Berlin), Seite 688-696.*

Eracleous, M. et al. 2012, *ApJS* **201**, 23, 23.

Escala, A. et al. 2004, *ApJ* **607**, 765–777.

Escala, A. et al. 2005, *ApJ* **630**, 152–166.

Farris, B. D. et al. 2015a, *MNRAS* **447**, L80–L84.

Farris, B. D. et al. 2015b, *MNRAS* **446**, L36–L40.

Ferrarese, L. and Merritt, D. 2000, *ApJ* **539**, L9–L12.

Ferreira, J. 1997, *A&A* **319**, 340–359.

Fiacconi, D. et al. 2013, *ApJ* **777**, L14, L14.

Finkelstein, David. 1958, *Phys. Rev.* **110** (4), 965–967.

Fragner, M. M. and Nelson, R. P. 2010, *A&A* **511**, A77, A77.

Gaspari, M., Brighenti, F., and Temi, P. 2015, *A&A* **579**, A62, A62.

Gaspari, M., Ruszkowski, M., and Oh, S. P. 2013, *MNRAS* **432**, 3401–3422.

Gaspari, M., Ruszkowski, M., and Sharma, P. 2012, *ApJ* **746**, 94, 94.

Gaspari, M. and Sądowski, A. 2017, *ApJ* **837**, 149, 149.

Gaspari, M., Temi, P., and Brighenti, F. 2017, *MNRAS* **466**, 677–704.

Gebhardt, K. et al. 2000, *ApJ* **539**, L13–L16.

Ghez, A. M. et al. 2008, *ApJ* **689**, 1044-1062, 1044–1062.

Giacconi, R. et al. 1962, *Physical Review Letters* **9**, 439–443.

Gillessen, S. et al. 2009, *ApJ* **707**, L114–L117.

Gingold, R. A. and Monaghan, J. J. 1977, *MNRAS* **181**, 375–389.

Goodman, J. 2003, *MNRAS* **339**, 937–948.

Gould, A. and Rix, H.-W. 2000, *ApJ* **532**, L29–L32.

Graham, M. J. et al. 2015a, *Nature* **518**, 74–76.

Graham, M. J. et al. 2015b, *MNRAS* **453**, 1562–1576.

Green, P. J. et al. 2010, *ApJ* **710**, 1578–1588.

Gualandris, A. et al. 2017, *MNRAS* **464**, 2301–2310.

Haiman, Z., Kocsis, B., and Menou, K. 2009, *ApJ* **700**, 1952–1969.

Hamer, S. L. et al. 2016, *MNRAS* **460**, 1758–1789.

Hartmann, L. et al. 1998, *ApJ* **495**, 385–400.

Hawking, S. W. 1974, *Nature* **248**, 30–31.

Hawley, J. F. et al. 2015, *Space Sci. Rev.* **191**, 441–469.

Hemsendorf, M., Sigurdsson, S., and Spurzem, R. 2002, *ApJ* **581**, 1256–1270.

Hernquist, L. 1989, *Nature* **340**, 687–691.

Hernquist, L. 1990, *ApJ* **356**, 359–364.

Hernquist, L. and Barnes, J. E. 1991, *Nature* **354**, 210–212.

Herrnstein, J. R. et al. 2005, *ApJ* **629**, 719–738.

Hewish, A. et al. 1968, *Nature* **217**, 709–713.

Hobbs, A. and Nayakshin, S. 2009, *MNRAS* **394**, 191–206.

Hobbs, A. et al. 2011, *MNRAS* **413**, 2633–2650.

Hobbs, G. et al. 2010, *Classical and Quantum Gravity* **27**.8, 084013, 084013.

Holley-Bockelmann, K. and Khan, F. M. 2015, *ApJ* **810**, 139, 139.

Hopkins, P. F. and Quataert, E. 2010, *MNRAS* **407**, 1529–1564.

Hopkins, P. F. and Quataert, E. 2011, *MNRAS* **415**, 1027–1050.

Hudson, D. S. et al. 2006, *A&A* **453**, 433–446.

Ivanov, P. B., Papaloizou, J. C. B., and Polnarev, A. G. 1999, *MNRAS* **307**, 79–90.

Ivezic, Z. et al. 2008, *arXiv:0805.2366*.

Ju, W. et al. 2013, *ApJ* **777**, 44, 44.

Kelly, B. C. and Shen, Y. 2013, *ApJ* **764**, 45, 45.

Kerr, Roy P. 1963, *Phys. Rev. Lett.* **11** (5), 237–238.

Khan, F. M., Just, A., and Merritt, D. 2011, *ApJ* **732**, 89, 89.

Khan, F. M. et al. 2013, *ApJ* **773**, 100, 100.

King, A. R. and Pounds, K. A. 2003, *MNRAS* **345**, 657–659.

King, A. R. and Pringle, J. E. 2006, *MNRAS* **373**, L90–L92.

King, A. R. and Pringle, J. E. 2007, *MNRAS* **377**, L25–L28.

Kocsis, B., Haiman, Z., and Loeb, A. 2012, *MNRAS* **427**, 2680–2700.

Komossa, S. et al. 2003, *ApJ* **582**, L15–L19.

Kormendy, J. and Ho, L. C. 2013, *ARA&A* **51**, 511–653.

Kormendy, J. and Richstone, D. 1995, *ARA&A* **33**, 581.

Kozai, Y. 1962, *AJ* **67**, 579.

Laplace, P. S. 1799, *Allgemeine Geographische Ephemeriden, Vol. 4, Issue 1, p. 1-6* **4**, 1–6.

Larson, R. B. 1981, *MNRAS* **194**, 809–826.

Larwood, J. D. et al. 1996, *MNRAS* **282**, 597–613.

Lemaître, G. 1933, *Annales de la Société Scientifique de Bruxelles* **53**.

Levine, R., Gnedin, N. Y., and Hamilton, A. J. S. 2010, *ApJ* **716**, 1386–1396.

Li, Y.-R. et al. 2016, *ApJ* **822**, 4, 4.

Lidov, M. L. 1962, *Planet. Space Sci.* **9**, 719–759.

Lira, P. et al. 2011, *MNRAS* **415**, 1290–1303.

Liu, F. K., Li, S., and Chen, X. 2009, *ApJ* **706**, L133–L137.

Liu, F. K., Li, S., and Komossa, S. 2014, *ApJ* **786**, 103, 103.

Liu, T. et al. 2015, *ApJ* **803**, L16, L16.

Lodato, G. et al. 2009, *MNRAS* **398**, 1392–1402.

Looper, D. L. et al. 2010, *ApJ* **714**, 45–67.

Lu, J. R. et al. 2009, *ApJ* **690**, 1463–1487.

Lu, K.-X. et al. 2016, *MNRAS* **459**, L124–L128.

Lubow, S. H. and Ogilvie, G. I. 2000, *ApJ* **538**, 326–340.

Lucas, W. E. et al. 2013, *MNRAS* **433**, 353–365.

Lucy, L. B. 1977, *AJ* **82**, 1013–1024.

Lupi, A. et al. 2015, *MNRAS* **453**, 3437–3446.

Lynden-Bell, D. 1969, *Nature* **223**, 690–694.

MacFadyen, A. I. and Milosavljević, M. 2008, *ApJ* **672**, 83-93, 83–93.

Madigan, A.-M., Levin, Y., and Hopman, C. 2009, *ApJ* **697**, L44–L48.

Magorrian, J. et al. 1998, *AJ* **115**, 2285–2305.

Manset, N. et al. 2009, *A&A* **499**, 137–148.

Mapelli, M. et al. 2012, *ApJ* **749**, 168, 168.

Martin, R. G. et al. 2014, *ApJ* **792**, L33, L33.

Masunaga, H. and Inutsuka, S.-i. 2000, *ApJ* **531**, 350–365.

Masunaga, H., Miyama, S. M., and Inutsuka, S.-i. 1998, *ApJ* **495**, 346–369.

Mayer, L. et al. 2007, *Science* **316**, 1874–.

McConnell, N. J. and Ma, C.-P. 2013, *ApJ* **764**, 184, 184.

McNamara, B. R. et al. 2014, *ApJ* **785**, 44, 44.

Meijerink, R., Spaans, M., and Israel, F. P. 2007, *A&A* **461**, 793–811.

Merloni, A. and Heinz, S. 2013, in: *Planets, Stars and Stellar Systems. Volume 6: Extragalactic Astronomy and Cosmology*. Ed. by T. D. Oswalt and W. C. Keel, 503.

Merritt, D., Mikkola, S., and Szell, A. 2007, *ApJ* **671**, 53–72.

Merritt, D. and Milosavljević, M. 2005, *Living Reviews in Relativity* **8**.

Merritt, D. and Vasiliev, E. 2011, *ApJ* **726**, 61, 61.

Michell, J. 1784, *Philosophical Transactions of the Royal Society of London Series I* **74**, 35–57.

Mikkola, S. and Valtonen, M. J. 1992, *MNRAS* **259**, 115–120.

Milosavljević, M. and Merritt, D. 2001, *ApJ* **563**, 34–62.

Milosavljević, M. and Merritt, D. 2003, *ApJ* **596**, 860–878.

Moeckel, N. and Bally, J. 2006, *ApJ* **653**, 437–446.

Morris, J.P. and Monaghan, J.J. 1997, *Journal of Computational Physics* **136**.1, 41 –50.

Nayakshin, S. and King, A. 2007, *arXiv:0705.1686*.

Nayakshin, S., Power, C., and King, A. R. 2012, *ApJ* **753**, 15, 15.

Newman, E. T. et al. 1965, *Journal of Mathematical Physics* **6**, 918–919.

Nixon, C., King, A., and Price, D. 2013, *MNRAS* **434**, 1946–1954.

Nixon, C. and Lubow, S. H. 2015, *MNRAS* **448**, 3472–3483.

Nixon, C. J. 2012, *MNRAS* **423**, 2597–2600.

Nixon, C. J., King, A. R., and Pringle, J. E. 2011, *MNRAS* **417**, L66–L69.

Nixon, C. J. et al. 2011, *MNRAS* **412**, 1591–1598.

Özel, F. et al. 2010, *ApJ* **725**, 1918–1927.

Papaloizou, J. C. B. and Terquem, C. 1995, *MNRAS* **274**, 987–1001.

Paumard, T. et al. 2006, *ApJ* **643**, 1011–1035.

Peters, P. C. and Mathews, J. 1963, *Physical Review* **131**, 435–440.

Planelles, S. et al. 2014, *MNRAS* **438**, 195–216.

Poon, M. Y. and Merritt, D. 2004, *ApJ* **606**, 774–787.

Preto, M. et al. 2011, *ApJ* **732**, L26, L26.

Price, D. J. 2012, *Journal of Computational Physics* **231**, 759–794.

Prieto, J. et al. 2017, *ApJ* **836**, 216, 216.

Pudritz, R. E. and Norman, C. A. 1983, *ApJ* **274**, 677–697.

Pudritz, R. E. et al. 2007, *Protostars and Planets V*, 277–294.

Quinlan, G. D. 1996, *New Astron.* **1**, 35–56.

Reynolds, C. S. et al. 2009, *ApJ* **691**, 1159–1167.

Rodriguez, C. et al. 2006, *ApJ* **646**, 49–60.

Roedig, C. and Sesana, A. 2014, *MNRAS* **439**, 3476–3489.

Roedig, C. et al. 2011, *MNRAS* **415**, 3033–3041.

Roedig, C. et al. 2012, *A&A* **545**, A127, A127.

Roland, J. et al. 2009, *A&A* **496**, 645–651.

Roškar, R. et al. 2015, *MNRAS* **449**, 494–505.

Runnoe, J. C. et al. 2017, *MNRAS* **468**, 1683–1702.

Russell, H. R. et al. 2014, *ApJ* **784**, 78, 78.

Sanders, D. B. and Mirabel, I. F. 1996, *ARA&A* **34**, 749.

Sanders, D. B. et al. 1988, *ApJ* **325**, 74–91.

Sandrinelli, A. et al. 2016, *AJ* **151**, 54, 54.

Schmidt, M. 1963, *Nature* **197**, 1040.

Schwarzschild, K. 1916, *Abh. Konigl. Preuss. Akad. Wissenschaften Jahre 1906,92, Berlin,1907* **1916**.

Sesana, A. 2010, *ApJ* **719**, 851–864.

Sesana, A. 2013, *MNRAS* **433**, L1–L5.

Sesana, A., Gualandris, A., and Dotti, M. 2011, *MNRAS* **415**, L35–L39.

Sesana, A., Haardt, F., and Madau, P. 2006, *ApJ* **651**, 392–400.

Sesana, A., Haardt, F., and Madau, P. 2008, *ApJ* **686**, 432-447, 432–447.

Sesana, A. and Khan, F. M. 2015, *MNRAS* **454**, L66–L70.

Sesana, A. and Vecchio, A. 2010, *Phys. Rev. D* **81**.10, 104008, 104008.

Sesana, A. et al. 2011, *Phys. Rev. D* **83**.4, 044036, 044036.

Sesana, A. et al. 2012, *MNRAS* **420**, 860–877.

Sesana, A. et al. 2014, *ApJ* **794**, 104, 104.

Shakura, N. I. and Sunyaev, R. A. 1973, *A&A* **24**, 337–355.

Sheikhnezami, S. and Fendt, C. 2015, *ApJ* **814**, 113, 113.

Sillanpaa, A. et al. 1988, *ApJ* **325**, 628–634.

Smith, R. M. et al. 2014, in: *Ground-based and Airborne Instrumentation for Astronomy V*. **9147**. Proc. SPIE, 914779.

Springel, V. 2005, *MNRAS* **364**, 1105–1134.

Springel, V. 2010a, *MNRAS* **401**, 791–851.

Springel, V. 2010b, *ARA&A* **48**, 391–430.

Springel, V., Di Matteo, T., and Hernquist, L. 2005, *MNRAS* **361**, 776–794.

Springel, V. and Hernquist, L. 2002, *MNRAS* **333**, 649–664.

Stasyszyn, F. A. and Elstner, D. 2015, *Journal of Computational Physics* **282**, 148–156.

Steinmetz, M. 1996, *MNRAS* **278**, 1005–1017.

Syer, D. and Clarke, C. J. 1995, *MNRAS* **277**, 758–766.

Tang, Y., MacFadyen, A., and Haiman, Z. 2017, *arXiv:1703.03913*.

Tremblay, G. R. et al. 2015, *MNRAS* **451**, 3768–3800.

Tremblay, G. R. et al. 2016, *Nature* **534**, 218–221.

Tsalmantza, P. et al. 2011, *ApJ* **738**, 20, 20.

Valtonen, M. J. et al. 2011, *ApJ* **729**, 33, 33.

Vasiliev, E., Antonini, F., and Merritt, D. 2015, *ApJ* **810**, 49, 49.

Veilleux, S. et al. 2009, *ApJ* **701**, 587–606.

Villforth, C. et al. 2010, *MNRAS* **402**, 2087–2111.

Volonteri, M., Haardt, F., and Madau, P. 2003, *ApJ* **582**, 559–573.

Webster, B. L. and Murdin, P. 1972, *Nature* **235**, 37–38.

White, S. D. M. and Rees, M. J. 1978, *MNRAS* **183**, 341–358.

Woods, D. F., Geller, M. J., and Barton, E. J. 2006, *AJ* **132**, 197–209.

Yu, Q. 2002, *MNRAS* **331**, 935–958.

Zheng, Z.-Y. et al. 2016, *ApJ* **827**, 56, 56.